**Universitat Jaume I**

**Doctoral School**

**Amirkabir University of Technology**
**Tehran Polytechnic)**
**Department of Textile Engineering**

## Doctoral Program in Science

# Development of perovskite optoelectronic devices on flexible substrates

Author
**Ehsan Hassanabadi**

Supervisors
**Iván Mora Seró** **Masoud Latifi**

March 2022

## Doctoral Programme in Science

**Universitat Jaume I Doctoral School**

**Doctoral School**

**Amirkabir University of Technology**

**Department of Textile Engineering**

# Development of perovskite optoelectronic devices on flexible substrates

**Report submitted by Ehsan Hassanabadi in order to be eligible for a doctoral degree awarded by the Universitat Jaume I**

| Author | Supervisor | Supervisor |
|---|---|---|
| 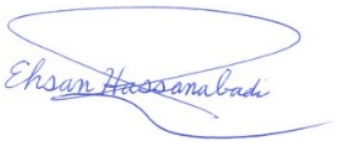 | Firmado por IVAN MORA SERO - NIF:***5368** el día 13/05/2022 con un certificado emitido por ACCVCA-120 | 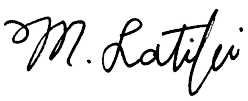 |
| Ehsan Hassanabadi | Iván Mora Seró | Masoud Latifi |

Castelló de la Plana, March 2022

## 1. CREATIVE COMMONS (CC) LICENCES FOR THESES



## 2. Funding

- **NO-Limit** (boosting photovoltaic performance by the synergistic interaction of halide perovskites and semiconductor quantum dots)

- **DROP-IT** (Drop-on Demand Flexible Optoelectronics and Photovoltaics by means of Lead-Free Halide Perovskites)

**Publications included in this thesis**

1. Suárez, Isaac*[1], Ehsan Hassanabadi*, Alberto Maulu, Niccolò Carlino, Cecilia Ada Maestri, Masoud Latifi, Paolo Bettotti, Iván Mora-Seró, and Juan P. Martínez-Pastor. "Integrated Optical Amplifier–Photodetector on a Wearable Nanocellulose Substrate." *Advanced Optical Materials* 6, no. 12 (2018): 1800201.
2. Zolfaghari, Zahra, Ehsan Hassanabadi, Didac Pitarch-Tena, Seog Joon Yoon, Zahra Shariatinia, Jao van de Lagemaat, Joseph M. Luther, and Iván Mora-Seró. "Operation mechanism of perovskite quantum dot solar cells probed by impedance spectroscopy." *ACS Energy Letters* 4, no. 1 (2018): 251-258.
3. Hassanabadi, Ehsan, Masoud Latifi, Andrés F. Gualdrón-Reyes, Sofia Masi, Seog Joon Yoon, Macarena Poyatos, Beatriz Julián-López, and Iván Mora-Seró. "Ligand & band gap engineering: Tailoring the protocol synthesis for achieving high-quality $CsPbI_3$ quantum dots." *Nanoscale* 12, no. 26 (2020): 14194-14203.

[1] equal contribution

**Publications not included in this thesis**

1. Salim, KM Muhammed*, Ehsan Hassanabadi*, Sofia Masi, Andrés F. Gualdrón-Reyes, Marius Franckevicius, Andrius Devižis, Vidmantas Gulbinas, Azhar Fakharuddin, and Ivan Mora-Sero. "Optimizing performance and operational stability of CsPbI3 quantum-dot-based light-emitting diodes by interface engineering." *ACS Applied Electronic Materials* 2, no. 8 (2020): 2525-2534.

2. Marand, Zahra Rezay, Ahmad Kermanpur, Fathallah Karimzadeh, Eva M. Barea, Ehsan Hassanabadi, Elham Halvani Anaraki, Beatriz Julián-López, Sofia Masi, and Iván Mora-Seró. "Structural and Electrical Investigation of Cobalt-Doped NiOx/Perovskite Interface for Efficient Inverted Solar Cells." *Nanomaterials* 10, no. 5 (2020): 872.

3. Aeineh, Naemeh, Andrés-Felipe Castro-Méndez, Pedro J. Rodriguez-Cantó, Rafael Abargues, Ehsan Hassanabadi, Isaac Suarez, Abbas Behjat, Pablo Ortiz, Juan P. Martínez-Pastor, and Ivan Mora-Seró. "Optical optimization of the TiO2 mesoporous layer in perovskite solar cells by the addition of SiO2 nanoparticles." *ACS omega* 3, no. 8 (2018): 9798-9804.
4. Suárez, Isaac, Ehsan Hassanabadi, Alberto Maulu, Niccolò Carlino, Cecilia Ada Maestri, Masoud Latifi, Paolo Bettotti, Iván Mora-Seró, and Juan P. Martínez-Pastor. "Polymer Halide Perovskites-Waveguides Integrated in Nanocellulose as a Wearable Amplifier-Photodetector System." In 2018 20th International Conference on Transparent Optical Networks (ICTON), pp. 1-3. *IEEE*, 2018.

بِسۡمِ ٱللَّهِ ٱلرَّحۡمَٰنِ ٱلرَّحِيمِ

In The name of Allah, the Entirely Merciful, the Especially Merciful

# Table of Contents

Table of Contents

Table of Contents

# Table of Figures

Table of Figures

Table of Figures

# List of tables

# List of Abbreviations

| | |
|---|---|
| MHPs | metal halide perovskites |
| NC | nanocellulose |
| WG | waveguide |
| PSCs | Halide perovskite solar cells |
| QDs | quantum dots |
| PQDSC | perovskite QD solar cell |
| PQDs | perovskite QDs |
| IS | impedance spectroscopy |
| EQE | external quantum efficiency |
| IQE | internal quantum efficiency |
| LED | light emitting diode |
| OA | oleic acid |
| OLA | oleylamine |
| OLM | oleylammonium oleate |
| PL | Photoluminescence |
| FWHM | full width at half maximum |
| AFM | atomic force microscope |
| SEM | scanning electron microscopy |
| PMMA | poly(methyl methacrylate) |
| ASE | Amplified spontaneous emission |
| $I_{PC}$ | photocurrent |
| $I_{PL}$ | intensity of photoluminescence |
| $C_{LF}$ | low-frequency capacitance |
| $R_{rec}$ | recombination resistance |

| | |
|---|---|
| TEM | Transmission electron microscopy |
| XRD | X-ray diffraction |
| $J_{sc}$ | short circuit Current Density |
| $V_{oc}$ | Open Circuit Voltage |
| FF | Fill Factor |
| IPCE | incident photon-to-current conversion efficiency |
| $\eta$ | photoconversion efficiency |
| c-$TiO_2$ | compact layer of $TiO_2$ |
| FTO | fluorine-doped tin oxide |
| ITO | Indium tin oxide |
| NMR | Nuclear magnetic resonance |
| $^1$H NMR | Proton nuclear magnetic resonance |
| $^{13}$C NMR | Carbon-13 nuclear magnetic resonance |
| NOA | N-oleyl-oleamide |
| ppm | parts-per-million |
| QCR | quantum confinement regime |
| $K_r$ | radiative recombination decay rate constant |
| $K_{nr}$ | non-radiative recombination decay rate constant |
| L | luminance |
| $V_{ON}$ | turn-on voltage |
| m | ideality factor |
| CW | continuous wave |
| DMF | N,N-dimethylformamide |
| DMSO | dimethyl sulfoxide |
| MAI | methylammonium iodide |
| TEMPO | 2,2,6,6-tetramethylpiperidine-1-oxyl |

| | |
|---|---|
| Nd: Yag | neodymium-doped yttrium aluminum garnet |
| SMU | Source Meter Unit |
| 4-TBP | 4-tert-butylpridine |
| TMS | Tetramethylsilane |
| PEDOT:PSS | poly(3,4-ethylenedioxythiophene) polystyrene sulfonate |
| Poly-TPD | ), poly(N,N'-bis-4-butylphenyl-N,N'-bisphenyl)benzidine |
| TPBi | (2,2′,2"-(1,3,5-Benzinetriyl)-tris(1-phenyl-1-H-benzimidazole)) |
| TRPL | Time-resolved photoluminescence |
| HRTEM | High-resolution transmission electron microscopy |
| RF | Radio frequency |
| EL | Electroluminescence |
| DC | Direct current |
| PV | Photovoltaics |
| DSCs | dye-sensitized solar cells |
| IPCE | incident photon-to-current conversion efficiency |
| APCE | absorbed photon to current conversion efficiency |
| TCSPC | time-correlated single-photon counting |
| SPT | single-photon timing |
| ADC | analog-to-digital converter |
| FID | free induction decay |
| FT | Fourier transformation |
| HPLC | High-performance liquid chromatography |
| GC | Gas chromatography |
| Eth | effective ASE threshold |
| CIGS | copper indium gallium selenide |
| TM | Transverse Magnetic |

| | |
|---|---|
| TE | Transverse Electric |

رَبَّنَا تَقَبَّلۡ مِنَّآۖ إِنَّكَ أَنتَ ٱلسَّمِيعُ ٱلۡعَلِيمُ

**Our Lord, accept from us. Indeed, you are the Hearing, the knowing**

# Acknowledgement

I went through a very difficult period on the ups and downs of research. In this way, I am grateful to those who helped me. First of all, the Almighty God, who was my guide in all moments and made the impossible possible for me. From my supervisor, Professor Mora Sero, who closely followed the research process and benefited me from using their laboratory facilities and scientific guidance. Also, from my supervisor, Prof. Latifi, who helped me with his paternal support, and this would not have been possible without his cooperation and support. I would like to thank my research colleagues, Dr. Suarez, Dr. Zolfaghari, Dr. Masi, Dr. Julian and Dr. Guadron, Dr. Salim, as well as my former supervisor, the late Dr. Shoushtari, with whom I started this path.

Many thanks to my dear family, my parents and my wife's parents.

And finally, special thanks to my dear and devoted wife and to my little daughter Nazanin Zahra who supported and encouraged me.

# Abstract

In this thesis, first, the monolithic integration of a perovskite-based optical waveguide amplifier together with a photodetector on a nanocellulose substrate is shown to demonstrate the feasibility of a stretchable signal manipulation and receptor system fabricated on a biodegradable material. An integrated optical amplifier–photodetector is developed in which the photocurrent is exploited that is generated in the organic–inorganic lead halide perovskite under an applied bias. Such photocurrent does not minimally perturb the amplifier operation and is used to monitor the light signal propagating along the waveguide, opening a broad range of applications for example to measure the operation temperature.

Then, perovskite quantum dot solar cells (PQDSCs) were systematically investigated with impedance spectroscopy. Despite the evident structural differences with respect to standard perovskite solar cells (PSCs), similar impedance spectra were obtained for PQDSCs, pointing to similar working principles in terms of the active layer. Although there is no consensus about the exact mechanism responsible for low frequency capacitance, the suggested models point to an ion migration origin. Its observation in thin-film and PQDSCs devices implies a similar effect in both.

Finally, we synthesized ultra-high stable $CsPbI_3$ QDs by controlling two main parameters: synthesis temperature and the concentration of capping ligands. We achieved the maximum photoluminescence quantum yield (PLQY) of 93% for a synthesis conducted at 185 °C, establishing an efficient surface passivation. Under these optimized synthesis conditions, deep red LEDs with an External Quantum Efficiency (EQE) higher than 6% were achieved. We show that it is possible to produce stable $CsPbI_3$ QDs with high PLQY and red emission beyond the requirement of the Rec. 2020 standards for red color.

**Key Words:** flexible devices, nanocellulose, optical amplifiers, photodetectors, perovskites, quantum dots, solar cells, impedance spectroscopy, light emitting diodes, hot-injection synthesis

# چکیده

در این رساله، ابتدا، یکپارچه‌سازی موجبر، تقویت‌کننده و آشکارساز نوری پروسکایت حجیم $MAPbI_3$ بر روی نانوسلولز انجام شده است که در یک بایاس اعمال شده، جریان نوری‌ای مورد بهره‌برداری قرار می‌گیرد که چنین جریان نوریی نه تنها عملکرد تقویت‌کننده را به حداقل نمی‌رساند بلکه برای نظارت بر انتشار سیگنال نوری در امتداد موجبر استفاده می‌شود و طیف گسترده‌ای از کاربردها به عنوان مثال تنظیم دمای کاری را امکان‌پذیر می‌کند.

در ادامه سلول‌های خورشیدی پروسکایتی نقطه‌های کوانتومی به‌طور نظام‌مند با طیف‌سنجی امپدانس بررسی شدند. با وجود تفاوتهای ساختاری آشکار در رابطه با سلول‌های خورشیدی پروسکایتی معمولی، طیف‌های امپدانس مشابهی برای سلول‌های خورشیدی پروسکایتی نقطه‌های کوانتومی به‌دست آمد که از نظر لایه فعال به اصول کار مشابهی اشاره دارد. اگر چه درباره سازوکار دقیق مسئول ظرفیت بسامد پایین اتفاق نظر وجود ندارد، اما مدلهای پیشنهادی به منشأ مهاجرت یونی اشاره دارند.

در پایان با پایش دو شاخص اصلی سنتز، دما و غلظت لیگاندهای پوشش‌دهنده، نقطه‌های کوانتومی $CsPbI_3$ با پایداری فوق‌العاده بالا سنتز کردیم. ما حداکثر عملکرد کوانتومی فوتولومینسانس ۹۳٪ را با ایجاد یک پوشش‌دهی سطح کارا برای یک سنتز انجام شده در دمای ۱۸۵ درجه‌ی سانتی‌گراد به‌دست آوردیم. تحت این شرایط سنتز بهینه شده، دیودهای ساطع‌کننده‌ی نور قرمز عمیق با عملکرد خارجی کوانتومی بالاتر از ۶٪ به‌دست آمد، که نشان می‌دهد امکان تولید نقطه‌های کوانتومی $CsPbI_3$ پایدار با عملکرد کوانتومی فوتولومینسانس بالا و انتشار قرمز بیش از نیاز معیارهای Rec ۲۰۲۰ برای رنگ قرمز وجود دارد.

## واژه‌های کلیدی

ابزارهای انعطاف‌پذیر، نانوسلولز، تقویت‌کننده‌های نوری، آشکارساز های نوری، پروسکایت، نقطه‌های کوانتومی، سلول‌های خورشیدی، طیف‌سنجی امپدانس، دیودهای ساطع‌کننده‌ی نور، سنتز تزریق گرم

# Resumen

En esta tesis, en primer lugar, se muestra la integración monolítica de un amplificador de guía de ondas óptico basado en perovskita junto con un fotodetector en un sustrato de nanocelulosa para demostrar la viabilidad de un sistema de manipulación y receptor de señal extensible fabricado en un material biodegradable. Se desarrolla un amplificador-fotodetector óptico integrado en el que se aprovecha la fotocorriente que se genera en la perovskita de haluro de plomo orgánico-inorgánico bajo un potencial aplicado. Dicha fotocorriente no perturba mínimamente el funcionamiento del amplificador y se utiliza para monitorizar la señal de luz que se propaga a lo largo de la guía de ondas, abriendo una amplia gama de aplicaciones, por ejemplo para medir la temperatura de funcionamiento.

Luego, las células solares de puntos cuánticos de perovskita (PQDSC) se investigaron sistemáticamente con espectroscopía de impedancia. A pesar de las evidentes diferencias estructurales con respecto a las células solares de perovskita estándar (PSC), se obtuvieron espectros de impedancia similares para las PQDSC, lo que apunta a principios de trabajo similares en términos de la capa activa. Aunque no hay consenso sobre el mecanismo exacto responsable de la capacitancia de baja frecuencia, los modelos sugeridos apuntan a un origen de migración de iones. Su observación en dispositivos de película fina y PQDSCs implica un efecto similar en ambos.

Finalmente, sintetizamos QD de $CsPbI_3$ con establilidades ultraaltas controlando dos parámetros principales: la temperatura de síntesis y la concentración de ligandos de protección. Logramos el rendimiento cuántico de fotoluminiscencia máximo (PLQY) del 93% para una síntesis realizada a 185 ° C, estableciendo una pasivación superficial eficiente. En estas condiciones de síntesis optimizadas, se lograron LED de color rojo intenso con una eficiencia cuántica externa (EQE) superior al 6%. Demostramos que es posible producir $CsPbI_3$ QD estables con un PLQY alto y una emisión de rojo más allá del requisito de la Rec. Estándares 2020 para el color rojo.

Palabras clave: dispositivos flexibles, nanocelulosa, amplificadores ópticos, fotodetectores, perovskitas, puntos cuánticos, células solares, espectroscopia de impedancia, diodos emisores de luz, síntesis de inyección en caliente

# 1. Fundamentals and concepts

## 1.1. Structural Characterization

### 1.1.1. X-ray diffraction

Powder X-ray diffraction (pXRD) is a fast and inexpensive method that can be used to determine numerous structural properties of a material. To perform pXRD, X-ray with a fixed wavelength is fired at a sample and X-rays that are diffracted from the sample are detected. The detector and X-ray source are moved around the sample changing the angle between the incident beam and the detector (2θ) and a plot of intensity against 2θ is formed. This intensity vs 2θ plot can be used to compare with a database of diffraction patterns and can also give the distance between symmetry planes in the crystal. The relation between the diffraction angle (θ) and the distance between symmetry planes ($d_{hkl}$) is given by Bragg's law (Equation 1.1.1), where λ is the wavelength of the X-rays. [1]

$$\boldsymbol{\lambda = 2d_{hkl}sin\theta} \qquad \textbf{1.1.1}$$

When parallel atoms with an even $d_{hkl}$ space diffract X-rays, they will positively interfere with each other causing a diffraction peak. The different planes must be properly aligned with the incident X-rays for a peak to be shaped. A single crystal would produce a different diffraction pattern dependent on the orientation of the planes but for a bulk powder this orientation specific diffraction can be effectively neglected since the crystals are randomly oriented so all of the planes would have some crystals aligned properly to form a diffraction peak.

Other valuable information that can be collected from pXRD is the average crystallite size. By means of the full width at half maximum (FWHM) (Δ) and the Scherrer equation (Equation 1.1.2) the crystallite size (T) can be calculated. [2] In the below equation T is the crystallite size, K is the shape factor, λ is the wavelength of the incident X-ray, Δ is the FWHM and θ is the diffraction angle.

$$\mathbf{T} = \frac{\mathbf{K}\boldsymbol{\lambda}}{\boldsymbol{\Delta cos\theta}} \qquad \textbf{1.1.2}$$

According to the Scherrer formula narrower peaks mean bigger crystals, but there are other factors that influence peak width so the results of the Scherrer formula should be considered as an estimate.

### 1.1.2. Scanning electron microscopy (SEM)

Owing to the resolution limit of optical microscopes, scanning electron microscopy (SEM) is a suitable method to characterize surfaces and morphologies at the nanometer

scale.[3]This is because of the wavelength dependence of the resolution limit given in Equation 1.1.3:

$$d = \frac{\lambda}{2NA} \qquad 1.1.3$$

Where d is the resolution limit, λ is the wavelength of the incident photons and NA the numerical aperture. Assuming a typical NA between 1 and 1.5 and a wavelength of about 550 nm, which is typically applied in fluorescence microscopy, a diffraction limit d of about 200 nm can be attained.[4, 5] On the contrary, SEM permits for spatial resolution close to one nanometer.[6] The important parts of an SEM are shown in Figure 1.1.1

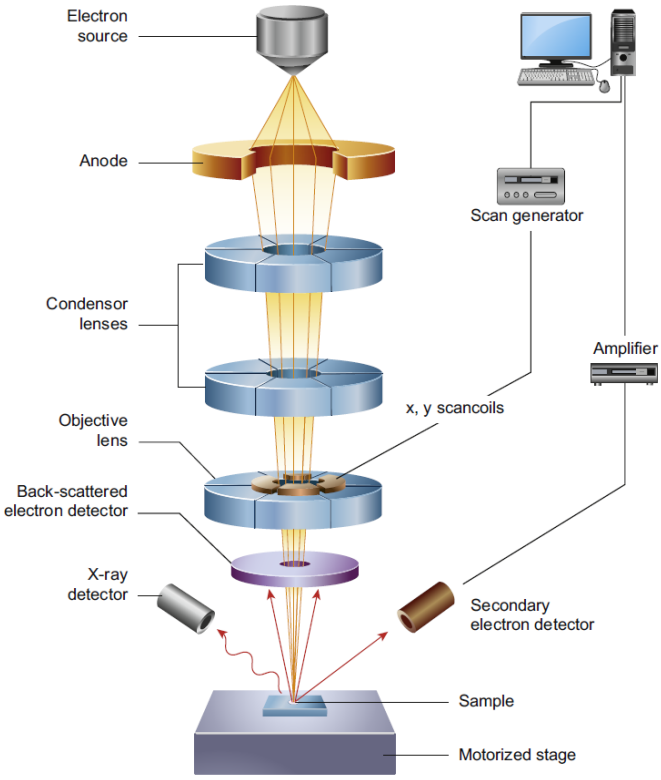


**Figure 1.1.1 Schematic diagram of the main parts of an SEM microscope reprinted with permission from [7]**

### 1.1.3. Transmission electron microscopy (TEM)

Transmission electron microscopy (TEM) has long been applied as an important characterization method in the area of material science. A key feature of TEM is the probable resolution provided by an accelerated electron beam with operative wavelengths that are smaller by a factor of $10^5$ than visible light. In this method, an image is formed by the interaction of electrons with the sample as beam is transmitted through the specimen. The image is then focused on the imaging device such as photographic film or fluorescent

screen after magnification. Transmission electron microscopes can produce high-resolution images in comparison with the light microscope, as a result of the smaller wavelength of electrons. The main parts of TEM instrument are shown in Figure 1.1.2, which consist of electron source, electromagnetic lenses, electrostatic plates and vacuum system [8].

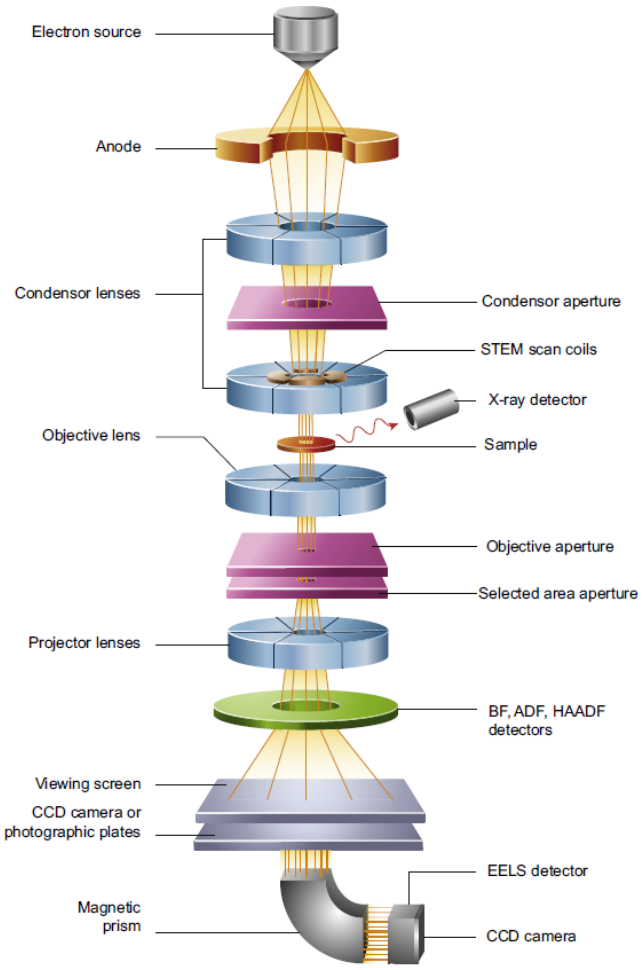


**Figure 1.1.2 Schematic of main components of a TEM microscope reprinted with permission from [7]**

## 1.2. Optical Characterization

### 1.2.1. Absorbance

In steady-state absorption spectroscopy, a sample is illuminated by a monochromatic beam from a continuous light source. The reduction of beam intensity as it passes through the sample is measured over a range of incident wavelengths.

$$A = -\log_{10}\frac{I}{I_0} = \varepsilon l c \qquad 1.2.1$$

Transmittance, $\varepsilon$ is the molar extinction coefficient, $I_0$ is the intensity of incident monochromatic beam, $I$ is the intensity of the transmitted beam, $c$ is the sample concentration and l is the path length of the sample. The equation is effective for dilute solutions where $\varepsilon$ is independent of sample concentration. For concentrated solutions (> $10^{-2}$ mol $L^{-1}$), $\varepsilon$ depends meaningfully on the refractive index of the solution and the linear relation between absorbance and sample concentration is no longer valid.

Optical absorption is a measure of an interaction between the incident electromagnetic (EM) radiation and the sample that energy transfer initiates system perturbation enabling specific molecular movements from the far to near infrared regions and electron transitions (i.e. trap state excitations, state-to-state and band-to-band transitions) from the near infrared to ultraviolet realms. Those salient features allow to identify functional groups in organic compounds (by Fourier-transform infrared spectroscopy) and to investigate optical transitions related to excitonic states and free carriers in semiconductor materials (by UV-visible absorption spectroscopy). The incident radiation ($I_0$) exponentially attenuates in specimen in response to its concentration (c), absorption coefficient (ε) and absorbing path (l). The physical quantity is called absorbance (A) and described by Beer-Lambert Law.

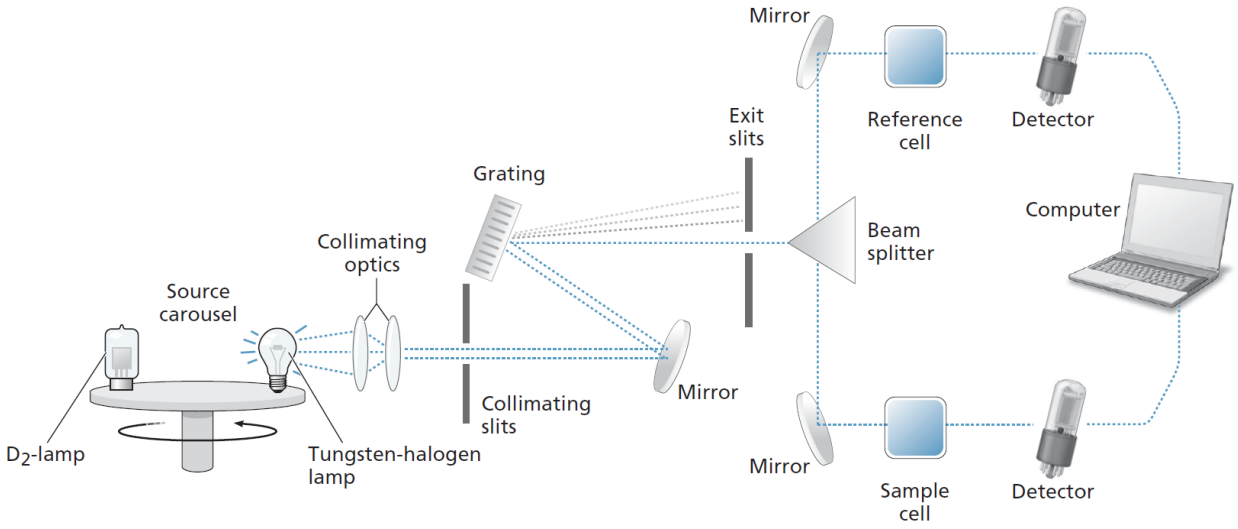


**Figure 1.2.1 Schematic of a dual-beam spectrophotometer. reprinted with permission from [9]**

### 1.2.2. Steady state Photoluminescence

Photoluminescence (PL) generally relates to a subsequent radiative relaxation through luminescence after optical excitation, which reveals characteristic electronic transitions in organic compounds and semiconductors.[10]

Jablonski diagram is used to explain the multiple electronic transitions involving singlet excited states and triplet excited states Figure 1.2.3) [11]. Due to the presence of triplet excited states and spin-orbit coupling, the singlet excited states can transfer to triplet excited state via intersystem crossing. The radiative recombination of excitons from singlet states is called fluorescence, which generally happens in a short time period (nanosecond scale); the radiative recombination of excitons from triplet states is called named phosphorescence, which may last from microseconds to millisecond or even several seconds as a result of the spin forbidden transition back to ground states.

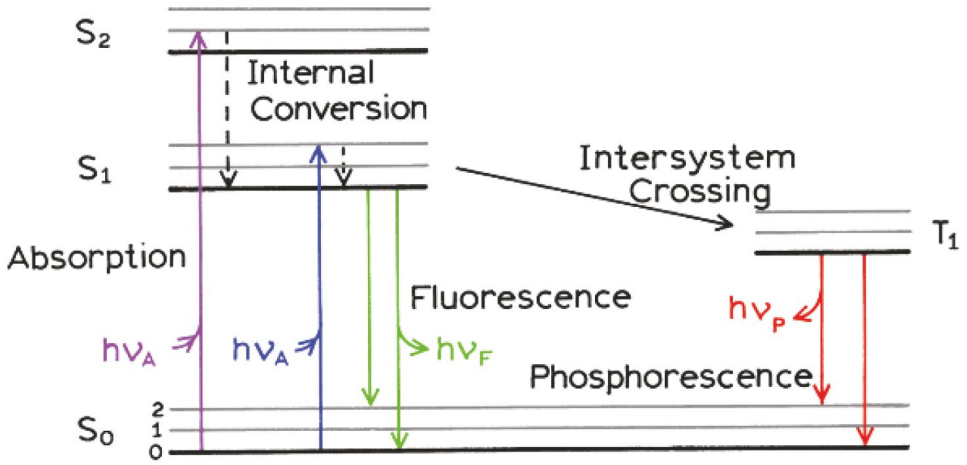


**Figure 1.2.2 Jablonski diagram for illustration of photoluminescence process reprinted with permission from [12]**

In steady-state PL, samples are photoexcited at specific wavelengths, and the light scattered from the sample are collected by a photodetector.[13] The detector disperses the obtained spectra as function of wavelength and records the intensity at each wavelength. Since in the Photoluminescence analysis the sample is excited optically, this method is nondestructive. Fundamentally, the limitation of Photoluminescence analysis is its dependence on radiative events. Materials with poor radiative efficiency, such as low-quality semiconductors with indirect bandgaps, are hard to investigate through normal Photoluminescence technique.[14]

### 1.2.3. Photoluminescence decay

While steady-state Photoluminescence measurement is simple, nanosecond time-resolved Photoluminescence (TRPL) measurement typically requires complex and expensive instrumentation, but contains more information than is available from the steady-state data.

With the advent of fast detectors and ultrafast laser sources, time-resolved photoluminescence (TRPL) techniques have emerged as useful tools to understand a wealth of dynamic processes including purity of the sample as well as the donor-to-acceptor distance. [12] charge and energy relaxation, recombination, and transfer.[15]

The most popular technique TRPL is based on the time-correlated single-photon counting (TCSPC) method, better called as single-photon timing (SPT). The basic principle relies on the fact that the probability of detecting a single photon at time t after exciting pulse is proportional to the fluorescence intensity at that time.[16] so, for low-level, high-repletion rate signals the light intensity is usually low enough that not only, the probability to detect more than one photon in one signal period is negligible [17] but also the probability of detection one photon in one signal period is far less than one. Therefore, it is not necessary to provide for the possibility of detecting several photons in one signal period. It is sufficient to record the photons, measure their time in the signal period, and build up a histogram of the photon times, [18] to an extent where the error due to counting statistics becomes negligible. [19]

After timing and recording the single photons following a large number of exciting pulses, the fluorescence intensity decay curve is reconstructed. [16]

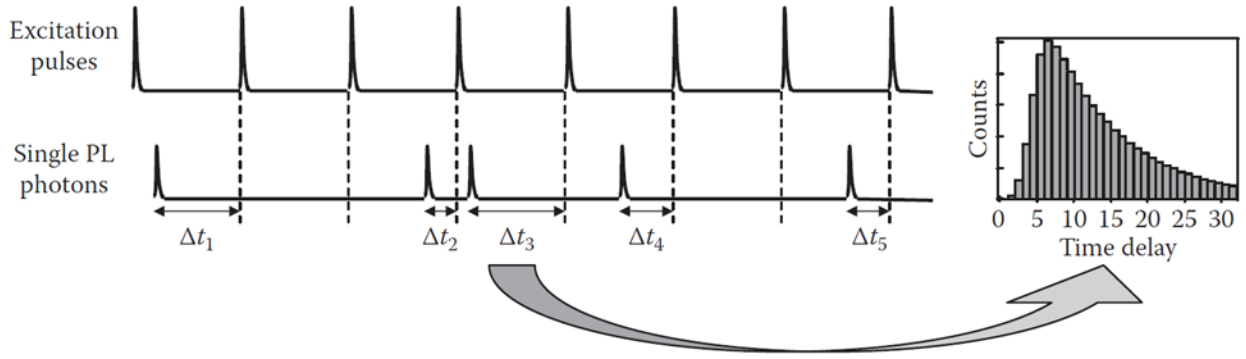


**Figure 1.2.3 in TCSPC, the time delays of single emitted photons are recorded and used to generate a histogram. reprinted with permission from [15]**

### 1.2.4. Photoluminescence Quantum Yield

The photoluminescence quantum yield (PLQY) is an important measure of luminescent materials. Referring to the number of emitted photons per absorbed photons. In electro-luminescent devices, maximizing the external quantum efficiency is often the driving motivation. Besides the careful engineering of the device architecture and electric performance, the efficiency directly depends on the inherent efficiency of the luminescent materials used. Due to the direct accessibility, this efficiency is normally quantified in photoluminescent experiments, rather than in electroluminescent ones, leading to the photoluminescence quantum yield (PLQY Therefore, when designing new materials, the PLQY is one key performance indicator [20]

$\Phi_f$ can be determined fluorometrically either relative to a fluorescent standard with a known fluorescence quantum yield, respectively, or absolutely (method 2) measuring the number of emitted photons $N_{em}$ per number of absorbed photons $N_{abs}$; see equation 1.2.2:

$$\boldsymbol{\Phi_f = \frac{N_{em}}{N_{abs}}} \qquad \textbf{1.2.2}$$

In the majority of cases, method 1a is employed because of its comparative simplicity, low costs, and high sensitivity. This procedure is often regarded as being established, for the simplest case of transparent dilute solutions of small organic dyes The most straightforward method for the determination of $\Phi_f$ values presents the absolute measurement of $N_{abs}$ and $N_{em}$ in equation 1.2.2 with an integrating sphere setup (method 2).This circumvents uncertainties related to the use of fluorescence standards inherent to all relative methods; also, this is the only fluorometric method suitable for measurements of $\Phi_f$ values of scattering systems. The fluorescence quantum yields were calculated from the spectra of the blank (solvent-filled cuvette) and the sample according to equation 1.2.2 using a procedure implemented by the instrument manufacturer. The measurement of absolute fluorescence quantum yields of dilute dye solutions according to equation 1.2.2 with the commercialized integrating sphere setup consists of the following steps:

(i) determination of the of the excitation light peak ($I_x(\lambda_{ex})$) and the emitted light ($I_x(\lambda_{em})$) of the sample and a blank (solvent-filled cuvette; ($I_b(\lambda_{ex})$) ; ($I_b(\lambda_{em})$) under identical measurement conditions (e. g., excitation wavelength, temperature), each within a single scan,

(ii) (ii) data evaluation including choice of the excitation and emission wavelength region used for signal integration and spectral emission correction;

(iii) (iii) calculation of the fluorescence quantum yield based upon equation 1.2.3, using the software of the instrument manufacturer Hamamatsu.

$$\boldsymbol{\Phi_f} = \frac{\int_{\lambda_{em1}}^{\lambda_{em2}} \frac{(I_x(\lambda_{em}) - I_b(\lambda_{em}))}{s(\lambda_{em})} \boldsymbol{\lambda_{em} d\lambda_{em}}}{\int_{\lambda_{ex}-\Delta\lambda}^{\lambda_{ex}+\Delta\lambda} \frac{(I_b(\lambda_{ex}) - I_x(\lambda_{ex}))}{s(\lambda_{ex})} \boldsymbol{\lambda_{ex} d\lambda_{ex}}} = \frac{\mathrm{N}_{em}}{N_{abs}} \qquad \textbf{1.2.3}$$

$\mathrm{N}_{em}$ is obtained upon integration of the blank-corrected (subtraction of $(I_b(\lambda_{em}))$ and spectrally corrected emission spectrum of the sample $(I_x(\lambda_{em}))$. $N_{abs}$ follows from the integrated difference between the excitation light resulting from measurements with the blank $(I_b(\lambda_{ex}))$ and the sample $I_x(\lambda_{ex})$. [21]

## 1.3. Electrical Characterization

### 1.3.1. Current density-voltage characteristic

The acquisition of current–voltage (I-V) curves is the most basic method to characterize the electrical behavior of a solar cell. For an ideal pn-junction solar cell, the dependency of the current density on voltage would be given the Shockley equation

$$\boldsymbol{J(V) = J_0 \cdot \left[exp\left(\frac{eV}{k_B T} - 1\right)\right] - J_{Ph}} \qquad \textbf{1.3.1}$$

Therein, e is the elementary charge, V is the applied voltage, $k_B$ is the Boltzmann constant, T is the temperature, and $J_0$ is the so-called reverse saturation current density, i.e., the current density flowing through the diode under dark condition, if a (relatively high) reverse bias is applied. In the dark, ( $J_{Ph} = 0$) a solar cell should behave like a diode Under illumination, a photocurrent is generated. The photocurrent, treated as a positive quantity and denoted $J_{Ph}$ (as a current density), flows in the opposite direction as the current due to the injection of charge carriers by a positive applied voltage

The J-V curve under illumination contains several characteristic points. At zero voltage, no current is injected by an external voltage source. The current is then purely due to current generation by the conversion of solar energy. At this point, the current density is called the short-circuit current density, $J_{SC}$. At a certain positive voltage, the injection current compensates the photocurrent, so that no net current is flowing. The voltage at this point is called the open-circuit voltage, $V_{OC}$. However, deviations from the behavior of an ideal diode should be taken into account. Often, this can be done by assuming an equivalent circuit model, where a series and a parallel resistance are introduced. The series resistance, $R_S$, represents resistive losses, e.g., due to barriers at interfaces and contacts. For an ideal solar cell, the series resistance should be zero. The parallel resistance, $R_P$, takes into account that the current may find an alternative path in a real solar cell, e.g., if contact

materials penetrating into the organic layers lead locally to shorts (also called shunts). The parallel resistance, sometimes also called shunt resistance, should be infinite in an ideal solar cell. so, the following relationship between the current density and voltage can be deduced:

$$\boldsymbol{J(V) = \frac{1}{1+R_S/R_P} \cdot \left[J_0 \cdot \left[exp\left(\frac{e\cdot(V-JR_SA)}{nk_BT}\right) - 1\right] - \left(J_{Ph} - \frac{V}{R_PA}\right)\right]} \qquad \textbf{1.3.2}$$

Equation (1.3.2) is sometimes referred to as the enhanced Shockley equation. Therein, A denotes the area of the device, and n is the so-called ideality factor of the diode. For an ideal diode, n should equal 1. Another important quantity is the power delivered by the solar cell. Power is the product of voltage and current, and it depends on the voltage applied, how much power is obtained. At a certain voltage, a maximum is obtained. This point of operation is called the maximum power point (MPP). With $J_{MPP}$ and $V_{MPP}$ denoting the current density and voltage at the maximum power point, respectively, one can furthermore define the fill factor (FF):

$$\boldsymbol{FF = \frac{J_{MPP}\cdot V_{MPP}}{J_{SC}\cdot V_{OC}}} \qquad \textbf{1.3.3}$$

The fill factor describes how 'rectangular' the J-V curve is. For solar cells with high fill factor, $J_{MPP}$ and $V_{MPP}$ have to approach $J_{SC}$ and $V_{OC}$, respectively. The shape of the current–voltage curve will then become more and more rectangular. To calculate the power conversion efficiency (PCE, η), the power delivered by the device has to be divided by the incident power from the sunlight ($P_{light}$):

$$\boldsymbol{PCE = \frac{J_{MPP}\cdot V_{MPP}}{P_{light}} \cdot 100\%} \qquad \textbf{1.3.4}$$

Using the definition of the fill factor, the efficiency can also be expressed by [22]

$$\boldsymbol{PCE = \frac{FF\cdot J_{SC}\cdot V_{OC}}{P_{light}} \cdot 100\%} \qquad \textbf{1.3.5}$$

### 1.3.2. Incident photon to current efficiency (IPCE)

Another PV parameter, which is routinely employed to determine the quality of a PV device, is the external quantum efficiency (EQE), usually referred to as the incident photon-to-current conversion efficiency (IPCE) by the DSCs community. $IPCE(\lambda)$ is defined as the number of collected electrons under short circuit conditions per number of incident photons at a given excitation wavelength λ and gives the ability of a cell to generate current as a function of the wavelength of the incident monochromatic light. IPCE is calculated by

measuring the short-circuit photocurrent as a function of the monochromatic photon flux. [23]

$$\boldsymbol{IPCE(\lambda) = \frac{J_{sc}(\lambda)/e}{P_{in}(\lambda)/hv} = \frac{hc}{\lambda e}\frac{J_{sc}(\lambda)}{P_{in}(\lambda)} = \frac{1240}{\lambda}\frac{J_{sc}(\lambda)}{P_{in}(\lambda)}} \qquad \textbf{1.3.6}$$

The IPCE can be used to estimate the maximum obtainable photocurrent under AM 1.5 irradiation by the following relationship:

$$\boldsymbol{J_{AM\,1.5} = \int (IPCE_{\lambda} \times \Phi_{\lambda} \times e) d\lambda} \qquad \textbf{1.3.7}$$

Where $J_{AM\ 1.5}$ is the total photocurrent density under solar irradiation (mA/cm$^2$), $\Phi_\lambda$ is the photon flux of the solar irradiation (photons/(m$^2$s)), and e is the elementary charge (C). While this is not a direct or 100 % accurate way to estimate the photocurrent density of a material under AM 1.5 solar irradiation, it can give a close estimate if a solar simulator is not available in a particular laboratory, and only IPCE testing equipment is available. A correlation between IPCE (integrated photocurrent) and information provided by J–V measurements is essential for ensuring consistency of measurements.

The IPCE measures the total amount of electrons converted from all of the incident photons (broken down into individual wavelengths), and thus is useful to estimate the maximum possible current that can be extracted by a photon source. However, this technique inherently takes into account all of the photons that are incident on a photoelectrode (i.e., light that is either reflected or transmitted through the sample) and converted to usable (i.e., able to drive the water redox reactions) electrons. This is certainly not the case for a practical semiconductor material, and therefore it is also useful to normalize the IPCE by the absorbed spectrum of a sample, which results in the absorbed photon to current conversion efficiency (APCE), or internal quantum efficiency (IQE).

$$\boldsymbol{APCE = APCE(\lambda) = IQE(\lambda) = \frac{IPCE}{A_{\lambda}} = \frac{|j_{ph}(mA/cm^2)| \times hc(Vm)}{P_{\lambda}(mW/cm^2) \times \lambda(nm) \times A_{\lambda}}} \qquad \textbf{1.3.8}$$

Where $A_\lambda$ is the absorptance as a function of wavelength. The APCE is primarily used as a tool to determine the optimal thickness of a material to maximize the light-absorbing path length through a semiconductor. [24]

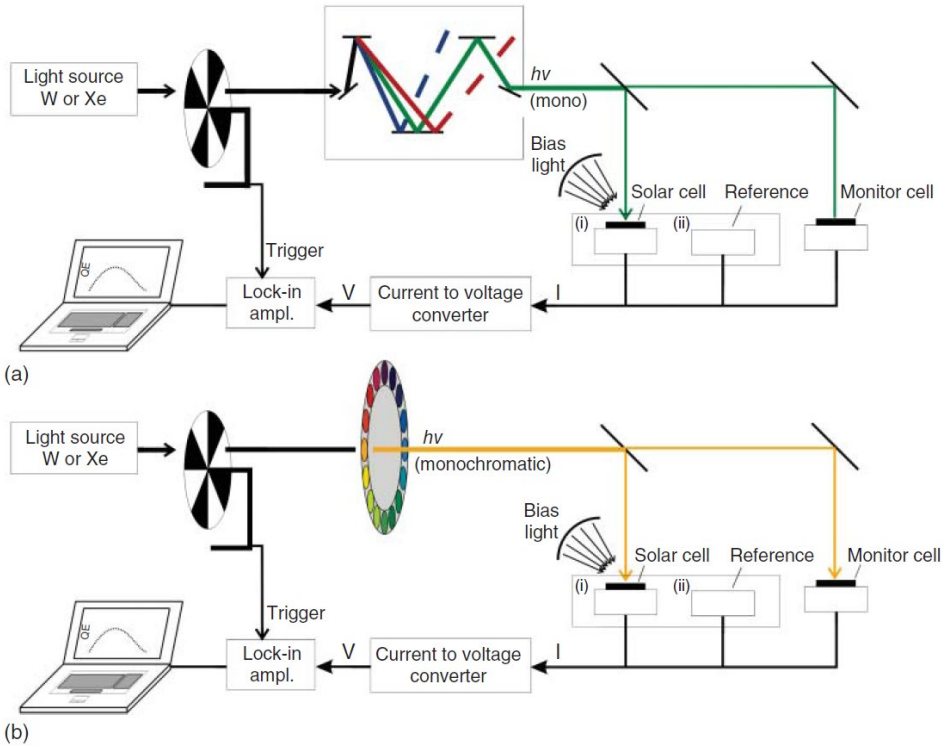


**Figure 1.3.1 Scheme of two quantum efficiency setups – (a) a monochromator-based setup and (b) a setup with a filter wheel. In both cases, chopped monochromatic light illuminates first the reference (during calibration) and then the sample (during measurement). The current output of reference or sample is converted to voltage and then amplified with a lock-in amplifier triggered by the chopper wheel synchronization output. Temporal variations in intensity of the monochromatic light can be monitored with a monitor diode measuring intensity during calibration and during measurement. reprinted with permission from [25]**

### 1.3.3. External quantum efficiency (EQE%)

The external quantum efficiency (EQE), the most important metrics to determine LED performance, is defined as the ratio of photons that escape the LED to the number of electrons flowing in the external circuit. To properly quantify the EQE at a given current density (J), there are three approaches, each of which is in principle equivalent, provided the measurements are performed carefully with appropriate calibration. A first approach utilizes a large photodetector at close proximity to the LED to collect the photons emitted in the forward. A second approach to measure the EQE is by collecting all photons in the forward-emitting hemisphere through use of an integrating sphere in a $2\pi$ geometry and a spectrometer. A third approach is to place the photodetector at a large distance compared with the dimensions of the emitting area and the thickness of the device. To accurately determine the emission quantum efficiency in each case, it is essential to account for the spectral-dependent losses caused by any element of the measurement set-up placed

between the LED and the photodetector. Likewise, one must perform a careful spectral response calibration of the photodetector at the device emission wavelengths; this of course first necessitates a measurement of the electroluminescence (EL) spectrum using a spectrometer. In the case of emitters having a broad emission spectral spread, the average responsivity of the photodetector weighted by the emission spectrum should be used. One may also consider the use of a well-calibrated spectroradiometer as an alternative to a calibrated photodetector, and the experimenter can then determine the EQE through accurate measurement of the device active area; this approach is widely employed in industry. In any case, any measurement set-up including a detector must be carefully and regularly calibrated. Quantum efficiency values must be quoted in context with the carrier density under which they are measured. The internal quantum efficiency (IQE) is defined as the ratio of photons generated within the device to the number of charge carriers injected. It is related to the EQE through the extraction efficiency, which is the ratio of photons escaping the device to those generated. Furthermore, the performance of some novel LED structures is substantially influenced by additional internal processes such as efficient photon recycling, for example in many of those based on crystalline semiconductors, including the halide perovskites, which exhibit small Stokes shifts between absorption and emission energies. These phenomena have an important impact on both the IQE and EQE because the opportunity for forward emission is substantially increased due to the larger number of absorption and re-emission events taking place within the device. Further information about the internal processes of the device can be ascertained by correlating the EL and EQE with their photoinduced counterparts — photoluminescence (PL) and photoluminescence quantum efficiency (PLQE). Efforts to quantify the IQE and extraction efficiency precisely are needed to unravel the working principles of the LED and to understand how close (or far) a particular emitter and device stack combination is to (or from) maximum performance. [26]

$$\boldsymbol{EQE(V) = \frac{N_{phot(V)}e}{I(V)} \times \frac{a^2+L^2}{a^2} \times 100} \qquad \textbf{1.3.9}$$

where, $I(V)$ is the current passing through the device at an applied bias, V, $N_{phot(V)}$ represents the number of emitted photons collected by the photodiode, a is the diameter of the active area of the photodiode and L represent the distance between the emitting pixel and the active area. $N_{phot(V)}$ was calculated from the photocurrent ($I_{Ph}$) of the photodiode in response to the measured EL at each bias, accounting for the wavelength dependence of the responsivity, R(λ), of the photodiode. [27]

### 1.3.4. Impedance spectroscopy

Impedance spectroscopy (IS) is a extensively used technique that extracts dynamic operating parameters on complete solar cells. [28] In this technique, a small ac perturbation (i.e. 20 mV) is applied to the working device using a wide range of frequencies (megahertz to millihertz) and the differential current output is measured. This method is carried out on a particular steady-state determined by dc bias, in specified illumination conditions, and allows us to probe different positions in the J−V curve by changing dc bias.[29] This method shows well-resolved arcs in the complex impedance plot for electronic and ionic processes taking place at different characteristic times.[29] There are two main types of representation to analyze the IS data. One is the complex impedance plot,-which reveals different arcs when the processes are well-separated with respect to frequency. This is an important method to identify the dynamic features of the system. The complex impedance plot ($Z'$, $-Z''$) directly shows resistance values by measuring the width of arc in the real axis. Alternatively, another important representation is the capacitance−frequency (C−f) plot that shows the general evolution of capacitive processes. Note that the capacitance representation is just a rephrasing of the impedance data. Complex capacitance is defined as

$$\boldsymbol{C(\omega) = \frac{1}{i\omega Z(\omega)}} \qquad \textbf{1.3.10}$$

Here, ω is the angular frequency related to the frequency as f =ω/2π. Capacitance in the C−f plot is the real part of the complex capacitance. This is a general view of the capacitive response, but specific capacitive processes, and the quantitative capacitance value, need to be obtained by fitting to an equivalent circuit model. [29] A very simple equivalent circuit that accounts for the physical processes taking place in a high-performance solar cell is represented in Figure 1.3.2 A. In this model, the resistance $R_3$ is coupled to $C_{bulk}$, which corresponds to the high-frequency arc. $R_1$ and $C_1$ represent the parameters associated with the contacts to the perovskite.

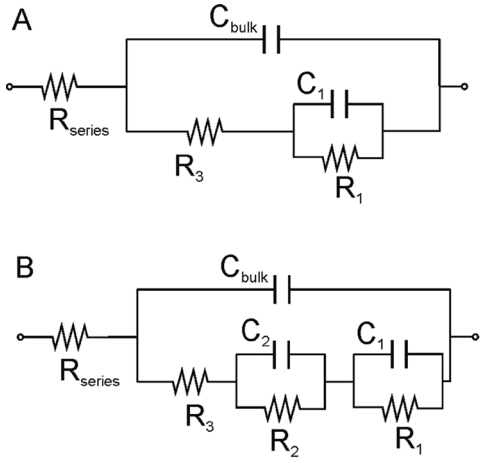


**Figure 1.3.2 (A) Equivalent Circuit for the Analysis of Perovskite Solar Cells Consisting of Bulk and Interface Components, (B) Advanced Circuit with Extended Interfacial Structure [29]**

The capacitance $C_{bulk}$ is mostly related to the intrinsic dielectric relaxation of the bulk perovskite layer. More generally, this capacitance is dominated by the geometric capacitance and may contain components of contact layers responding in a very high-frequency domain. Even if circuit A in many cases is appropriate to describe devices with the best performing contacts, in more general circuit (Figure 1.3.2 B), the aforementioned structure associated with the interface, $R_1C_1$ is modified considering additional kinetic and charge storage processes happening at the interface represented by elements $R_2$ and $C_2$. This model can be applied to describe devices with less efficient external contacts.[29]

### 1.3.5. Electroluminescence

Electroluminescence (EL) is the conversion of electrical energy into optical energy by an electronic relaxation process. The EL in inorganic materials is classified into two groups: high-field EL and injection EL. High-field EL consists of excitation of luminescence centers by majority charge carriers accelerated under the action of strong electric (a.c. or d.c.) fields $\sim 10^6$ V/cm. This type of EL mechanism relies on inter- and intraquantum shell transitions at luminescent centers/ions. High-energy electrons raise the luminescent centers to the excited quantum states via impact ionization and/or impact excitation. The excited centers must eventually relax to ground state emitting photons, known as the radiative relaxation process. The electron excitation and radiative relaxation are atomic transitions localized at the luminescent center. Injection EL is where the light emission is generated by the direct injection and subsequent recombination of electron–hole pairs at a p–n homo-

or hetero-junction. This is the light generation mechanism in light emitting diodes (LEDs) and semiconductor lasers. The material need not be in direct contact with the electrodes and no net current passes through the materials. In injection EL, light is emitted upon recombination of minority and majority carriers across the band gap of crystals.

There are four fundamental processes in EL behavior which may lead to light emission. These processes are: (i) injection of charge carriers into the phosphor layer, (ii) acceleration of charge carriers to optical energies, (iii) excitation of luminescence centers by energetic electrons (impact excitation), and (iv) radiative relaxation of luminescent centers. The mechanism of EL behavior of materials, though with a slight difference, is almost the same.

The EL properties of luminescent centers (ions) are determined by their quantum mechanical properties through intershell (change of principal quantum number n) and intrashell (without change in n) electronic transitions following selection rules. There are three properties that are of primary importance: radiative kinetics, the cross-section for impact excitation, and radiative transition energy (color). The electrical energy supplied to the phosphor layer raises the luminescent center to its excited state. This center eventually relaxes to the ground state by dissipating the absorbed energy. The relaxation process may emit: (i) a photon (radiative relaxation), (ii) a phonon to the lattice (non-radiative dissipation of absorbed energy to the lattice), or (iii) transfer energy to another luminescent center. Transitions allowed by selection rules possess short decay times (about a nanosecond), whereas forbidden transitions are of long decay times (about a millisecond or longer). The internal quantum efficiency, defined as the ratio of the radiative relaxation to the total relaxation, decreases with the rise of temperature and is termed ‘thermal quenching’.

The mechanism of light generation in injection EL and high-field EL are quite different from each other. There are two methods with which injection of minority carriers can occur. In the first method, the injection occurs from an electrode (rectifying contact) into the crystal. The electrons are accelerated and excite the luminescence centers similar to the case of high-field EL. Only the source of electrons is different. This type of injection EL can be observed in single crystals of ZnS or in thin films that have contact with electrodes. In the second method, light emission occurs at a p–n junction. At thermal equilibrium, a depletion layer is formed and a diffusion potential $V_d$ across the junction is produced. When the p–n junction is forward-biased, the diffusion potential decreases to ($V_d$ — V) and the electrons are injected from the n-region into the p-region while holes are injected from the p-region into the n-region; i.e., minority carrier injection takes place. Subsequently, the

minority carriers diffuse and recombine with majority carriers directly or through trapping at various kinds of recombination centers, producing injection EL. [30]

## 1.4. Chemical Characterization

### 1.4.1. Nuclear magnetic resonance

Nuclear magnetic resonance (NMR) spectroscopy is one of the most powerful techniques available for studying the structure of molecules The NMR phenomenon is dependent upon the magnetic properties of the nucleus. Certain nuclei possess spin angular momentum, which gives rise to different spin states in the presence of a magnetic field. Nuclei with I = 0, where I is the spin quantum number, including all nuclei with both an even atomic number and an even mass number, such as $^{16}O$ and $^{12}C$, do not have a magnetic moment and therefore do not exhibit the NMR phenomenon. In theory, all other nuclei can be observed by NMR.

NMR involves the absorption of radio waves by the nuclei of some combined atoms in a molecule that is located in a magnetic field. Radio waves are low-energy electromagnetic radiation with frequencies on the order of $10^7$ Hz. The quantity of energy involved in RF radiation is very small. It is too small to vibrate, rotate, or electronically excite an atom or a molecule. It is great enough to affect the nuclear spin of atoms in a molecule. As a result, spinning nuclei of some atoms in a molecule in a magnetic field can absorb RF radiation and change the direction of the spinning axis. In principle, each chemically distinct atom in a molecule will have a different absorption frequency or resonance if its nucleus possesses a magnetic moment. The analytical field that uses absorption of RF radiation by such nuclei in magnetic fields to provide information about a sample is NMR spectroscopy. In analytical chemistry, NMR is a technique that enables us to study the shape and structure of molecules. In particular, it reveals the different chemical environments of the NMR-active nuclei present in a molecule, from which we can ascertain the structure of the molecule. NMR provides information on the spatial orientation of atoms in a molecule. If we already know what types of compounds are present, NMR can provide a means of determining how much of each is in the mixture. It is thus a method for both qualitative and quantitative analysis, particularly of organic compounds. In addition, NMR is used to study chemical equilibria, reaction kinetics, motion of molecules, and intermolecular interactions. [31]

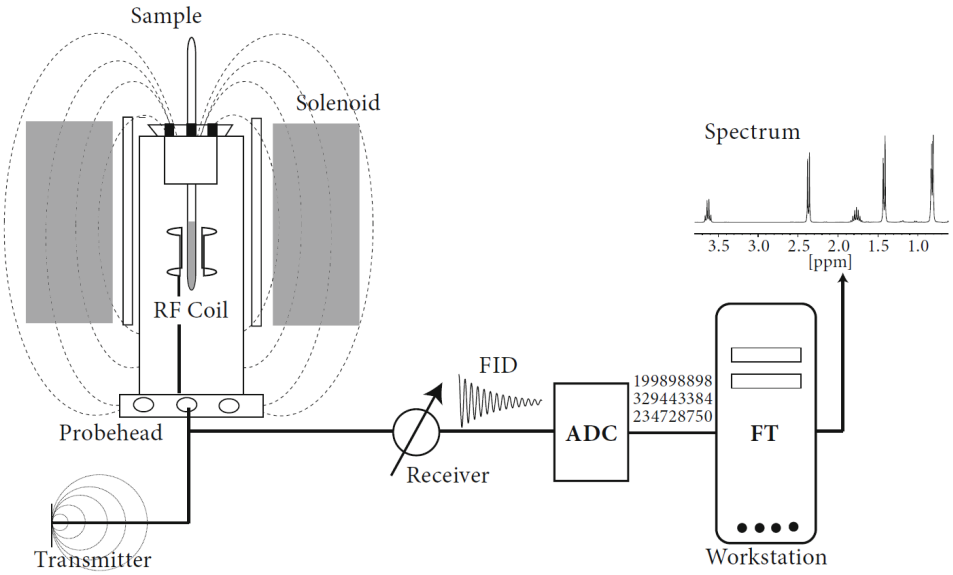


**Figure 1.4.1 Schematic setup of the NMR experiment. ADC – analog-to-digital converter, FID –free induction decay, FT – Fourier transformation reprinted with permission from [32]**

# 2. Literature reviews

## 2.1. Integrated Optical Amplifier-Photodetector on a Wearable Nanocellulose Substrate

### 2.1.1. Flexible Optoelectronics

The use of flexible materials is nowadays one of the main trends in electronics[33] and photonics,[34] and currently shows a broad range of applications,[35] such as deformable displays,[36] chip to chip interconnects,[37] mechanic tuning [38] or sensors.[39]

Moreover, the implementation of a wear-able photonic technology directly in con-tact with clothes would be light-weight, comfortable, noninvasive, implantable, and inherently low cost. It attracts a strong interest for industry in this futuristic field. Indeed, according to International Data Corporation, the important growth of this technology is forecasted to grow up to 213.6 million in 2020.[40] Nowadays, examples of commercial real-time applications include textile-based displays,[41] photovoltaics[41] or health monitoring.[41] In spite of this significant progress, wearable devices still require reduced footprint, better coupling techniques, and the integration of more complex optic/electrical functionalities to meet the performances already provided by traditional semiconductors integrated on rigid substrates.

Taking into account these current limitations, metal halide perovskites (MHPs) is a promising semi-conductor for flexible/wearable optoelectronic devices because of the outstanding capabilities to provide light emission, gain generation, and photodetection functionalities of polycrystalline MHPs films grown at low temperature. Indeed, MHPs demonstrated a broad range of excellent electrical and optical properties, such as long diffusion lengths,[42] high absorption cross-section,[43] high quantum yield of emission at room temperature,[44] or tunable bandgap with the composition.[45] MHP-based devices include highly efficient solar cells,[46] optical active devices,[44, 45, 47, 48] and photodetectors.[49, 50] The majority of these publications, however, use a rigid substrate to fabricate the device, being a significantly lower amount of works on MHP flexible devices with a single functionality as solar cells,[51, 52] optical switch,[53] or lasing.[54]

### 2.1.2. Nanocellulose for wearable optoelectronics

On the other hand, nanocellulose (NC)[55, 56] has been probed as an ideal substrate for wearable optoelectronics.[57] This polymer is obtained from the most common biopolymer on Earth, and it consists of rigid nanocrystals that can be easily assembled into films and gel materials.NC is not only an excellent bendable, deformable and stretchable material,[58] but also exhibits very interesting properties for optoelectronics. Its

advantages comprise a very high transparency in the visible,[59] tunable chiral nematic order by the surface chemistry,[60] low roughness, and extremely high gas barrier properties.[61] Nevertheless, despite these promising abilities, integration of optoelectronic devices in cellulose has been elusive, being it polyimide or polydimethylsiloxane the most common flexible substrates.[62] To the best of our knowledge, there are very few reports of its use in combination with MHP for the preparation of solar cells;[63, 64] with very limited performance but exhibiting a good potential for encapsulation.

### 2.1.3. Integrated optical amplifier–photodetector on Nanocellulose substrate

In the present work, we propose a step forward in the design of wearable optoelectronic devices by the development of an integrated optical amplifier–photodetector on a biocompatible/biodegradable NC substrate, based on polymer/MHP wave-guides (WGs). Our approach to integrate MHP-based opto-electronics/photonics on flexible NC demonstrates: (i) an easy fabrication method to integrate the perovskite and electrodes onto a flexible and biocompatible NC substrates, (ii) a suitable design of the WG structure to enhance the optical gain of the MHP and the generated photocurrent, (iii) the successful integration of the photonic (WG-amplifier) and the optoelectronic (photodetector) components within the same flexible device, and (iv) an in situ monitoring of the photoluminescence signal inside the optical WG-amplifier through the generated carrier photocurrent. This configuration opens a broad range of electronic applications, we stress this point in the present work showing how the system could be an element of the electronic circuitry to regulate the operation depending on temperature.

## 2.2. Operation Mechanism of Perovskite Quantum Dot Solar Cells Probed by Impedance Spectroscopy

### 2.2.1. Halide perovskite solar cells

Halide perovskite solar cells (PSCs) have inspired the photovoltaic community in the past few years because of the high-power conversion efficiency [65-67] already exceeding 23% for solution-processed semiconductors.[46] This value surpasses other thin-film photovoltaic technology efficiencies, such as CdTe or CIGS, and is close to that of crystalline Si cells.[46] However, the record efficiencies reported for hybrid organic−inorganic halide perovskites are in nonstabilized devices, pointing to the most important challenge of halide perovskite technology: stability.[68] Although, hybrid perovskite solar cells show high efficiency, significant challenges remain to prove that a

perovskite photovoltaic product can operate in the field with lifetime greater than 25 years, which is the lifetime of current technologies.[69] One way to palliate these stability issues is the use of fully inorganic halide perovskites, which provide higher stability under thermal stress.[70, 71] $CsPbI_3$ seems to be the most obvious all-inorganic choice to use in perovskite solar cells, as iodine perovskites present a narrower bandgap than bromine and chlorine perovskites,[72, 73] consequently allowing light harvesting for a broader range of wavelengths. Nevertheless, the small size of the $Cs^+$ cation makes the δ yellow orthorhombic phase with broad bandgap, $E_g$, the thermodynamically stable phase for $CsPbI_3$ at room temperature,[74] while the α perovskite phase with $E_g$ = 1.73 eV[75] is the stable phase at high temperature (>320 °C).[76]

The limitation of the perovskite phase stability of $CsPbI_3$ bulk thin films can be overcome by the use of quantum dots (QDs) of the same material that can trap the crystal structure in the typically high-temperature crystal perovskite phase.[76] Colloidal QDs are nanocrystals with smaller dimensions on the order of the Bohr exciton radius, allowing the observation of quantum confinement behaviors such as $E_g$ tuning with particle size.[77] QDs often have enhanced properties compared to the same material composition in bulk form, and thus have been broadly studied in the last few decades.[78, 79] The great success of halide perovskites boosted also the interest in the nanoparticles of these materials. Pérez-Prieto and co-workers reported for first time the development of hybrid halide perovskite nanoparticles,[80] and Kovalenko and co-workers prepared inorganic $CsPbX_3$ (X: $Cl^-$,$Br^-$, and/or $I^-$).[81] In addition to thin-film halide perovskites, nanoparticles are also generating huge interest because relative easy preparation methods yield a simple core structure, without the need for passivating shells, reaching photoluminescence quantum yield (PLQY) values greater than 90%.[82, 83] This remarkable PLQY points to low nonradiative recombination and consequently shows excellent rationale for the development of solar cells. In fact, $CsPbI_3$ QDs have been deposited in a thin film utilized for solar cell fabrication, recently achieving a power conversion efficiency of 13.43%,[84] the world record efficiency for QD solar cells (QDSCs) already outperforming other material systems with very little research. This efficiency was achieved with a post treatment of perovskite QD film using halide salts which provide a method for tuning the coupling between perovskite QDs improving charge transport.[84] Lower performances have been obtained when iodine is totally or partially substituted by bromine.[85] $CsPbI_3$ QDs have been also used in QD sensitized solar cell configuration demonstrating a power conversion of efficiency of 5%.[86] In addition, perovskite QDs also offer the possibility of bandgap tuning using mixed halide perovskites, as $CsPb(Br_{1-x}I_x)_3$, because the reduced

size of these nano-particles avoids the phase segregation,[87] forming bromide- and iodine-rich segregated domains.[88, 89] The phase segregation limits the effectiveness of high-bandgap perovskite materials of special interest for the development of tandem devices.[90] It is also worth mentioning that QDs can exhibit $E_g$ tuning by size confinement, enabling a potential higher-bandgap material without the need for Br.

### 2.2.2. Operating Mechanism of perovskite QD solar cells

Despite this potential, to date there is little knowledge concerning the operating mechanism in perovskite QD solar cell (PQDSC) devices. A priori, the presence of complex QD surface structure[91] with the corresponding ligand molecules and presumed high densities of surface defects should influence transport and recombination and therefore limit the open-circuit potential, $V_{oc}$, to far below that of thin films. However, $V_{oc}$ of up to 90% of the radiative limit has been shown in various compositions of PQD absorber layers,[92] and with hole transport contact optimization, voltages as large as 1.27 V have been reported for absorbers with $E_g$ less than 2 eV.[93]

### 2.2.3. Impedance Spectroscopy Characterization

Here, we prepare PQDSCs with different QD layer thicknesses and characterize them systematically using frequency modulated impedance spectroscopy (IS) to high-light the behavior of this system in terms of working mechanisms and in comparison, with standard PSCs. IS can be applied at the device working conditions, and the frequency modulation allows us to decouple processes with different characteristic times, making this technique ideal to characterize the different processes occurring in the device.[94]

## 2.3. Ligand & Band Gap Engineering: Tailoring the Protocol Synthesis for Achieving High-Quality $CsPbI_3$ Quantum Dots

### 2.3.1. Next generation Optoelectronic Devices

Halide perovskite colloidal quantum dots (QDs), with tunable band gap under quantum confinement regime, are considered very promising materials for the next generation of a broad range of optoelectronic devices, such as high-quality displays,[95] lasers,[45, 96, 97] light-emitting diodes,[98] photodetectors,[99] and solar cells.[100-103] This interest is based on their high photo-luminescence quantum yield (PLQY), bandgap tunability in the entire visible region, and narrow emission line widths.[44, 104-108] Among the different halide perovskite QD materials, $CsPbI_3$ black phase is the inorganic Pb halide perovskite with the lowest bandgap, ~1.80 eV (~1.73 eV in bulk), favorable for both solar cells[101] and light emitting diodes (LEDs).[109, 110] A record in the external quantum efficiency

(EQE) of 21% is achieved for red LEDs based on mixed-anion $CsPbBr_{3-x}I_x$,[111] highlighting the potentiality of these materials. However, it is still a challenge to obtain efficient and stable deep red $CsPbI_3$ LEDs.[112] The main problem is the phase stability of $CsPbI_3$ black phase, which in bulk crystals transforms quickly into non-perovskite yellow δ-phase, presenting a wider band gap to be inactive under photoexcitation.[113] These features reduce the PLQY of the perovskite. Nevertheless, the stability of the CsPbI3 perovskite is significantly increased when this material is synthesized as nanoparticles due to the contribution of the surface energy.[113]

However, $CsPbI_3$ exhibits a blueshift in the band gap com-pared with its bulk counterpart due to quantum confinement, which limits partially its application for the deep red emission or as a light harvester in perovskite QD solar cells.[113] Quantum confinement can be reduced by increasing the QD size for approaching the bulk band gap, without declining the red pure color, by increasing the synthesis temperature.[113] Nonetheless, the formation of bigger $CsPbI_3$ QDs is restricted by some synthetic conditions. Recent reports have highlighted the difficulty of synthesizing $CsPbI_3$ QDs at temperatures higher than 180–185 °C, because the lead halide precursor is not well solubilized.[113, 114] In the case of $CsPbBr_3$ QDs, the precipitation temperature is extended to higher values by increasing the concentration of OA and OLA in the reaction mixture.[114] The synthesis of bigger QDs with narrower band gap and lower full width at half maximum (FWHM) has been achieved, but with a reduced PLQY and stability.[113, 115] In order to overcome these issues, several methods have been mainly considered: (i) incorporation of bromide anions to prepare CsPbBr3−xIx mixed halide perovskites;[70] (ii) metal doping with $Ag^+$,[116] $Bi^{3+}$,[117] $Cd^{2+}$,[118] $Mn^{2+}$,[119, 120] $Sn^{2+}$,[118] $Sr^{2+}$,[121, 122] or $Zn^{2+}$,[118] (iii) purification of $CsPbI_3$ black phase QDs by using polar solvents such as methyl acetate (MeOAc) or ethyl acetate (EtOAc),[84, 113] and (iv) postsynthetic treatment by using water or $ZnI_2$-hexane solutions.[123, 124] These methods can improve different properties such as size dispersion, material stability, PLQY and/or LED performance. Interestingly, the repair of the defective QD surface by using the fourth strategy is critical for boosting mainly PLQY, making that the post-treatment of QDs is well established to enhance the quality of the final product. Unfortunately, the enhancement of the properties of QDs has, in some cases, the collateral cost of the blueshift of the band gap, which remains a big deal. An optimized synthesis of $CsPbI_3$ QDs with suitable optical, structural, and electronic properties is envisioned, as the current synthesis leads to low performances of LEDs. For instance, the use of standard $CsPbI_3$ black phase QDs as an active layer in the standard LED architecture (ITO/PEDOT/p-TPD/perovskite/TPBI/LiF/Al) has provided an external

quantum efficiency (EQE) of around 2.3–2.5%.[122, 125] This performance is lower than those of LEDs based on mixed halide (I/Br) perovskite or doped perovskite, and LEDs with more complex architectures.[111, 121, 126] Hence, it has been difficult to prepare long-term stable deep red $CsPbI_3$ QDs with high PLQY, narrow FWHM and good electrical properties at the same time. By understanding the chemistry behind the QD synthesis, these fascinating features could be unlocked and high-quality materials could be prepared. However, a chemical limitation of perovskite QDs stems from their high surface-to-volume ratio, and in turn from the large number of atoms or ions on the surface that are not coordinated.[127] These surface defects act as traps for photogene-rated excitons, which causes non-radiative recombination and quenches the photophysical features.[115, 127] In this sense, surface passivation of QDs is a key point to minimize the non-radiative recombination. Accordingly, it is expected that the PLQY, the stability of the nanocrystals and the performance of fabricated devices could be improved, with an enhanced passivation.[122, 128]

Herein, we systematically study the impact of the synthesis temperature and capping ligand concentration on the band gap, size distributions, PLQY, PL FWHM, and stability of $CsPbI_3$ black phase (hereafter called only $CsPbI_3$) QDs synthesized by the hot-injection method, and integrated as an active layer in LEDs. We demonstrate that oleylammonium oleate (OLM), produced from the combination between oleic acid (OA) and oleylamine (OLA) ligands, is the determinant species to stabilize the lead precursors during synthesis[129] and promote the surface passivation of QDs. By increasing the OA and OLA concentration in the reaction mixture, we achieved the successful QD synthesis at higher temperatures and efficient passivation of surface defects for higher performance. With these considerations, we produced $CsPbI_3$ QDs with deep red emission, high PLQY, narrow PL FWHM and ultra-high stability for more than 15 months. In this line, the photo-physical properties of our QDs are competitive with previously reported high-quality $CsPbI_3$ QDs.[105, 122-125] We also observed improved red-emissive LED performances, with an EQE = 6% at a similar turn-on voltage to state-of-the-art devices under the same conditions.[122] Moreover, the chromaticity indexes of our devices were beyond the requirement of the Rec. 2020 standards for red color.[130] These findings offer a new insight about how the key synthesis parameters affecting the chemistry involved in the QD formation can be appropriately controlled.

# 3. Experimental

# 3.1. Integrated Optical Amplifier-Photodetector on a Wearable Nanocellulose Substrate

## 3.1.1. Products and Substrate Preparation

All chemicals were used as received. N,N-dimethylformamide (DMF) anhydrous, 99.8%, dimethyl sulfoxide (DMSO) anhydrous ≥99.9%, toluene anhydrous, 99.8%, and poly(methyl methacrylate) (PMMA) with average molecular weight of 350 000 were purchased from Sigma-Aldrich, methylammonium iodide (MAI) was purchased from DYESOL, and $PbI_2$ 99.99%, was purchased from TCI. MHP solutions with concentrations of 1.35 and 2.025 M were prepared by adding 1 mL of DMF and 95 μL of DMSO into each vial containing 622 and 933 mg of $PbI_2$. The solutions were heated at 65 °C to dissolve $PbI_2$. After cooled down to the room temperature, they were poured into corresponding vials containing 215 and 322.5 mg of MAI to make final solutions. PMMA solutions with concentrations of 99, 110 and 140 mg $mL^{-1}$ in Toluene were prepared by stirring.

## 3.1.2. Device Fabrication

Cellulose nanocrystals were obtained via TEMPO-mediated oxidation procedure slightly. The initial aqueous solution was composed by 10 g of Kraft pulp immersed in 1 L of purified water and stirred with a magnetic stirrer for half an hour. Later, the solution was sonicated for other 30 min in a 350-Watt ultrasonic bath, obtaining a preliminary homogeneous suspension of cellulose. Oxidant and catalyst species (0.162 g of TEMPO, 1.000 g of NaBr and 35 mL of NaClO) were added to the solution under stirring. The pH was monitored during the reaction and maintained at a value between 10.5 and 11 through the addition of 1 mL of 1 M NaOH at time. Once stabilized, the pH was neutralized by diluting the solution and letting the cellulose to deposit on the bottom of the bicker and then washed with purified water: the washing was repeated 15 times with at least 400 mL of water each. Cellulose concentration was measured weighting a known quantity of solution, subsequently placed in an oven at 60 °C. Once completely dried, the remaining cellulose was weighted again. Typical values were in the range 3–5 mg $mL^{-1}$. The concentration can be tuned by either dilution or concentration through water evaporation. The mechanical disintegration to release the nanofibers was reached through sonication using a Bandelin Sonopuls HD 2200 ultrasonic homogenizer with a 13 mm diameter ultrasonic tip for 2 min at 20 kHz frequency and 100 W output power. This step was repeated twice for every sample, obtaining transparent NC fibrils suspension. Finally, the films were obtained by pouring the clear suspension on a 8.5 cm diameter Petri dish and drying it at 60 °C in an oven. The oven was equipped with a flat copper foil to maintain

homogeneous temperature over the whole layer surface. The solution dried for 36 h, at the end a transparent and homogeneous film could be peeled off. These were stored at room temperature in a dehumidified container. To be handled NC films need to have 10–20 μm of thickness. This can be obtained by varying either the amounts of the poured solution or by changing the NC concentration.

Samples used for the perovskite deposition were 20 μm thick (see section A.1 for more details). Then, NC was attached to glass substrates by using double sided tape at margins. In order to have a uniform and homogeneous layer of perovskite on plain glass and NC, substrates were ozone treated for 15 min just before spin coating of perovskite. MHP films were deposited by spin-coating of 50 μL of 1.35 and 2.025 M solutions for 50 s at 4000 and 3000 rpm, respectively. During spin coating, anti-solvent method was employed in order to help in the film crystallization, washing with nonpolar diethyl ether just before formation of white crystals in the substrate. At 30 and 60% RH, this could be relatively 8–9 and 12–13 s after starting the spin coating. Then substrates were annealed at 100 °C for 3 min. At the end of the process 350–500 nm thick $MAPbI_3$ films (thickness is controlled with the spin coating speed) were deposited on the NC.

Once the perovskite was properly deposited on the flexible substrate, 1 $mm^2$ square and 30 nm thick Au electrodes were evaporated on the semiconductor. Then, gaps of 100, 500, and 1 μm were patterned by protecting the sample with an aluminum mask. Finally, a ≈1 μm thick PMMA film is spin coated for 3000 rpm on the perovskite as capping layer and post baked at 80 and 150 °C each temperature. Here evaporated gold electrodes defining the photoconductive detector were protected with a resist before PMMA deposition, in order to enable the final bonding of silver wires with silver paint. The biocompatibility and flexibility of the cellulose substrate allows the-device-on-cellulose to be easily wore on or incorporated to any kind of substrate or surfaces. Here it was deposited on a polyimide strip (one side glued) to allow an easier examination of the optical electrical properties. For this purpose, edges of the sample were carefully cut with a thin blade from the back side (polymer strip).

For electrical measurements, the whole device-on-cellulose/polymer stripe structure was pasted on glass in order to allow an easier bonding of Au wires and the electrical connections.

### 3.1.3. Characterization

The morphology of the films was analyzed by SEM using a JSM7001F (field emission scanning electron microscope). The XRD patterns of the samples were measured using a X-ray diffractometer (D8 Advance, Bruker-AXS) (Cu $K_\alpha$, wavelength $\lambda = 1.5406$ Å).

The device was examined at room temperature and ambient conditions by end-fire coupling a Nd:Yag laser doubled at 532 nm (SNP-20F-100 supplied by Team Photonics, France) at the input edge of the sample (pulse of 1 ns 20 KHz repetition rate) with the aid of 40× microscope objective (Figure 4.1.1). The waveguide PL of the $MAPbI_3$ at 780 nm (Figure 4.1.1a) was collected at the output edge of the structure with a 20× microscope objective and focused into a fiber optic connected to a HR4000 Ocean Optics spectrograph (estimated overall resolution better than 0.7 nm).

Time resolved PL was carried out by focusing the PL into a Hamamatsu C5658-3769 avalanche photodetector connected to a BOXCARDPCS-150 electronics from Becker & Hickl GmbH.

Photocurrent (see Figure 4.1.1a) is analyzed by applying an electric field between the Au electrodes and measuring the generated current by using a Keithley's Series 2400 Source MeterUnit (SMU). Detection below 1nA is limited in some cases by the dark current of the photoconductor and resolution of the multimeter.

Frequency dependence experiments were carried out by illuminating the samples under continuous wave (CW) excitation at 532 nm (Z40M18-B, Z-laser Optoelektronic GmbH, Germany) chopped at a controlled frequency. Then photocurrent generated by the application of the external voltage with the SMU is synchronously detected with a lock-in amplifier (SR810, StandFord Research Systems) by previously filtering the DC component with a RC circuit. Time dependence electrical experiments were performed by detecting the photocurrent with the scope GDS-8208 (GW Instek, Taiwan). Additional characterization was performed by focusing the excitation beam on the top of the sample and measuring the back-scattering PL/photocurrent with the same set-up. In addition, samples were also examined under CW excitation at 532 nm, and 1 ns pulsed Nd:Yag laser doubled at 532 nm with variable repetition rate 100–1 KHz (FTSS355-Q4-1KHZ adapted at 532 nm and supplied by CryLas Laser Systems, Germany). Temperature measurements were done by using a Peltier device with area 1 $cm^2$.

## 3.2. Operation Mechanism of Perovskite Quantum Dot Solar Cells Probed by Impedance Spectroscopy

### 3.2.1. Materials

Cesium carbonate ($Cs_2CO_3$; 99.9 %, Sigma-Aldrich), $PbI_2$ (99.999 %, ABCR), oleic acid (OA; 90 %, Sigma-Aldrich), oleylamine (OAM; ≥ 98 %, Sigma-Aldrich), 1-octadecene (ODE; 90 %, Sigma-Aldrich), hexane (≥ 95 %, Sigma-Aldrich), octane (≥ 99 %, Sigma-Aldrich), Methyl acetate(MeOAc anhydrous, 99.5 %, Sigma-Aldrich), Eethyl acetate (EtOAc anhydrous, 99.8 %,Sigma-Aldrich), $Pb(NO_3)_2$ (99.999 %, Sigma-Aldrich), $N^2,N^2,N^{2'},N^{2'},N^7,N^7,N^{7'},N^{7'}$-octakis(4-methoxyphenyl)-9,9′-spirobi[9H-fluorene]-2,2′,7,7′-tetramine (spiro-OMeTAD, ≥ 99 %, Merck), cholorobenzene (anhydrous, 99.8 %, Sigma-Aldrich), 4-tert-butylpridine (4-TBP; 96 %, Sigma-Aldrich), bis (trifluoromethane)-sulfonimide lithium salt (99.95 %, Sigma-Aldrich), acetonitrile (anhydrous, 99.8 %, Sigma-Aldrich), and commercial Ti-alkoxide solution (ShareChem, SC-BT060). FTO glasses (25x25 mm, Pilkington TEC15, ~15$\Omega\square^{-1}$). All materials were used as received.

### 3.2.2. CsPbI3 QDs synthesis and purification

$CsPbI_3$ QDs were synthesized following the report by Luther and coworkers. [84] Cs-oleate in ODE solution was synthesized with 0.814 g of $Cs_2CO_3$, 2.5 ml of oleic acid, and 40 ml of ODE in 100-ml three-neck flask under vacuum at 120 ˚C for 1 hr. under stirring. After purging the nitrogen in the flask, the flask was heated to 150 ˚C until the reaction was completed shown clear solution. The Cs-oleate in ODE solution was cooled and used for QD synthesis. In order to synthesize $CsPbI_3$ QDs, 0.5 g of $PbI_2$ and 25 ml of ODE were degassed in the 100 ml three neck flask under vacuum at 120 ˚C for 30 min under stirring. OA and OAM (2.5 ml of each) were added to the reaction flask and put flask under vacuum for 1 minute until the $PbI_2$ had completely dissolved. Then, $PbI_2$ solution was purged with $N_2$ and then heated to 170 ˚C quickly. Once the reaction temperature was reached, 2 ml of preheated Cs-Oleate in ODE (100˚C) was injected into the reaction flask. The reaction was quenched by immediate immersion of the flask into an ice-water bath (5 sec after injection). To purify QDs, 70 ml of MeOAc or EtOAc was added to as-synthesized QD solution and then centrifuged at 4700 rpm for 5 min. The supernatant was discarded, and the QDs was dispersed again in 5 ml of hexane. 8 ml of MeOAc or EtOAc was added again to QDs solution and then immediately centrifuged at 4700 rpm for 5 min. the precipitate was dispersed in 10 ml of hexane. QDs solution was kept to dark at 4 ˚C.

Before use, the solution was centrifuged 4700 rpm for 5 min, the precipitate was removed and the QDs was dried with nitrogen and dissolved in octane at concentration of ~50 and 75 mg/ml.

### 3.2.3. Device fabrication

A ~30 nm compact $TiO_2$ layer was deposited via solution onto FTO. 80 µL of Ti-alkoxide solution was deposited with spin coating at 4000 rpm for 30 seconds, the spin-cast films were dried at 150 ˚C for 10 min and then annealed at 500 ˚C for 30 min. $CsPbI_3$ QDs film were fabricated according to previous report.[84] In short, saturated $Pb(NO_3)_2$ in MeOAc or EtOAc was prepared by sonicating 40 mg of $Pb(NO_3)_2$ in 40 ml of MeOAc or EtOAc for 10 min and then for removing the excess salt it was centrifuged at 4000 rpm for 5 min. Each layer of $CsPbI_3$ QDs was spin coated from QDs solution in octane (50 mg/ml and 75 mg/ml) at spin speed of 1000 rpm for 20 s and 2000 rpm for 5 s. Then, the film was dipped 3 times into $Pb(NO_3)_2$ in MeOAc or EtOAc solution, rinsed in neat MeOAc or EtOAc , and then immediately dried with nitrogen. Devices were prepared with different layer 1-5 of 50 mg/ml and 1-7 of 75 mg/ml solution. The spiro-OMeTAD hole transporting material was spin coating at 4000 rmp for 30 sec from a solution of 72.3 mg of spiro-OMeTAD, 1 ml chlorobenzene, 28.8 µL of 4-TBP, and 17.5 µL of Li-TFSI solution (520 mg/ml in acetonitrile). Au was evaporated at rate ranging from 0.5-1 A/s for a total thickness of 70 nm.

### 3.2.4. Characterizations

The current- voltage were measured through Abet Technologies Sun 2000 Class A solar simulator with a Keithley 2612 Source Meter with scan rate of 10 mV/s under AM 1G. The active area of the device was defined based on a mask area of 0.11 $cm^2$. The light intensity was matched one sun by calibrating with a Si reference cell equipped with a IR-cut off filter.

IPCE measurement was measured with employing 150 W xenon lamp coupled with a monochromator. The external quantum efficiency was measured using an optical power meter 70310 from Oriel instruments, using Si photodiode to calibrate the system.

FE-SEM (JSM7001F) was utilized to carry out thickness of film.

The structural of the $CsPbI_3$ QDs was determined by using X-ray diffractometer (Bruker AXS, D4 Endeavor advanced X-ray diffractometer, with Cu $K_\alpha$ radiation).

Absorbance was done using Varian Cary 300 Bio spectrophotometer.

PLQY was measured using a Hamamatsu integrating sphere where a quartz cuvette containing the sample was placed. PLQY is referred to QDs which were purified two times with methyl acetate were dispersed in hexane. For PLQY measurement, we the absorbance of QDs solution was kept between 0.5-0.6. As reference, measurement was performed with cuvette containing only the hexane in the same excitation wavelength. PLQY of $CsPbI_3$ QDs solution with absorbance of 0.553 at excitation wavelength of 400 nm is 40%. PL was measured by Horiba FL-100.

The impedance spectroscopy measurements were carried out in a PGSTAT- 30 potentiostat from Autolab. A Xe lamp was used to illuminate the PSC controlling the light intensity with neutral density filters, between 0.1 and 100 $mW/cm^2$ in a logarithmic scale. The AC voltage perturbation was fixed at 20 mV under open-circuit conditions. The integration time was fixed at 0.125 s and the number of cycles was equal to 1. Each frequency spectrum was measured ranging between 1 MHz and 0.1 Hz. The equivalent circuit we have used to fit the data is plotted in Figure A.2.6. Further details on Impedance characterization method can be found in reference [131].

## 3.3. Ligand & Band Gap Engineering: Tailoring the Protocol Synthesis for Achieving High-Quality $CsPbI_3$ Quantum Dots

### 3.3.1. Materials and chemicals

All chemicals used for the synthesis were purchased from Sigma-Aldrich, unless otherwise specified. Cesium carbonate ($Cs_2CO_3$, 99.9 %), lead (II) iodide, ($PbI_2$, 99.99 %, TCI), 1-octadecene, (1-ODE, 90 %), oleic acid (OA, 90 %), oleylamine (OLA, ≥ 98 % primary amine), methyl acetate (MeOAc, anhydrous, 99.5 %), hexane (anhydrous, ≥99 %, mixture of isomers), hexane (≥ 97.0 %, CHROMASOLV for HPLC (GC) Honeywell), n-octane (anhydrous, ≥ 99 %), $CDCl_3$ (100%, 99.96 atom %D, contains 0.03% (v/v) TMS), PEDOT:PSS Clevios (P VP Al 4083), poly(N,N'-bis-4-butylphenyl-N,N'-bisphenyl)benzidine (Poly-TPD, Ossila), TPBi (2,2′,2"-(1,3,5-Benzinetriyl)-tris(1-phenyl-1-H-benzimidazole)) , lithium fluoride (99.99 %), aluminum pellets (Evaporation Materials Kurt J. Lesker) and ITO glasses (25 x 25 $mm^2$, Pilkington TEC10 ~10 $\Omega m^{-1}$).

### 3.3.2. Synthesis and isolation of colloidal $CsPbI_3$ Perovskite Quantum Dots (QDs)

$CsPbI_3$ QDs were synthesized following the previous reports with some modifications.[84, 100, 113] First, Cs-oleate solution was prepared by mixing 0.814 g of $Cs_2CO_3$, 2.5mL of OA and 40 mL of 1-ODE into a 100 mL-three neck flask and heating at 120 °C under

vacuum for 1 h until bubbling completely disapplied. Then the mixture was heated until 150 °C under $N_2$-purge in order to complete the formation of Cs-Oleate. Since the Cs-oleate become solid, before injection, the solution was heated to 100 °C under $N_2$ flow. In a 100 mL-three neck flask, $PbI_2$ (0.5 g) and dried 1-ODE (25 mL) were stirred and degassed under vacuum at 120 °C for 1 h. The flask was then purged with $N_2$ and kept under constant stirring. 1.5 mL to 4 mL of dried OA and OLA (depending to temperature of synthesis) were injected. The flask was put under vacuum again until the $PbI_2$ completely dissolved and the solution was no longer releasing gas (15 – 30 min). The synthesis temperature influences the QD size (170 °C for 9.14 nm, 180 °C for 10.60 nm, 185 °C for 12.84 nm, and 190 °C for 13.16 nm, QDs). 2 mL of pre-heated Cs-oleate solution was swiftly injected into the reaction mixture under $N_2$ atmosphere. After 5 s, the reaction was quenched by immediate immersion of the flask into an ice bath.

As-prepared $CsPbI_3$ QDs were precipitated by adding MeOAc (7.5 mL QDs crude solution: 17.5 mL MeOAc) and then centrifuged at 7500 RPM for 5 min. The QDs were dispersed in 7.5 mL of hexane and stored in the dark at 4 °C for at least 24 hours to precipitate excess Pb-oleate. The QDs solution was decanted and centrifuged again at 4000 RPM for 5 min before use. For device fabrication, hexane was dried, and the QDs were dissolved in n-octane at a concentration of ~20 mg/mL.

### 3.3.3. Characterization of CsPbI3 QDs

The crystalline structure of the $CsPbI_3$ QDs was determined by using an X-ray diffractometer (Bruker AXS, D4 Endeavor advanced X-ray diffractometer, with Cu $K_\alpha$ radiation).

Absorption spectra was performed on a Varian Cary 300 Bio spectrophotometer.

Steady-state photoluminescence (PL) and photoluminescence quantum yield (PLQY) was measured using a Hamamatsu integrating sphere at excitation wavelength of 400 nm. PLQY is referred to QDs which were purified one time with methyl acetate and further dispersed in hexane. As reference, measurement was performed with cuvette containing only the HPLC-hexane in the same excitation wavelength. To avoid the influence of different concentrations of $CsPbI_3$ QD solutions on the PLQY measurements, we adjusted the concentrations to be an appropriate level, which is that the QDs solution was diluted in HPLC n-hexane until the measurement was 0.67 of absorbance at the wavelength of 400 nm.

Time-resolved photoluminescence (TRPL) was measured through photoluminescence spectrophotometer (Fluorolog 3-11, Horiba). 405 nm pulsed laser (1 MHz frequency, NanoLED-405L, <100 ps of pulse width) was used to excite QDs. All measurements for the TRPL were performed under inert environment with $N_2$ purged solution to prevent extra excitation quenching.

High-resolution transmission electron microscopy (HRTEM) images of perovskite nanoparticles were obtained with a field emission gun TECNAI G2 F20 microscope operated at 200 kV.

The size distribution and particle size of QDs were obtained from the TEM images with ImageJ software.

Nuclear magnetic resonance (NMR) characterization was carried out by using Bruker Avance III HD 400 MHz instrument, using $CDCl_3$ as solvent.

### 3.3.4. Fabrication of the CsPbI3-based LED devices

In order to have the active area of 6 $mm^2$, 2.5 x 2.5 $cm^2$ ITO substrates (10 $\Omega/cm^2$) were partially covered with scotch tape and then extra part of scotch tape was cut with laser printer (model LaserPro C180) at speed and power of 8 and 50% respectively) and left 12 mm width without tape. Then, the substrates were etched with Zinc powder and 6 M HCl (37% HCl was diluted with equal volume) one by one and wiped with tissue paper, rinsed with DI water. Later on, scotch tape was removed and any remaining glue from tape were cleaned with paper and ethanol, and then substrates were introduced in a soap solution and sonicated for 15 min. The substrates were rinsed couple of times with DI water and sonicated again with ethanol for another 15 min. After that, ITO substrates were introduced into a mixture of isopropanol/acetone (1:1 v/v), sonicated for another 15 min and dried with compressed air or nitrogen. After that, the substrates were introduced into a UV–$O_3$ cleaner for 15 min and the solution of PEDOT: PSS was spin coated at 3000 rpm for 30 s and annealed at 140 °C for 10 min in air, to yield a thin layer (20 nm). Next, a Poly-TPD layer was spin coated (20 mg/mL in chlorobenzene) at different rpms (e.g. 4000 rpm) for 30 s, and subsequently annealed at 140 °C for 10 min in air. The solutions of QDs (20 mg/mL) in n-octane were spin-coated at 3000 rpm for 30 s. After that, 60 nm of TPBi, 1nm of LiF and 100 nm Al were thermally evaporated at rates of 0.02-0.03, 0.5 and 1.5–2 Å/s, respectively; the active areas were encapsulated with adhesive tape and then contacts covered with Cooper tape for the measurement.

# 4. Results and Discussions

## 4.1. Integrated Optical Amplifier-Photodetector on a Wearable Nanocellulose Substrate

The integrated WG amplifier–photodetector proposed in this work allows simultaneously the amplification of emitted light by the MHP and the signal monitoring by the photocurrent detected at metal contacts separated by the WG, as illustrated in Figure 4.1.1a.

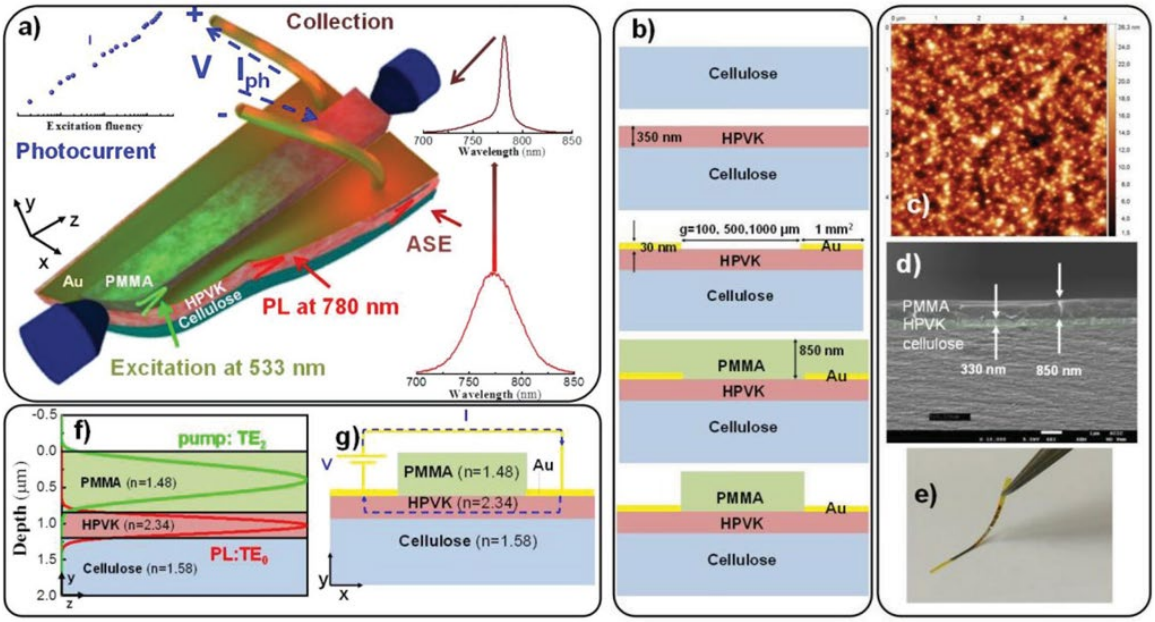


**Figure 4.1.1 Description of integrated optical amplifier–photodetector. a) Scheme of the optical waveguide amplifier and photodetector integrated on NC. b) Fabrication procedure. c) AFM image of the MHP surface on NC. d) SEM cross section of the device. e) Photograph of the device on NC held on a polymer strip (without electrical contacts). f) Longitudinal cross section of the WG and mode analysis. The low optical losses in the polymer allow the propagation of the excitation beam at 532 nm (TE2) along the whole length of the WG (green curve), whereas the PL of the MHP at 780 nm (see red curve in (a)) is excited along the WG by the evanescent field of the mode at 532 nm, and it is coupled to the TE0 mode confined in the semiconductor (red curve); under high enough excitation fluency the WG demonstrates ASE (see brown curve in (a)). g) Transversal cross section of the device with detail of the photodetector, which measures a photocurrent proportional to the applied bias voltage upon laser excitation beam propagation (blue symbols in (a)).**

Essentially, we exploited the optical confinement at the WG, due to the refractive index contrast between the MHP core (2.24 at 780 nm),[44] the NC bottom cladding (1.54 at 780 nm)[60] and the poly(methyl methacrylate) (PMMA) top cladding (1.492 at 780 nm). The WG is optimized to propagate both the excitation beam at 532 nm end fire coupled at the input edge of the sample (represented by a green Gaussian profile) as well as the generated photoluminescence (PL) at 780 nm (red PL spectrum at the bottom right corner of Figure

5.1.1a) that will propagate along the WG structure. In these conditions, light decoupled at the WG output is characterized by amplification of stimulated emission (brown spectrum at the top right corner of Figure 5.1.1a), and the application of a bias voltage between the electrodes promotes the establishment of a photocurrent (blue data symbols at the top left corner of Figure 4.1.1a) proportional to the excitation fluency along the WG. Fabrication procedure is illustrated in Figure 4.1.1b and thoroughly reported in methods section and in Section A.1.1). NC was obtained by a modified version of the protocol presented in ref. [132]. Then, a compact layer (see Figure A.1.1) of $CH_3NH_3PbI_3$ ($MAPbI_3$) perovskite (see X-ray diffractometer (XRD) Figure A.1.2) was deposited on top of NC, and then capped by a PMMA film after patterning Au electrodes on the surface of the semiconductor. All films showed low roughness (see Figure 4.1.1c and Figure A.1.3) and good homogeneity (see Figure 4.1.1d). Since this compact device is implemented in a flexible NC substrate, it allows bending and wearable properties (see Figure 4.1.1e).

Mode analysis carried out on a PMMA/MHP bilayer structure of 0.85/0.35 μm reveals that the pump beam at 532 nm supports the first three propagation modes in each polarization (see Section A.1.2). These modes are spatially distributed along the semiconductor (TE0 and TE1) and the polymer (TE2) with negligible difference between the transverse electric (TE) and magnetic (TM) polarizations, thus the discussion about TE can be extended to TM modes. Propagation at 532 nm along the TE0 and TE1 modes, however, is inhibited by the high absorption coefficient of the MHP at this wavelength (about 13 $\mu m^{-1}$);[43, 44] and hence pump beam at 532 nm mainly travels along the TE2 mode (see Figure 4.1.1f) whose losses are reduced down to 0.05 $\mu m^{-1}$. In these conditions, evanescent field of TE2 in the MHP (0.3% overlap) generate PL at 780 nm along the entire length (≈1 mm) of the WG. On the opposite, the TE0 and TE1 modes supporting the propagation of PL peaked at 780 nm are highly confined (70% overlap) in the MHP, see Figure 4.1.1e, and will promote amplification of the spontaneous emission (ASE) for high enough laser excitation fluencies. Indeed, we already demonstrated that the PMMA layer on top of MHP (in this case deposited on a rigid substrate) produced a double beneficial effect that assured low ASE threshold:[48] (i) PMMA encapsulates the perovskite making the device stable over several months,[48] and (ii) The low losses of the mode at 532 nm confined in the PMMA allows a nearly uniform excitation of the MHP layer in the WG structure. For comparison purposes a less demanding rigid system PMMA/MHP integrated in silicon substrates has been also produced and characterized. In this configuration, a pump fluency of about 100 nJ $cm^{-2}$ corresponds to ≈ $2 \times 10^{20}$ photons $cm^{-2}$, which gives rise to ≈ $3.5 \times 10^{18}$ electrons per pulse cm3 from valence to conduction band (≈ $E.\alpha/h\vartheta$, where E is the pump fluency,

$\alpha$ the absorption coefficient and $h\vartheta$ the energy of the incident photon). Assuming the aforementioned uniform excitation and the geometrical parameters of the excited MHP film (100 μm wide, 0.5 μm thick, 1 mm length)$1.7 \times 10^{11}$ electron–hole pairs/pulse will be generated in the whole waveguide at the ASE threshold. Since the passivation of grain boundaries in MHP film[48, 133] lead to an enhancement of the emission quantum yield up to 70%,[134, 135] most of these pairs potentially will recombine radiatively increasing the PL signal.

Simultaneously, the application of an electric field when the MHP is optically pumped will promote a portion of those photogenerated carriers toward the external electrical circuit, i.e., give rise to an electrical photocurrent (transversal cross section in Figure 4.1.1g). The photoresponse of the photoconductive detector under illumination is analyzed simultaneously with the PL/amplification experiment for different applied bias, where the electric field can be also tuned by using different gap distance between electrodes (see Figure 4.1.1f). As a result, the device demonstrates photocurrents of 10–100 nA (varying slightly for different fabricated devices and electrode gap distance) under low bias voltages (5–10 V) at the ASE threshold energy inside the WG, which is observed at ≈ 4 nJ with a line width of ≈5 nm. Indeed, we demonstrate very close performance of the sub-system fabricated on NC standing over both rigid and flexible holders/supports. Therefore, our approach paves the road of a future technology for wearable devices that could be directly printed on paper or incorporated in clothes or other curved sur-faces by using NC as intermediate substrate.

MHP films deposited on NC were firstly examined under surface illumination in order to establish their optical and electro-optical properties as compared to the same films deposited on rigid substrates.

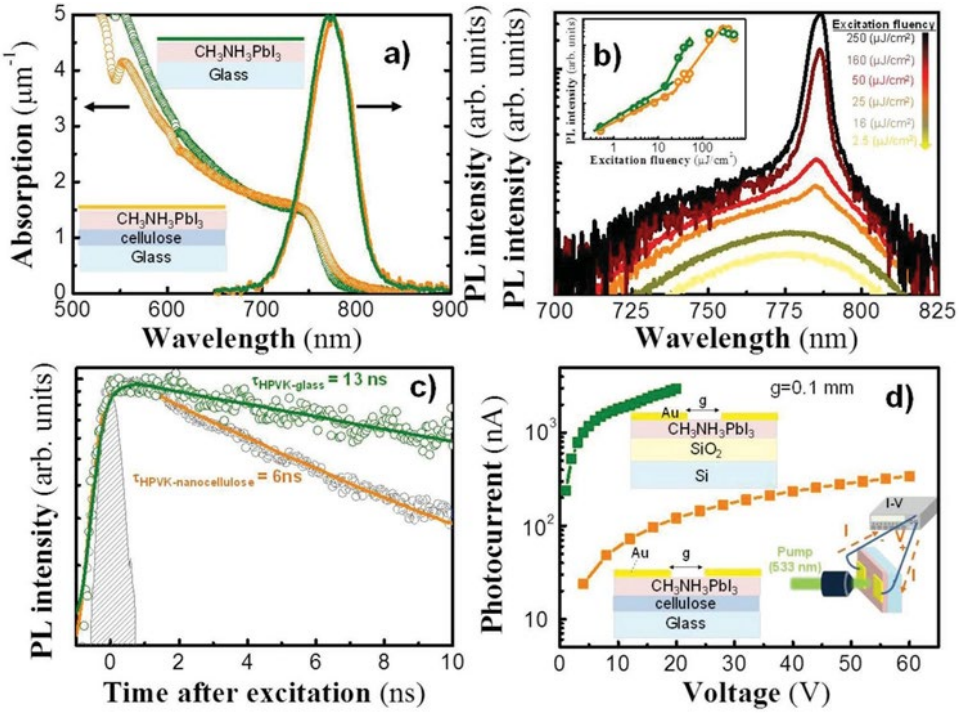


**Figure 4.1.2 Light absorption, photoluminescence and photocurrent characterization of films and integrated devices. a) Absorption (symbols and left axis) and PL intensity (solid lines and right axis) of a 350 nm thick MHP layers spin coated on glass (green) and NC (orange) (held on glass). b) PL spectra of MHP deposited on NC measured under back-scattering geometry (laser focused on the surface of the samples) for different excitation fluencies; above a threshold of ≈15 μJ cm$^{-2}$ the PL spectra narrows and its intensity grows superlinearly, clear signatures of stimulated emission; the inset compares the PL intensity as a function of the excitation fluency for MHP deposited on NC (orange symbols) and MHP deposited on glass (green symbols). Note the logarithmic scale on Y-axis. c) Time resolved photoluminescence spectra of the MHP layer deposited on glass (green) and NC (orange) measured under a low excitation fluency of 30 nJ cm$^{-2}$; symbols and solid lines refer to experimental data and fitting, respectively; gray shaded area corresponds to the system response. d) Photocurrent as a function of the applied voltage (inset corresponds to the experimental setup) under a CW excitation at 532 nm in a 350 nm thick MHP layer spin coated on a SiO2/Si substrate (green symbols) and on NC (orange symbols) in a photoconductor device with a gap distance between electrodes g = 0.1 mm.**

The absorption coefficient of the films as a function of wavelength (left axis of Figure 4.1.2a) presents a sharp band edge beginning at around 770 nm (1.61 eV), a visible exciton resonance at 750 nm (1.65 eV) and a monotonous increase below the bandgap wavelength, in agreement with previous publications.[43, 44] Indeed, the NC substrate did not introduce any significant spectral changes as compared to the film deposited on glass (see Figure 4.1.2a). Similarly, PL under low fluencies shows similar spectrum for both films deposited either on glass or on NC (see Figure 4.1.2a). In both cases the MHP film exhibits ASE for

high enough excitation fluencies (1 ns pulsed laser at 532 nm with 1 KHz of repetition rate) (see Figure 4.1.2b): [44, 47] The Gaussian-shaped PL band centered at ≈780 nm with a full width at half maximum (FWHM)≈ 55 nm becomes an intense and narrow Lorentzian ASE line with FWHM <10 nm (Figure 4.1.2b) centered at 785 nm. The slight redshift in the ASE peak as compared to the maximum of PL is usually found in ASE devices,[43, 44] which is due to the reabsorption effect of photons produced at the high energy tail of the PL.

It is important to highlight that ASE threshold, $\approx 10\ \mu J cm^{-2}$ shown in Figure 4.1.2b, is very similar in MHP films deposited on both glass and NC substrates, as observed in the inset of Figure 4.1.2b; this value is in agreement with other studies.[136, 137] This result confirms the good optical quality deduced from absorption/PL measurements in both cases. The observed slight increase of the ASE threshold in NC samples can be initially attributed to a higher contribution of nonradiative channels, which can be related to the smaller grain size of MHP on NC measured by atomic force microscope (AFM). According to the kinetics study shown in Figure 4.1.2c, the experimental decay time of the PL measured on these MHP films under low excitation fluencies (below ASE threshold) is slower when deposited in glass than in NC substrates. Indeed, the data were fitted by an effective decay time, $\tau_{eff}$, of 13 and 6 ns for glass and NC, respectively. The exciton radiative lifetime in our MHP films results to be $\tau_r = 18.6\ ns$, as estimated from the relation:

$$\frac{1}{\tau_{eff}} = \frac{1}{\tau_r} + \frac{1}{\tau_{nr}} \qquad \textbf{4.1.1}$$

where $\tau_{nr}$ is the nonradiative recombination time, and the quantum yield:

$$\boldsymbol{QY} = \frac{\tau_{nr}}{\tau_{nr}+\tau_r} \qquad \textbf{4.1.2}$$

of ≈70% for MHP films reported elsewhere.[135, 136] By taking into account that $\tau_r$ should be the same in both substrates, the nonradiative recombination time for MHP deposited on NC is $\tau_{nr}$(NC) = 8.9 ns (whereas $\tau_{nr}$(glass) = 43 ns), which would give a drop in the QY up to 32%. It is difficult to give a precise microscopic origin of the increased influence of nonradiative channels (smaller nonradiative times in perovskite on nanocellulose as compared to that on silicon/$SiO_2$), but possibly is related to an increased density of point/linear crystalline defects in the case of nanocellulose promoted by its surface peculiarities and subsequent perovskite crystallization as compared to $SiO_2$.

In addition, the lower thermal conductivity of NC (0.22– 0.53 $Wm^{-1}\ K^{-1}$)[138] as compared to glass (≈1 $Wm^{-1}\ K^{-1}$) can also influence the ASE threshold difference. Indeed,

the ASE spectra registered in the case of MHP on NC (Figure 4.1.2b) where unstable after some minutes, as compared to the films deposited on glass that demonstrated good stability under the same laser excitation conditions. On the opposite, a stable ASE operation in MHP was observed when the repetition rate was reduced down to 100 Hz, probably because a duty cycle of 10 ms between ns-pulses allows a sufficient cooling recovery (see Section A.1.3).

**Table 4.1.1 Electrical and electro-optical properties of MHP films (350 and 500 nm thick) prepared under ambient conditions on NC and SiO2/Si substrates. Responsivity measured through electrodes separated 0.1 and 1 mm are compared at bias voltages 2 and 20 V given its linear dependence with electric field.**

| | | MHP on nanocellulose | | MHP on $SiO_2$/Si | |
|---|---|---|---|---|---|
| | | 350 nm | 500 nm | 350 nm | 500 nm |
| Resistivity [$10^4$ Ω cm] | | 1.2–12 | 0.3–1.9 | 2–35 | 5–20 |
| Responsivity [mA $W^{-1}$] | $g$ = 0.1 mm (2 V) | 0.067 | 0.072 | 1.730 | 0.110 |
| | $g$ = 1 mm (20 V) | 0.020 | 0.085 | 0.640 | 0.390 |

Several sample series were processed under ambient conditions to measure wave-guided PL signal and photocurrent to check for reproducibility. Both dark current and photocurrent were measured through the deposited two metal contacts defining the photoconductor, and they yield different values of resistivity and responsivity from sample to sample, as indicated in Table 4.1.1. From I–V curves under dark conditions (see Section A.1.4), the resistivity measured in most of the films are within the range $3 \times 10^3$–$3.5 \times 10^5$ Ω cm, being found the larger dispersion in the case of the thinnest samples, likely due to the greater thickness inhomogeneity and surface roughness (in the case of NC). The smallest values, ≈ 3–5 × 103 Ω cm, are measured in 500 nm thick films deposited on NC, similar to values previously reported.[139, 140] In other samples, where the MHP was deposited either on NC or $SiO_2$/silicon, the resistivities were as high as 105 Ω cm. In these cases, assuming a mobility of ≈10 $cm^2$ $V^{-1}$ $s^{-1}$ as proposed elsewhere,[141] the electron concentration would be as low as $10^{13}$ $cm^{-3}$, which can be related to a near intrinsic semiconductor behavior.[142] In samples exhibiting this more intrinsic behavior the dark current will be smaller, hence being more sensitive to low light levels for which higher responsivity would be possible to measure.[143] In this way, a certain minimum concentration of photogenerated carriers are needed to overcome the background electron concentration in thermal equilibrium in order to give an appreciable photocurrent density $J_{ph}$:

$$J_{illumination} = J_{dark} + J_{ph} = e\mu_n n_0 + e\mu_n \Delta n \quad \textbf{4.1.3}$$

assuming a n-type character for the MHP,[49, 50] consistently with better responsivity values measured in more resistive films (Table 4.1.1).

In MHP films under low illumination level (60 mW $cm^{-2}$ at 532 nm under normal incidence, see inset in Figure 2d) exhibit a noticeable photocurrent of ≈2 × $10^3$ and ≈$10^2$ nA (at 15 V of bias voltage, i.e., low applied electric field ≈1.5 kV $cm^{-1}$) in $SiO_2$/Si and NC substrates, respectively, as observed Figure 4.1.2d. The lower photocurrent of the films deposited on NC is again attributed to nonradiative carrier losses, but also to the smaller resistivity (higher dark current in this NC sample) and the worse thermal conductivity of NC.

The temporal response of the device seems to be limited by the RC constant of the photoconductive detector circuit (R = 1 MΩ, C = 330 pF), because it is observed a frequency band-width below 1 kHz, and the RC constant of the photoconductive device itself that gives a time constant of around 20 μs due to the high resistivity of the MHP film, see Figure A.1.8, at least for the excitation laser used in the experiments with 20 kHz of repetition rate. In any case, this is not a limitation factor for the concept device demonstrated in this work and future improvements are possible by optimizing both factors (photodevice and its external circuit).

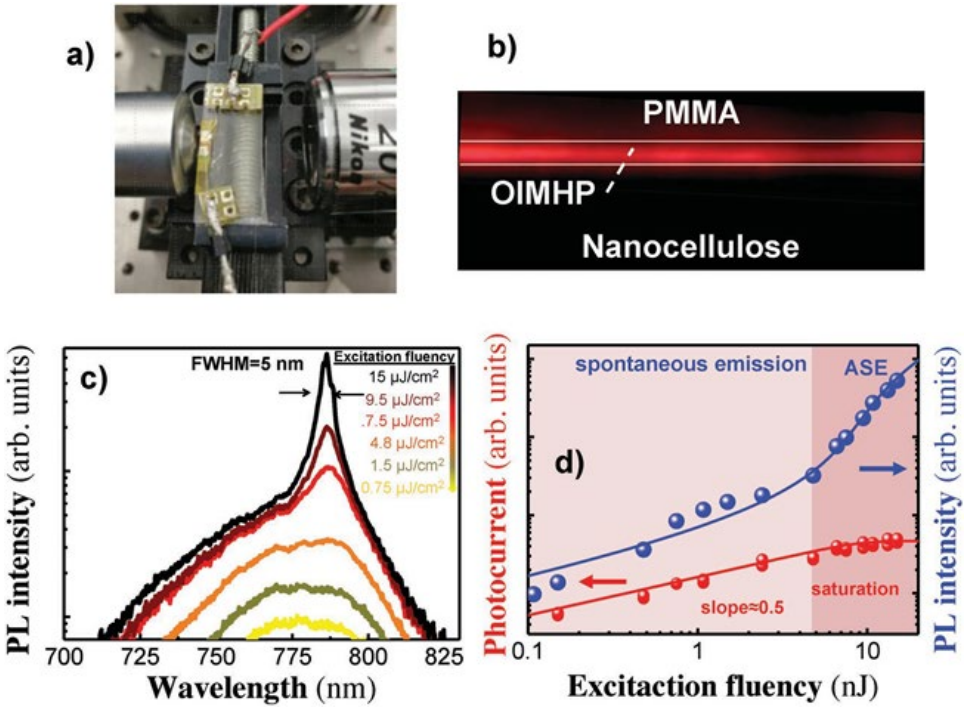


**Figure 4.1.3 Characterization and modeling of the flexible device. a) Picture of holder and photodevice with end-fire excitation/collection objectives. b) PL decoupled at the output edge of the waveguide. c) PL intensity measured for different excitation fluencies collapses to a narrow peak of about 10 nm above a certain threshold. Note the logarithmic scale on Y-axis.d) PL intensity (blue symbols) as a function of the excitation fluency demonstrates a superlinear growth of the PL above the 4 nJ threshold, while photocurrent shows a sublinear increase (red symbols) before saturation, in agreement with the model (solid lines), as explained in the text; photocurrent was measured by applying 10 V on gold electrodes with g = 1 mm.**

The MHP amplifying device fabricated on NC was studied under end-fire coupling of a pulsed laser pumping at 532 nm (WG geometry, as shown in Figure 4.1.3a). Here It is worth to note that we have tested the amplifier device on NC supported on glass (Figure 4.1.3a) or directly the device on stand-alone NC (see Section A.1.6) with similar results. In both cases, the ASE signal collected from the output edge of the WG as a guided mode (see Figure 4.1.3b) exhibits a narrow peak (whose linewidth is 5 nm for the highest laser excitation power used in the experiment, as indicated in Figure 4.1.3c) that grows superlinearly above a threshold of ≈ 4 nJ, as observed in Figure 4.1.3d. This behavior is quite similar as the one observed above under backscattering geometry and previously reported in similar structures integrated on a $Si/SiO_2$ rigid substrate. [15] Such a superlinear growth of the PL intensity (see Figure 4.1.3d) would follow a potential increase

$$I_{PL} \propto I_{PUMP}^{2.5} \qquad \textbf{4.1.4}$$

which would correspond to a gain G = 10 dB $cm^{-1}$ at the output edge of the waveguide (L ≈ 1 mm long) [47] or, in other words, a modal gain (g) of 23 $cm^{-1}$

$$\boldsymbol{G(dB) = 10 \log (e^{g.L})} \quad \textbf{4.1.5}$$

close to the material gain:

$$\boldsymbol{g = \Gamma . g_m} \quad \textbf{4.1.6}$$

since the confinement factor of the optical modes in the MHP film is close to 1. Here it is worth mentioning that PL intensity was stable during the measurement, although similar excitation conditions (20 kHz excitation source) did not show a stable ASE production under backscattering geometry. Therefore, the high confinement of emitted light by the active medium provided by this WG structure enhances the generation of light, and triggers the ASE regime. Moreover, the excitation fluencies shown in Figure 4.1.3c, d correspond to excitation light coupled with the whole PMMA/MHP/NC structure with a cross section of about $2 \times 10^{-5}$ $cm^2$. Nevertheless, since this device propagates the light along the PMMA layer, only a 0.3% of the TE2 mode at 532 nm travels along the MHP, reducing the thermal heating of the semiconductor and the effective ASE threshold (Eth) down to 600 nJ $cm^{-2}$, one order of magnitude smaller than that measured under backscattering geometry in Figure 4.1.2b. This Eth corresponds to an average power of the external pumping laser as low as 0.8 mW, which is estimated by taking into account a coupling efficiency ≈10% inside the waveguide and the repetition rate (20 KHz) of the pulsed laser.

Under the above given excitation conditions, the photocurrent mainly monitors photogenerated carriers by the pump beam travelling along the 1 mm long PMMA/MHP WG, the same distance covered by the Au electrodes. The photocurrent, $\boldsymbol{I_{PC}}$, variation presented in Figure 4.1.3d indicates a clear correlation between $\boldsymbol{I_{PL}}$ and $\boldsymbol{I_{PC}}$, where:

$$\boldsymbol{I_{PC} \propto I_{PUMP}^{0.5}} \quad \textbf{4.1.7}$$

before the saturation observed above $E_{th}$.

Moreover, $\boldsymbol{I_{PC}}$ and $\boldsymbol{I_{PL}}$ dependences can be nicely fitted (solid lines in Figure 4.1.3d) with the model developed in Section A.1.7). The simulations reveal a transparency carrier concentration for stimulated emission $N_0 \approx 1.5 \times 10^{18}$ in agreement with previous results.[16] This square root law for IPC as a function of the excitation fluency corresponds to the high carrier injection regime, while its saturation is attributed to the gain saturation mechanism in optical amplifiers,[144] where the increment of photogenerated carriers over $N_0$ is transformed into photons (stimulated emission regime). In this way, the highest

excitation fluencies reveal IPC up to 25–50 mA $cm^{-2}$ for 100–600 V $cm^{-1}$ applied electric fields inside the waveguide. Finally, it is worth mentioning that the device-on-NC presents again features very close to those obtained for MHP films on rigid substrates (see Section A.1.8), except by a slightly higher peak energy threshold (4 instead of 2 nJ) and ASE linewidth (5 nm instead 2–3 nm) and higher photocurrents.

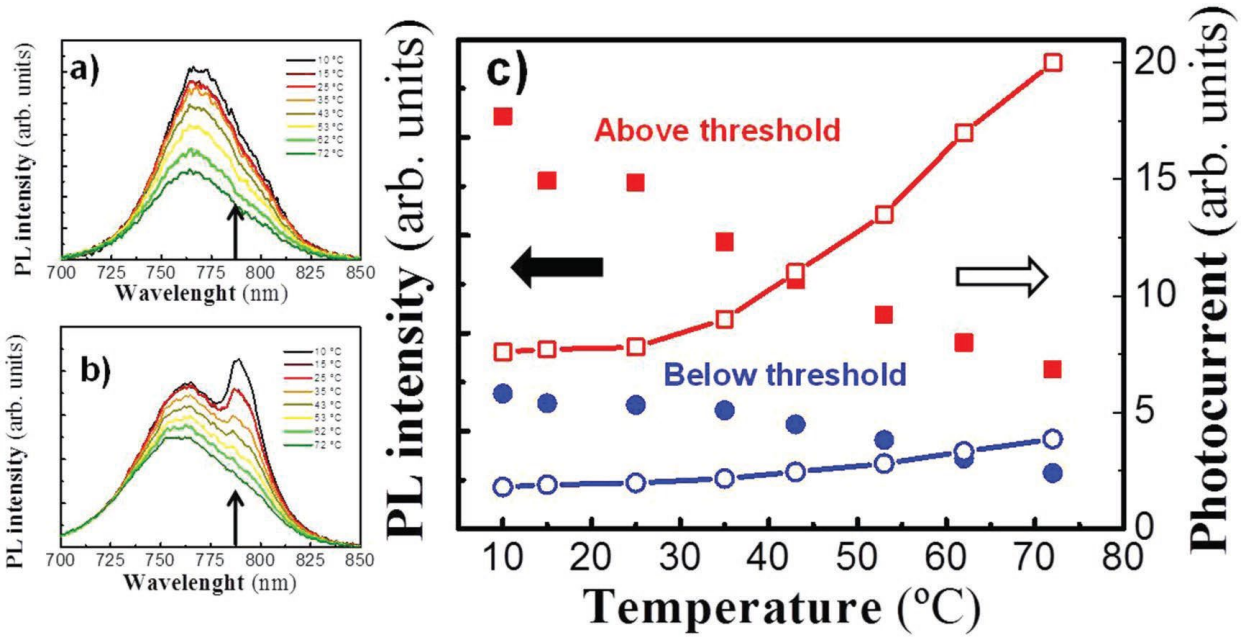


**Figure 4.1.4 Control of operation temperature of the photodevice. a,b) Evolution of PL spectra well below (a) and just above (b) the threshold of ASE for temperatures between 10 and 72 °C. c) PL intensity measured at 790 nm (filled symbols) and photocurrent (empty symbols) as a function of temperature below (blue) and above (red) the ASE threshold; the lines are guides for the eyes. Temperature measurements were done by using a Peltier device with area 1 $cm^2$.**

The integrated amplifier–photodetector device can be used for many applications related to signal amplification and processing at 780–790 nm (telecom, sensing, and other fields) but also at shorter/longer wavelengths by changing the metal or the halide in the MHP compound. One example is high-lighted in Figure 4.1.4. A primary use would be the control itself of the optical amplifier to fix the threshold of operation, specially under temperature changes. If laser fluency is fixed below the threshold the PL peak intensity decreases above room temperature (spectra in Figure 4.1.4a and blue solid circles in Figure 4.1.4c), whereas the photocurrent measured simultaneously at the photodetector suffers a slight monotonous increase (blue hollow circles in Figure 4.1.4c), as expected if the population of free carriers increases with temperature as compared to that of free excitons. However, if laser fluency is fixed just above the threshold, the PL peak at the ASE wavelength decreases in a similar way (spectra in Figure 4.1.4b and red solid squares in

Figure 4.1.4c), but this time the photocurrent is practically constant up to room temperature (red hollow squares in Figure 4.1.4c), due to its saturation regime (see above), and increases much faster when increasing temperature because the ASE regime is progressively lost against spontaneous emission.

## 4.2. Operation Mechanism of Perovskite Quantum Dot Solar Cells Probed by Impedance Spectroscopy

$CsPbI_3$ QDs were synthesized following previous reports.[113] The synthesized QDs were cube-shaped and 9.3 ± 1.5 nm in size as determined by TEM (Figure A.2.1). As reported previously, this synthesis procedure yields QDs in the perovskite crystalline phase as determined by XRD (Figure A.2.2). After QD deposition and subsequent ligand exchange, from the 0.39 theta at full width at half-maximum (FWHM) of the XRD peak corresponding to the (100) plane observed in the samples (Figure A.2.2), a grain size of 21.46 nm is calculated using the Scherrer equation. As expected, there is an increase of the crystal size after ligand exchange but with a size significantly lower than that reported in the standard solar cells. On the other hand, we have previously reported that ligand exchange just partially removes the capping layer of QDs,[145] consequently preserving the capping molecules and providing integrity to the perovskite nanoparticles. The PLQY of the $CsPbI_3$ QDs after a couple of washing processes, in order to remove the organic excess before the deposition, was measured to be roughly 40% in hexane solution. For the fabrication of PQDSCs, $SnO_2$:F (FTO)-coated conductive glass was used as substrate. A compact layer of $TiO_2$ (c-$TiO_2$) was deposited as electron-selective contact[146] on top of the FTO layer (Figure 4.2.1a). A controlled number of layers of $CsPbI_3$ QDs were then spin coated on top of c-$TiO_2$ to vary the active layer thickness of the solar cell. More details about the fabrication process can be found in section 3.2.3. Briefly, a purified solution of $CsPbI_3$ QDs in octane was spin coated, then the film was dipped three times into a methyl acetate or ethyl acetate solution containing $Pb(NO_3)_2$, rinsed in neat methyl acetate or ethyl acetate, and then immediately dried with nitrogen. This complete process constitutes one layer of $CsPbI_3$ QDs and was repeated multiple times to create devices with thicknesses ranging from 150 to 400 nm. On top of the QD film, spiro-OMeTAD was deposited as hole-selective contact. Finally, a 70 nm thick Au layer was evaporated as the hole-extracting contact. In Figure 4.2.1a, the cross section of a PQDSC analyzed in this work is depicted.

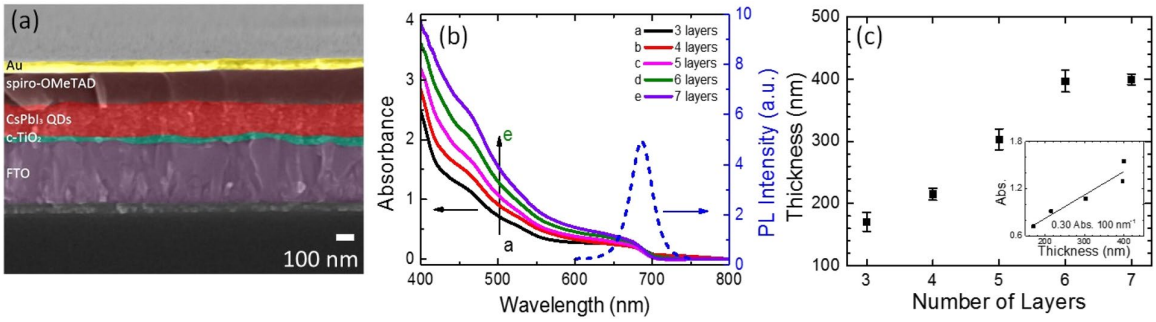


**Figure 4.2.1(a) SEM micrograph of the cross section of a PQDSC with the architecture glass/FTO/compact TiO2 (c-TiO2)/CsPbI3 QD thin film/spiro-OMeTAD/Au. (b) UV−vis absorption spectra (solid lines) of PQDSCs with different number of deposited layers of CsPbI3 and photoluminescence (dashed line). (c) Thickness of CsPbI3 film as a function of the number of deposited layers, measured by SEM. Inset: absorbance at 500 nm, see arrow in panel b, as a function of thickness. The slope of the linear fit is indicated.**

The $CsPbI_3$ QD layer exhibits a photoluminescence (PL) at 689 nm with a FWHM of 30 nm (Figure 4.2.1b). As expected, the light absorption of the QD layers increases with the number of deposited layers (Figure 4.2.1b). The thicknesses of the films were measured from the cross section by SEM (Figure 4.2.1c). Different device batches have been produced and analyzed. Independent of the synthetic batch, the light absorption increased linearly with the number of deposited layers; in the case plotted in the inset of Figure 4.2.1c, the absorbance at 500 nm increased roughly by 0.3 for each 100 nm of QD layer thickness.

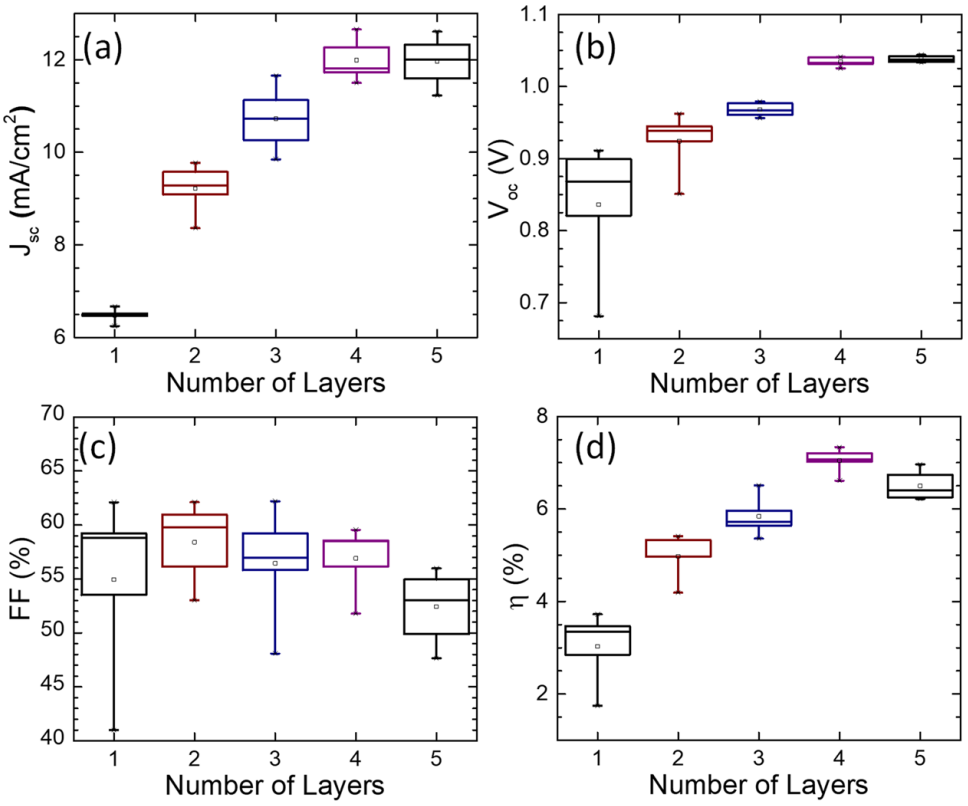


**Figure 4.2.2 Average photovoltaic parameters of the PQDSCs prepared from a QD solution of 50 mg/mL as a function of the number of deposited layers: (a) photocurrent, Jsc; (b) open-circuit potential, Voc; (c) fill factor, FF; and (d) photoconversion efficiency, η.**

Figure 4.2.2 shows the average photovoltaic parameters of the PQDSCs as a function of the number of deposited layers; at least 5−10 cells have been prepared at each thickness. Photocurrent density, $J_{sc}$, and open-circuit potential, $V_{oc}$, panels a and b of Figure 4.2.2, respectively, increased with the number of layers, saturating for large numbers. J−V curves of representative devices with different numbers of layers are plotted in Figure A.2.3. On the other hand, fill factor, FF, remains practically constant with the number of layers, taking into account the error bars. Consequently, the power conversion efficiency, η, increased with the number of deposited QD layers until a maximum average efficiency is reached for 4 layers, in the conditions of preparation of the batch depicted in Figure 4.2.2. Further deposition of layers decreased the performance due mainly to the reduction of FF. In this study, a maximum efficiency of 8.1% was obtained with $J_{sc}$ = 11.3 mA/cm$^2$, $V_{oc}$ = 1.094 V, and FF= 66% (Figure A.2.4). Different batches have been prepared by changing some deposition parameters, such as the concentration of QDs, or the ligand exchange procedure.

In all the analyzed batches, the solar cell parameters exhibit the same trend as reported in Figure 4.2.2.

When the performances obtained for PQDSCs are compared with state-of-the-art PSCs based on bulk thin film,[67] FF and especially $J_{sc}$ are significantly lower for PQDSCs. Higher FFs have been reported for PQDSCs, ~80%;[84] in our case, the low FF is probably due to the c-$TiO_2$, because this selective contact plays a fundamental role in the performance and FF of perovskite solar cells.[147] However, the weakest photovoltaic parameter for PQDSCs compared to conventional thin films is the photocurrent. $J_{sc}$ has been improved by the use of cation halide salt treatment.[84] Nevertheless, this parameter still requires improvement because the reported one for the record PQDSCs,[46] 15.246 mA/cm$^2$,[84] remains low in comparison with PSCs. This limitation is mainly due to the low incident photon to current efficiency (IPCE) at longer wavelengths (Figure A.2.5). Thin QD layers do not allow the complete harvesting of the long-wavelength region, whereas an increase of thickness does not necessarily solve this issue as carrier transport limitations arise.

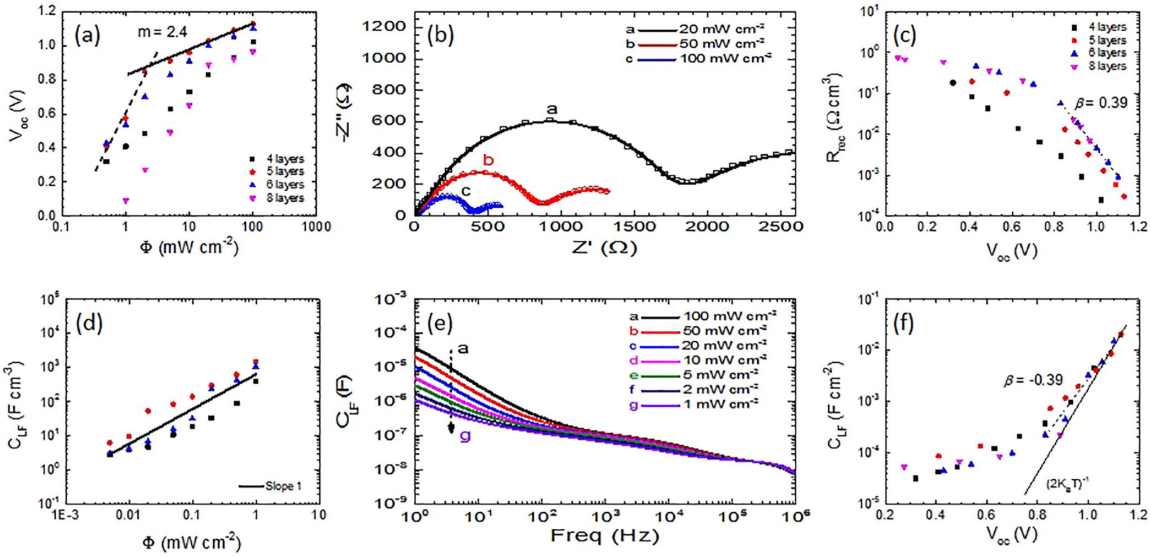


**Figure 4.2.3 Optoelectronic characterization of PQDSCs with different thicknesses. (a) Open-circuit potential as a function of the light intensity. Solid line is a straight line with m = 2.4. (b) IS Nyquist plot at applied bias equal to the device Voc for three different light intensities. Symbols are experimental data, whereas solid lines correspond to the fit using the equivalent circuit plotted in Figure A.2.6. (c) Recombination resistance, Rrec. The dashed line is the linear regression of experimental points at high applied bias according to eq. 4.2.1 for the two thicker layers. (d) Low-frequency capacitance as a function of light intensity. (e) Bode plot at Voc applied bias under different light intensities where the dashed arrow indicates the evolution of the impedance spectra as light intensity is reduced. (f) CLF as a**

**function of Voc. The dashed line is the linear regression of experimental points at high applied bias, whereas the solid line represents a straight line with slope defined by β = 0.5**

To obtain a better understanding of PQDSCs, measurements at various light intensities were systematically performed. Details about the experimental procedure can be found in section 3.2 and the recent contribution.[131] In Figure 4.2.3a, we plot $V_{oc}$ as a function of the light intensity. This representation allows for the easy calculation of the diode ideality factor, m, simply by the linear fit of the data.[148] Figure 4.2.3a points to two different working regimes: at low and at high light intensities characterized by different ideality factors. At low light intensities, m presents values significantly higher than 2 that could be assigned to a recombination process with multiple trapping events through-out a distribution of trap energies.[148] High m values have not been reported for standard PSCs using compact $TiO_2$ and spiro-OMeTAD as electron- and hole-selective contacts, respectively,[148, 149] and consequently, this multiple-trapping process at low light intensities would be associated with the perovskite QD layer. However, pinholes could also produce this high m behavior, and this explanation cannot be completely ruled out especially in the case of the thinnest layers. At higher light intensities, m reduced to 2 for the thickest samples as most of these traps are filled, pointing to an elimination of trapping leaving only Shockley−Read−Hall recombination at deep trap states.[148] Note that the small shunts produced by pinholes could be overwhelmed at high illumination, and similar behavior should be expected. Pinholes are especially influential in the cell performance for thinner samples; in fact, the thinnest layer in Figure 4.2.3a presents an ideally factor m greater than 2 even at high illumination. Analysis of recombination resistance, see below, also points to the presence of pinholes, especially in the case of the thinnest samples.

Impedance spectroscopy has been performed with an applied bias equal to $V_{oc}$ under different light intensities.[131] While there is a lack of consensus on interpretation of such IS patterns, an interesting qualitative comparison can be performed to detect differences between PSCs and PQDSCs. As in the case of conventional thin-film PSCs, two main features (arcs) at high and low frequency are presented in the Nyquist plot (imaginary part of the impedance, $Z''$, vs real part of the impedance, $Z'$)[147, 150-152] (Figure 4.2.3b). A closer inspection of the Nyquist plot points to a more complex system, as the high-frequency feature, the left-hand side feature with lower $Z'$, is not a single arc but better represented as two merged arcs at high frequency.[147] Consequently, we have used an equivalent circuit previously employed for PSCs,[29] containing an intermediate frequency arc, to fit the experimental data (Figure A.2.6). This equivalent circuit model can accurately fit the experimental measurements (Figure 4.2.3b). The impedance spectra of PQDSCs are

analogous to those observed for standard PSCs, and consequently the same equivalent circuits can be used to simulate the performance of both devices.

Impedance fitting allows the comparison of different parameters as a function of the number of layers Figure 4.2.3c plots the recombination resistance, $R_{rec}$, normalized to QD thin-film volume for different PQDSCs obtained as the sum of low- and high-frequency resistances;[28, 153] more details are presented in Figure A.2.7. $R_{rec}$ depends inversely on the recombination rate[94] and consequently can provide a direct quantitative view of the recombination process. $R_{rec}$ can also be obtained as the lifetime divided by the chemical capacitance.[94] $R_{rec}$ depends on carrier density and consequently on the applied bias, following a relation of the type[94]

$$\boldsymbol{R_{rec} = R_0 exp\left(-\frac{\beta q V}{k_B T}\right)} \qquad \textbf{4.2.1}$$

where $R_0$ is the recombination resistance at short circuit, q the elementary charge, $k_B$ the Boltzmann constant, T the absolute temperature, and β a dimensionless parameter related with the ideality factor m as one is the inverted value of the other (m = 1/β).[154] Good agreement is obtained between m and β values obtained in panels a and c of Figure 4.2.3, respectively, indicating the correctness of the experimental procedure.

From Figure 4.2.3c, we find that the recombination resistance normalized to the volume of the QD layer is improved as more layers are deposited up to saturation at 6 layers. This fact explains the increase in $V_{oc}$ observed in Figure 4.2.2b by a reduction of the recombination rate as the deposition of multiple layers reduces potential pin holes and inhomogeneities.

Especially interesting is the characterization of low-frequency capacitance, $C_{LF}$, as this capacitance is the most characteristic and recognizable feature of the impedance pattern of PSCs.[139] In PSCs, an increase in the $C_{LF}$ of several orders of magnitude, even at zero applied bias, has been observed between dark conditions versus 1-sun illuminations, in contrast with other photovoltaic technologies such as Si where a minimal change is observed.[139] On the other hand, $C_{LF}$ is not observed in all-solid state dye-sensitized solar cells either,[155] where the same selective contacts are used; consequently, its origin is attributed to the perovskite layer and/or the interaction of the perovskite layer with the selective contacts. The physical origin of this capacitance is not clear, and different models have been proposed. However, many of these models, especially the most recent ones, agree in identifying the ionic migration as the fundamental origin of this phenomenon. On one hand, this capacitance has been associated with the accumulation of majority carriers at the $TiO_2$ interface, and it is observed at low frequency as the accumulation process is

coupled with the ion migration.[156] On the other hand, light-induced ion migration has been pointed out as the origin of the behavior.[157] In addition, the interplay between ionic and electronic charge transfer at perovskite− contact interfaces controlling electronic injection and recombination[158] and ion-modulated recombination have been also indicated as the possible origin of the behavior.[159] Consequently, there is a broad consensus on the ionic origin of this feature characterizing PSCs. Moreover, it has been reported that the J−V curve hysteresis observed for PSCs is related to ion migration,[159-162] and in fact a reduction of hysteresis has been related to a decrease of $C_{LF}$, connecting both effects with the ion migration behavior in halide perovskites.[159, 160, 163]

In the case of PQDSCs, it is notable to observe that the $C_{LF}$ follows a similar behavior as in standard PSCs, exhibiting a linear increase of several orders of magnitude with light illumination (Figure 4.2.3d). This behavior can be clearly observed at lower frequencies of the Bode plot of PQDSCs at applied bias equal to the $V_{oc}$ at different light illuminations (Figure 4.2.3e). This similarity strongly points to an analogous origin of $C_{LF}$ in both PSCs and PQDSCs and an origin linked with ion migration, as has been suggested for PSCs. However, further research is needed to fully confirm this point.

A close inspection of $C_{LF}$ at different illuminations at $V_{oc}$ conditions allows us to differentiate two working regimes at low and high illumination (Figure 4.2.3f). Note that in Figure 4.2.3f $C_{LF}$ is normalized to the device area and not to the QD layer volume. At high light intensity all four devices present the same $C_{LF}$ independent of the thickness, pointing to a process where interfacial effects play a major role. It is interesting to note that at high light intensities $C_{LF}$ presents an exponential behavior and can be fitted with a phenomenological equation analogous to eq. 4.2.1:

$$\boldsymbol{C_{LF} = C_0 exp\left(-\frac{\beta qV}{k_B T}\right)} \qquad \textbf{4.2.2}$$

where $C_0$ is the low-frequency capacitance at 0 bias. A $\beta = -0.39$ is obtained for $C_{LF}$ at high applied bias, see Figure 4.2.3f, while a complementary value of 0.39 was obtained for $R_{rec}$ at high applied bias (Figure 4.2.3c). Both β values are in good agreement with the ideality factor measured independently in Figure 4.2.3a. On the other hand, very similar values of β for the high and low resistances have been also obtained (Figure A.2.7). This complementarity of $C_{LF}$ and $R_{rec}$ slopes has been previously observed for standard PSCs,[28] where a β value of – 0.5 was observed. A solid straight line corresponding to this β value is plotted in Figure 4.2.3e with a solid line for comparison. The $\beta = -0.5$ slope of the capacitance slope has been previously associated with the characteristic behavior of the interfacial charge accumulation.[28, 156, 164] The complementarity of the slopes

points to a common effect linking recombination and ion migration through $R_{rec}$ and $C_{LF}$, respectively. It has been calculated that interstitial iodine defects introduce deep electron/hole traps in $CH_3NH_3PbI_3$;[165] if these defects are the main factor responsible for the nonradiative recombination process, the recombination process would be affected by the ion migration, as the behavior of $R_{rec}$ and $C_{LF}$ suggests. Note that two regimes can be also distinguished for $R_{rec}$ and $C_{LF}$ at low and high applied bias, corresponding with the low and high regimes previously discussed regarding the light intensity dependence in Figure 4.2.3a.

A further comparison between PQDSCs and PSCs can be performed taking into account the impedance measurements. A characteristic time, $\tau$, can be defined as $C_{LF} \times R_{rec}$ (Figure A.2.8). Note that $\tau$ is not a lifetime because $C_{LF}$ is not a chemical capacitance.[166] Because of the complementary value of $C_{LF}$ and $R_{rec}$, a value $\sim$1 s is obtained, which is lower in the case of the thinner layer (Figure A.2.8). Characteristic times of the same order, measured by alternative transient techniques, have been reported for PSCs.[152, 167] This characteristic time has been shown to be independent of the applied bias and light illumination but decreasing with the thickness and depending on the perovskite material and the selective contacts.[28] The value of $\tau$ here obtained for PQDSC is very similar to that reported for planar PSCs of the same thickness when fabricated and having selective contacts with $MAPbI_3$ and 1 order of magnitude greater than a planar cell of $FAPbI_3$, where MA is methylammonium and FA formamidinium. Additionally, PQDSCs present a $\tau$ 3 orders of magnitude greater than that of planar PSCs of the same thickness fabricated and having selective contacts with MAPbI3 but with inverted configuration and organic selective contacts.[28]

The impedance spectroscopy analysis of PQDSCs is remarkably similar to the most characteristic trends of standard PSCs yet not observed in other cells: increase of several orders of magnitude of $C_{LF}$ with light illumination (Figure 4.2.3d,e); complementary slopes of $R_{rec}$ and $C_{LF}$, panels c and f of Figure 4.2.3, respectively; and nearly constant characteristic time $\tau = C_{LF} \cdot \times R_{rec}$ (Figure A.2.8). Consequently, our study preliminarily suggests that the PQDSCs present the same working mechanism as PSCs.

It will be important to further confirm this preliminary result as important conclusions could be obtained from this similarity. Concretely, $C_{LF}$ presents a behavior similar to that observed for PSCs, pointing to an important ion migration effect in PQDSCs, despite the fact that different ion migration properties might be expected between the PQDSCs and standard PSCs because of the structural differences between a thin film where QDs act as

a brick to build a continuous thin film with crystalline grains of hundreds of nanometers. It is expected that the presence of an organic capping on a perovskite QD surface would likely influence the ion migration process in perovskite QD layers. In fact, there are anions on the QD surface just to balance the charge. Those anions could migrate under a field through the voids in the QD layer.[91] In our case, ligands from the as-synthesized QDs were removed to reduce the interdot distance and to insolubilize the QDs on the substrate so that multiple layers could be coated.[113] Rapid and facile halide exchange in QD solutions has been observed because of the dynamic surface properties of QD perovskites in solution, and this effect can be used to create homogeneous halide alloy compositions.[108] Appropriate surface capping properties can reduce this effect.[168-170] The impedance analysis carried out in this work for PQDSCs shows clearly a behavior analogous to that in standard PSCs for $C_{LF}$, which is usually attributed to ion migration as we have previously discussed. The implication in PQDSCs will need further research. In this sense, impedance spectroscopy arises as a highly appealing method for characterization of PQDSCs in general and ion migration in particular.

## 4.3. Ligand & Band Gap Engineering: Tailoring the Protocol Synthesis for Achieving High-Quality $CsPbI_3$ Quantum Dots

For the standard hot-injection synthesis of $CsPbI_3$ QDs, in addition to the perovskite precursors, OA and OLA were added for the stabilization of the colloidal QDs.[81] Consequently, the injection of a higher OA/OLA content allowed us to synthesize QDs at higher synthesis temperatures than conventional synthetic protocol, in order to obtain QDs with improved photo-physical properties. With the purpose to understand how the temperature affects the synthesis of $CsPbI_3$ QDs, first of all, the reaction between OA and OLA was studied at different temperatures. Samples of OA, OLA and a mixture of them (1: 1 molar ratio) were heated at 120 °C under vacuum or nitrogen (mimicking the QDs synthesis conditions), and heated at the desired temperature (between 120 and 200 °C). Then, the samples were cooled down to ambient temperature and analyzed by $^1H$ NMR (Nuclear Magnetic Resonance) spectroscopy. We excluded the use of 1-ODE as this reagent is a non-coordinating solvent and does not take part in the reaction, but generates extra peaks in NMR analysis.

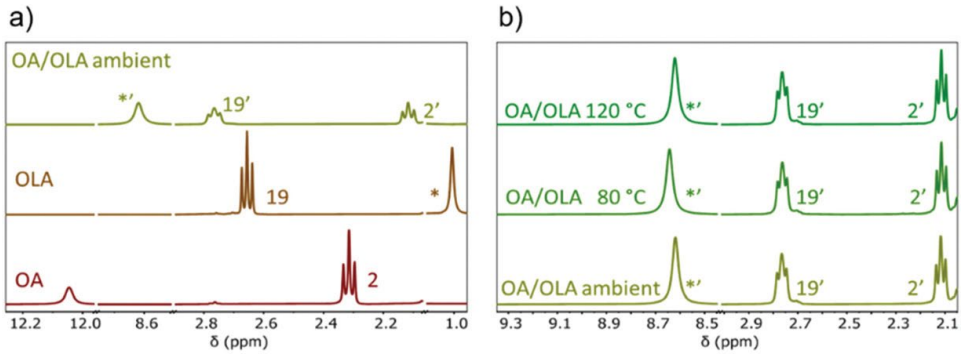


**Figure 4.3.1 (a) $^1$H NMR spectra ($CDCl_3$, 400 MHz, 25 °C) of OA and OLA capping ligands and their mixture to follow the formation of OLM at room temperature. (b) Comparison of the $^1$H NMR spectra ($CDCl_3$, 400 MHz, 25 °C) of the mixture at ambient temperature, 80 and 120 °C. Asterisks added in the Figure 4.3.1a and b denote the proton associated with the amine group from OLA (*), and the ammonium functionality from OLM (*').**

Figure 4.3.1a shows the comparison between the $^1$H NMR spectra of OA, OLA and the OA/OLA mixture prepared at ambient temperature. The resonance due to the proton from the carboxylic acid group of OA appears at a chemical shift (δ) of 12.04 ppm, while the resonance due to the protons of the amine group of OLA appears at δ = 1.01 ppm (denoted as *). When the reagents are mixed together, the signal corresponding to the proton of the carboxylic group disappears and the signal at δ = 1.01 ppm shifts to 8.6 ppm (denoted as *′), due to the protonation of the amine group ($–NH_2$) in favor of the ammonium group ($–NH_3^+$). The resonances of the methylene groups also shift, compared to the spectra of the starting materials, due to a different chemical environment. These results corroborate the gene-ration of a new species, namely oleylammonium oleate (OLM), even at room temperature, formed by the protonation of OLA.[114, 171] Then, by heating the OA/OLA mixture at 80 °C and 120 °C and then cooling down to room temperature, it is clear that the triplets corresponding to the α-$CH_2$ resonances next to the carbonyl (2′) and ammonium (19′) functionalities of OLM remain unchanged and there is a negligible shift of the signal from the $NH_3^+$ group (Figure 4.3.1b). This fact is an evidence that the reaction, under these conditions, fully transforms the initial OA and OLA into OLM.

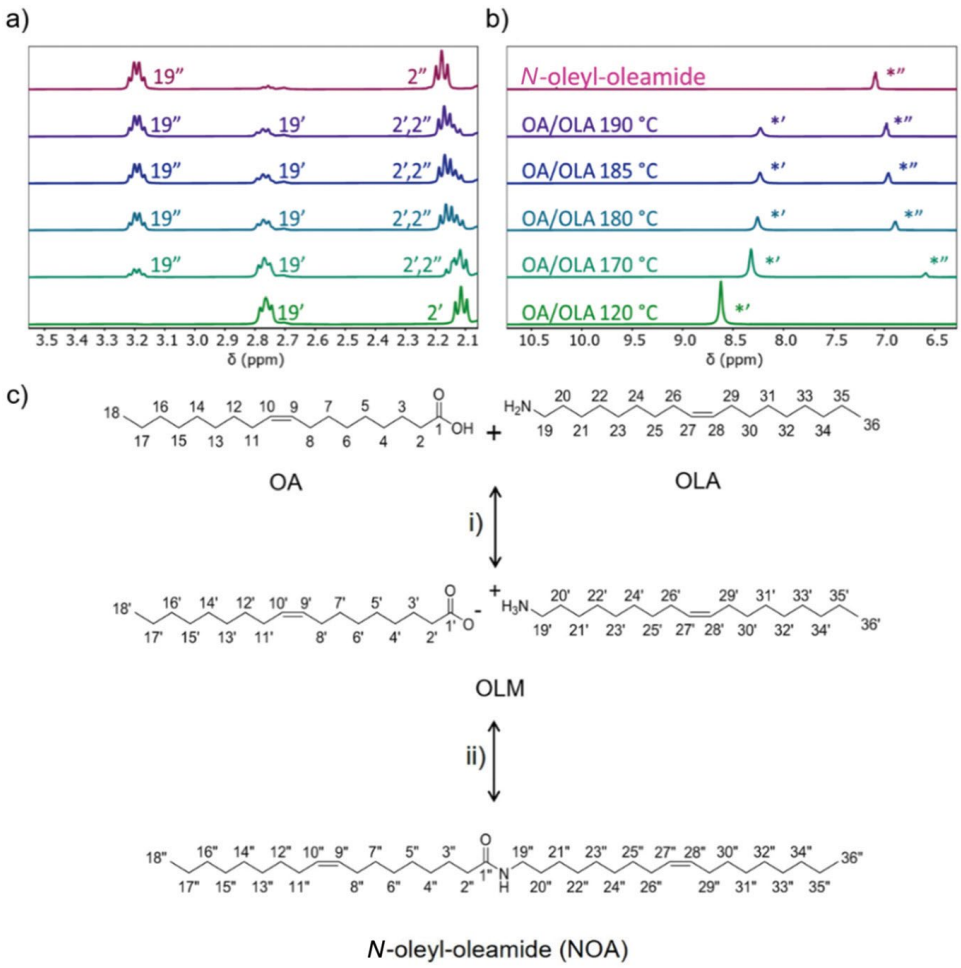


**Figure 4.3.2 $^{1}$H NMR spectra of the OA/OLA 1:1 molar ratio mixtures ($CDCl_3$, 400 MHz, 25 °C) at different temperatures, showing the formation of N-oleyl- oleamide from the OLM at (a) low and (b) high chemical shift. (c) Schematic representation of the reaction between oleic acid and oleylamine to produce (i) OLM oleate and (ii) N-oleyl-oleamide (NOA). Asterisks added in Figure 4.3.2b indicate the proton associated with the amide group from NOA (*”).**

By increasing the temperature of the OA/OLA mixture from 120 °C to 190 °C, obtaining their corresponding $^{1}$H NMR spectra (Figure 4.3.2a), the intensities of the triplets belonging to the α-CH2 resonances next to the ammonium and carbonyl functionalities of OLM (19′ and 2′, respectively) either decrease or change shape, from triplet to multiplet, and concomitantly a new multiplet centered at δ 3.20 ppm appears. Moreover, the appearance of a new peak at δ 7.1 ppm is associated with the formation of an amide as the product of the condensation reaction (denoted as *″).[114, 172] This result is in good agreement with the decrease of the signal associated with the ammonium group at 8.6 ppm (Figure 4.3.2b). In order to confirm the formation of the amide, we intentionally synthesized N-oleyl-oleamide (NOA) by mixing OA and OLA at 190 °C[129] under

vacuum over-night and characterized the final product by $^{1}H$ and $^{13}C$ NMR (Figure A.3.1a). The spectra of the synthesized product perfectly match those of the mixture of reagents at 190 °C, thus con-firming the presence of NOA. This by-product has been reported to appear at 160 °C during the synthesis of $CsPbX_3$ (X = Cl, Br, and I).[173] Moreover, in comparison with the individual liquid capping ligands (OLA and OA), the aspect of the mixture changes from a viscous liquid to a white solid, passing from a mixture of liquid and solid states (Figure A.3.1b). OLM is more viscous than OA and OLA at room temperature.

The amide compound, which has a melting point of around 50 °C, emerges as a white solid when it is mixed with OLM at room temperature. The white solid was not observed neither during the synthesis nor in the NMR tube due to the presence of octadecene and $CDCl_3$, respectively, both of which were able to dissolve the amide. All these findings are not in line with the previous mechanisms proposed, in which a progressive increase in the temperature induces the protonation of oleate by oleylammonium at temperatures as high as 100 °C (Figure 4.3.2c(i)).[114, 171] This discrepancy could be due to the preparation of the NMR samples. If traces of water remain during the NMR sample preparation, the amide by-product could be dissociated, affording the reagents (Figure 4.3.2c(i)) and leading to different species in the reaction mixture. By conducting the synthesis at high temperatures under an inert atmosphere, the condensation product NOA is formed (Figure 4.3.2(ii)), as we estimated also by an NMR quantitative analysis (see Table 4.3.1). By integrating the corresponding NMR peaks (Figure A.3.2a–f) and considering the concentration (or volume) of OA and OLA added during the QD preparation, we quantitatively calculated the concentration of OLM and NOA. It is observed that the concentration of the former decreases while that of the later increases with temperature (see Table 4.3.1 and Table A.3.1).

**Table 4.3.1 NMR quantitative analysis of the evolution of different amounts of OA and OLA (1: 1 molar ratio), OLM and NOA products at different temperatures. OA and OLA are initially fully transformed into OLM (see Figure 4.3.2c(i)) and finally a part of OLM is transformed into NOA (see Figure 4.3.2c(ii))**

| Temperature (° C) | Initial number of moles of OLM (=OA or OLA) (mmol) | Number of moles of OLM after transformation (mmol) | Number of moles of NOA after transformation (mmol) | Conversion of OLM to NOA (%) |
|---|---|---|---|---|
| 170 | 4.6 | 3.4 | 1.2 | 26 |
| 180 | 9.1 | 4.0 | 5.1 | 56 |
| 185 | 12.2 | 4.5 | 7.7 | 63 |
| 190 | 12.2 | 4.0 | 8.2 | 67 |

To stabilize the lead halide precursor during the QD synthesis, we took into consideration the NMR results. We modified the synthetic protocol by increasing the concentration of

both OA and OLA[114, 174-176] as the reaction temperature increases.[113, 177] Four temperatures (170, 180, 185, and 190 °C) were used for the $CsPbI_3$ QD synthesis, by varying the concentrations of OA and OLA, always in a 1 : 1 molar ratio (see Table 4.3.1).[81] In all the cases, $CsPbI_3$ QDs were successfully pre-pared, including the synthesis at higher temperatures (see Figure A.3.3). In order to avoid the problems observed in the QD synthesis at temperatures higher than 180–185 °C, at which the precursor is not well solubilized and precipitated,[113, 114] it is needed to increase the concentration of OA and OLA in order to increase the amount of OLM (see Table 4.3.1). The spontaneous organization of the long aliphatic chain of OLM coordinating the lead iodide precursor can react with Cs-oleate and form $CsPbI_3$ QDs. Consequently, the presence of OLM in the reaction mixture is essential to promote the stabilization of $CsPbI_3$ QDs. If the concentration of OLM is not increased ( by increasing the OA and OLA precursors, see Figure 4.3.2c(i)), when the synthesis temperature is enhanced, the final amount of available OLM decreases with temperature due to the fact that higher synthesis temperatures accelerate the transformation of OLM to produce NOA through the condensation reaction (formation of amide bound) (see Figure 4.3.2c(ii)). The lead iodide precursor was dissolved in OLM, which resulted in a complex of $PbI_2$ coordinated to oleylammonium iodide and Pb-oleate, as authenticated by the transparent lemon color of the solution. When the amount of OLM is not high enough to produce this coordination, an orange-reddish precipitate is obtained due to $PbI_2$ precipitation. This is commonly observed when the QD synthesis is attempted at T > 180 °C, with no further increase in the standard OA and OLA concentrations. The increase in the OA and OLA concentrations needs to consider the partial loss of OLM transformed into NOA. This loss increases as the temperature rises (see the percentage of OLM conversion into NOA in Table 4.3.1). Consequently, we increased the OA/OLA con-centration between 20 and 60% compared with the conventional hot-injection method, in order to allow the synthesis at higher temperatures that indeed modified the properties of the QDs, as we discuss below.

Moreover, OLM does play a key role not only in the QD syn-thesis, but also in their passivation and consequently, in the final QD properties.[127, 178, 179] Thus, at higher temperatures, more amounts of OA and OLA are needed to ensure that enough OLM is available to first fully stabilize $PbI_2$ allowing the QD synthesis and later to passivate the QD surface. Therefore, it is expected that a higher amount of OLM favors the QD surface passivation with important implication in the QD properties and also in the long-term stability, as non-passivated surface $I^-$ vacancies are mainly responsible for the self-degradation of QDs.[180]

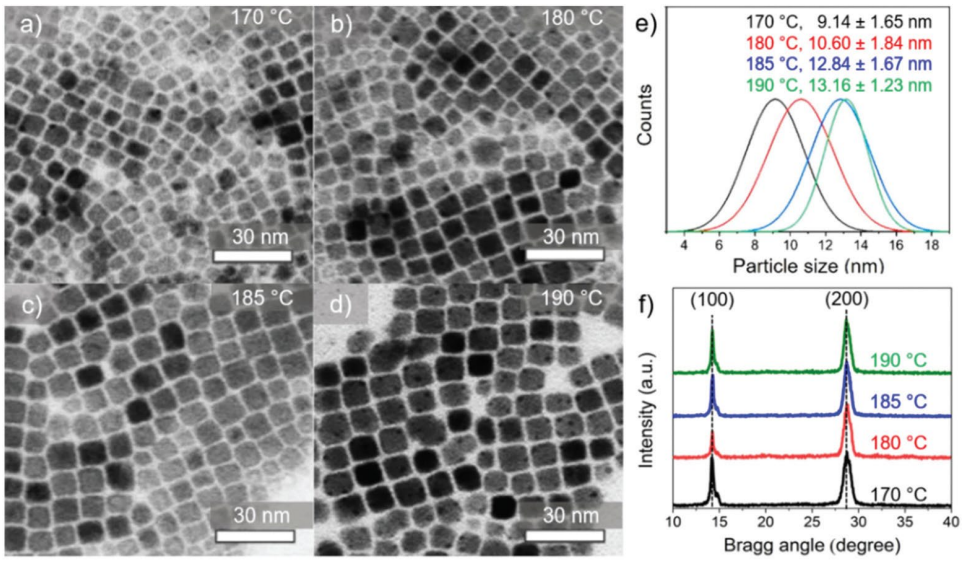


**Figure 4.3.3 (a–d) TEM images, (e) particle size distributions obtained from TEM and (f) XRD patterns of the $CsPbI_3$ QD solutions obtained at diverse synthesis temperatures: 170, 180, 185 and 190 °C.**

Figure 4.3.3a–d show the TEM images of synthesized $CsPbI_3$ QDs obtained under the conditions reported in Table 1. In all the cases, nanocrystals with a nanocube shape are obtained. The rise of the synthesis temperature increases the average nano-particle size between 9.1 nm and 13.2 nm, but decreases the QD size distribution, see Table 4.3.2 and Figure A.3.4 Thus, all the synthesized QDs exhibit the quantum confinement regime (QCR) effects as the Bohr diameter for $CsPbI_3$ is around 13 nm.[81] After hot-injection of $Cs^+$ species into the $PbI_2$ precursor, a broad population of small and big QDs are formed, which depends on the concentration of dissolved $Cs^+$,$Pb^{2+}$ and $I^-$ species in the reaction medium. Koolyk et al.[181] reported a size standard distribution of $CsPbI_3$ QDs to be between 2.9 and 3.4 nm for QD sizes between 7.5 and 10.5 nm, by increasing the reaction time from 4 to 20 s (before quenching). In the same line, Zhao et al.[182] reported a size distribution in $CsPbI_3$ QDs between 1.7 and 2.2 nm for QD sizes between 13.9 and 15.3 nm. In our case, the reaction time is limited to 5 s, obtaining a lower size distribution between 1.23 and 1.65 nm for QD sizes between 9.1 and 13.2 nm (Table 4.3.2). We deduced that the increase of the synthesis temperature instead of the reaction time can mediate a fast consumption of the above-mentioned species supporting the growth of small QDs to reach the size of larger ones, which present a slower particle growth rate.[181] In our case, this phenomenon can favor the QD population to be in the same size range, narrowing the particle size distribution.[114, 181] Moreover, an increase of the temperature produces an increase of the NOA formation that could increase the viscosity, decreasing the diffusion of the reactants. Thus, the proven progressive increase in NOA formation with

an increase in temperature (see Table 4.3.1) could produce a higher limitation of the reaction by diffusion, which is proved to be one of the requirements of narrowing the particle size distribution.[183, 184]

**Table 4.3.2 Summary of the different structural and optical parameters of the $CsPbI_3$ QDs analyzed in this work. Size dispersion is calculated considering the standard deviation with respect to the QD size**

| Synthesis temperature (°C) | Size of QD (nm) | Size standard distribution (nm) | Size dispersion (%) | PL peak (nm) | PL FWHM (nm) (meV) | Initial PLQY (%) | Reduction of PLQY after 15 months (%) |
|---|---|---|---|---|---|---|---|
| 170 | 9.14 | 1.65 | 18.05 | 677 | 44.6 (121) | 87 | 21 |
| 180 | 10.60 | 1.84 | 17.36 | 681 | 42.4 (113) | 91 | 16 |
| 185 | 12.84 | 1.67 | 13.01 | 685 | 37.6 (100) | 93 | 7 |
| 190 | 13.16 | 1.23 | 9.34 | 687 | 36.0 (94.8) | 92 | 8 |

Furthermore, the XRD profiles of $CsPbI_3$ QDs were also acquired, and they exhibit two main diffraction peaks at Bragg angles around 14.2° and 28.7°, see Figure 4.3.3f. These signals are associated with the (100) and (200) planes in the perovskite lattice, respectively, which are the characteristic signals of a cubic phase (ICSD 540752).[74, 185] This crystalline phase has been reported to be preferential when the $CsPbI_3$ QD synthesis is performed at temperatures between 170 and190 °C,[81, 108] and it is retained under room conditions due to the high surface energy generated in the confined QDs.[113, 182] According to these results, we deduced that the increase of the capping ligand concentration in the conventional hot-injection method (see Table 4.3.1) is essential for the stabilization of $CsPbI_3$ QDs at higher reaction temperatures, with bigger and more homogeneous particle size, presenting in all the cases, a nanocube shape and a crystalline cubic phase.

In an attempt to synthesize QDs at 200 °C, we kept increasing the amounts of OA and OLA added to the reaction mixture similar to that carried out in the previous synthesis processes. Unfortunately, the $PbI_2$ precipitation was observed, avoiding the preparation of QDs. At this stage, we deduced that higher transformation of OLM into NOA taking place at this temperature showed a stronger influence on the QD synthesis than the increase of the capping ligand content, blocking the growth of QDs. From this observation, it is clear that the QD synthesis at temperatures ≥200 °C demands extra modifications to our syn-thetic route, where the increase of capping ligand ratio is not enough to mediate the stabilization of the lead precursor (see below).

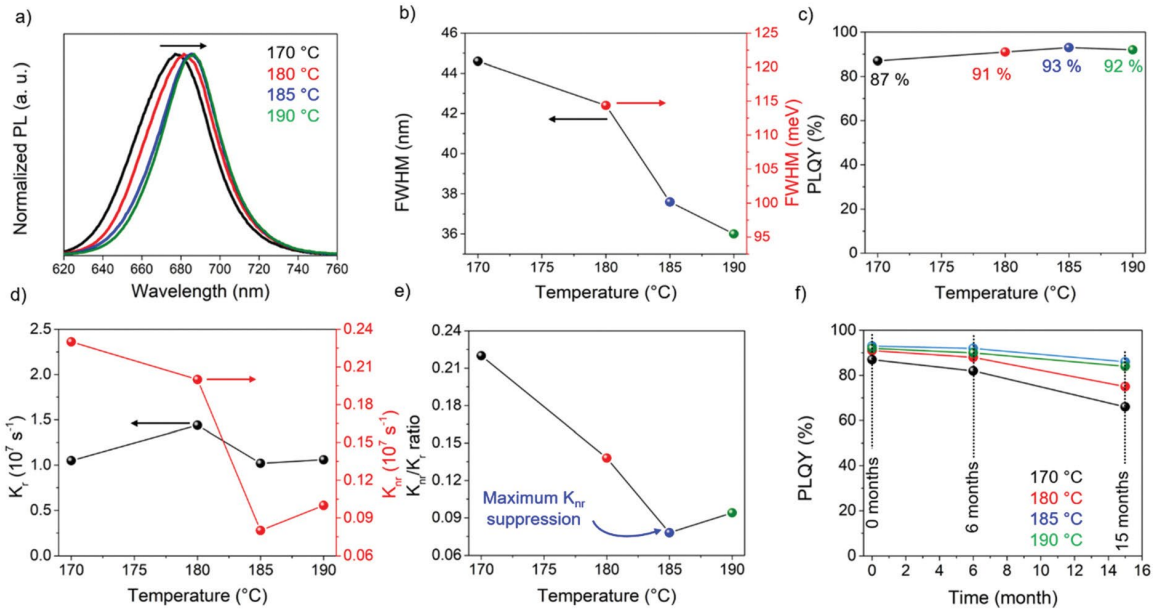


**Figure 4.3.4 (a) Normalized photoluminescence spectra, (b) full width at half-maximum (FWHM), (c) absolute photoluminescence quantum yield (PLQY) of the as prepared QD solutions. (d) Radiative ($K_r$) and non-radiative recombination ($K_{nr}$) decay constants, and the corresponding (e) $K_{nr}/K_r$ ratio for QD solutions after 6 months of storage. (f) PLQY stability for 15 months for $CsPbI_3$ QDs prepared at different synthesis temperatures.**

Given that the $CsPbI_3$ QDs size was directly influenced by the synthesis temperature, it was also expected that this parameter would have impact also on the optical features of these materials. The PL peak positions of the $CsPbI_3$ QDs prepared at different temperatures are depicted in Figure 4.3.4a. As the synthesis temperature increased, the emission peak positions were red-shifted. This trend indicates the narrowing of the bandgap, $E_g$, due to a relaxation of the QCR as the size of QDs increases. Moreover, the bigger the $CsPbI_3$ QDs, the narrower the full width half maximum (FWHM) of the corresponding PL peaks (Figure 4.3.4b), obtaining values as low as 36 nm (94.8 meV) for QDs grown at 190 °C (see Table A.3.2) This value is lower than the conventional FWHM reported for red-emitting $CsPbI_3$ QDs (around 40 nm)[108, 186] and is similar to the FWHM of near unity PLQY $CsPbI_3$ QDs synthesized by adding organic precursors (for instance, trioctylphosphine or 2,2′-iminodibenzoic acid) in accordance with a perovskite stabilization.[105, 125] This comparison infers that by a simple modification in the hot-injection method protocol without using extra chemical stabilizers, we were able to enhance the quality of the materials. The reduction of the FWHM is in good agreement with the reduction of the QD size dispersion from the average size and the corresponding size standard distribution obtained using TEM images (see Table 4.3.2, Figure 4.3.3e and Figure A.3.4). This fact clearly demonstrates that the population of QDs is more prone to

be in the same particle size range by increasing the synthesis temperature as we discussed above, and high density QDs with smaller band gaps (reduced QCR) will emit at the same wave-length. Thus, a lower size dispersion narrows the PL FWHM, improving the color purity of $CsPbI_3$ QDs as the synthesis temperature increases.

The PLQY of $CsPbI_3$ QDs is also influenced by the synthesis parameters (see Figure 4.3.4c). By carrying out the QD synthesis at temperatures between 170 and 185 °C, we evidenced an increase of the PLQY to achieve a maximum value of around 93%. A small decrease of PLQY to 92% is observed for the QDs grown at 190 °C. After storing the QD solutions for 6 months under an air atmosphere, we estimated their corresponding time-resolved PL, which exhibit longer decays as the synthesis temperature increases (see Figure A.3.5) PL decay measurements were performed after this period of time with the purpose of correlating their improved photophysical properties as PLQY of QDs with their long-term stability. The average lifetimes, $\tau_{avg}$, estimated from the PL decays allow the calculation of the corresponding radiative and non-radiative recombination decay rate constants, $K_r$ and $K_{nr}$ (see Table A.3.2 and Figure 4.3.4d). The trend observed in the PLQY (see Figure 4.3.4c) of the as-prepared QDs synthesized at different temperatures is in excellent agreement with the inverse of the $K_{nr}/K_r$ ratio (see Figure 4.3.4e). Note that all the QDs exhibit similar $K_r$, but $K_{nr}$ decreases with the synthesis temperature as it increases from 170 to 185 °C, reporting a minimum at the last temperature and then a slight increase when the temperature rises to 190 °C. Consequently, the shape of the $K_{nr}/K_r$ ratio, and therefore of the PLQY, is influenced by a change in the non-radiative decay rate. As the temperature increases from 170 to 185 °C, the non-radiative recombination channels are reduced, increasing slightly when the temperature varies from 185 °C to 190 °C. We attribute the reduction of the non-radiative recombination channels to the different QD synthesis conditions and to a different effective passivation of the QD surface by OLM, as we discuss below.

For carrying out the QD synthesis at temperatures ≥200 °C, it was necessary to introduce an extra modification to our syn-thetic route. Instead of stabilizing $PbI_2$ at 120 °C, we per-formed the stabilization of the lead precursor at the desired temperature just before the Cs-oleate injection. Under this condition, we minimized the time needed to induce the conversion of OLM to NOA in the mixture reaction. Thus, we were able to synthesize QDs at 210 and 230 °C, with a PLQY and FWHM of ~ 90% and 32 nm, respectively. Even though these photophysical properties show near values to the suitable condition one (185 °C), this procedure requires further optimization. However, we proved once again with this finding that the synthesis and stabilization of $CsPbI_3$ QDs can be guaran-teed by ensuring

the presence of enough content of OLM. In the same line, we concluded that OLM mediates the passivation of defects on the QD surface.[179] Note that, under different synthesis conditions, we modified the QD size and consequently the surface that needs to be passivated (see Table A.3.1) and the amount of available OLM for surface passivation (see Table 4.3.1). With these two parameters it is possible to calculate the available OLM per surface unit, see in Table A.3.1, as the OLM/surface ratio. This ratio follows the same trend as the PLQY, pointing to an increase of the OLM passivating agent as the origin of the PLQY enhancement. It is clear that the reduction of surface defects by ligand passivation is a key point to improve the photophysical features of QDs, similar to the surface treatment performed by postsynthetic protocols.[123, 124] In the same line, very recently, Hao et al.[102] have also reported the most recent performance record of QD solar cells, 16.6%, using perovskite QDs synthesized using an excess of OA.

Beyond the positive effect of the improved QD passivation on the PLQY, this passivation also has a remarkable effect on the long-term stability of $CsPbI_3$ QDs. We tracked the PLQY of perovskite QDs, stored under an air atmosphere in a fridge, after 6 and 15 months (see Figure 4.3.4f). In these periods of time, the PLQY just decreased 3 and 7% of the original value for QDs presenting the highest PLQY, the ones synthesized at 185 °C. This behavior is in good agreement with the $K_{nr}/K_r$ ratio established in Figure 4.3.4e, where the maximum suppression of non-radiative recombination channels was reached. In addition, the reduction of the initial PLQY after 15 months is inversely proportional to the initial PLQY (see Table 4.3.2 and Table A.3.1). This stability is well above the current stability of commercially available $CsPbI_3$ and $CsPbBr_3$, which normally present an expiry date of 3 months. Hence, we conclude that the suitable passivation of surface defects provided by OLM enhances both the PLQY and stability of QDs in a long-term.

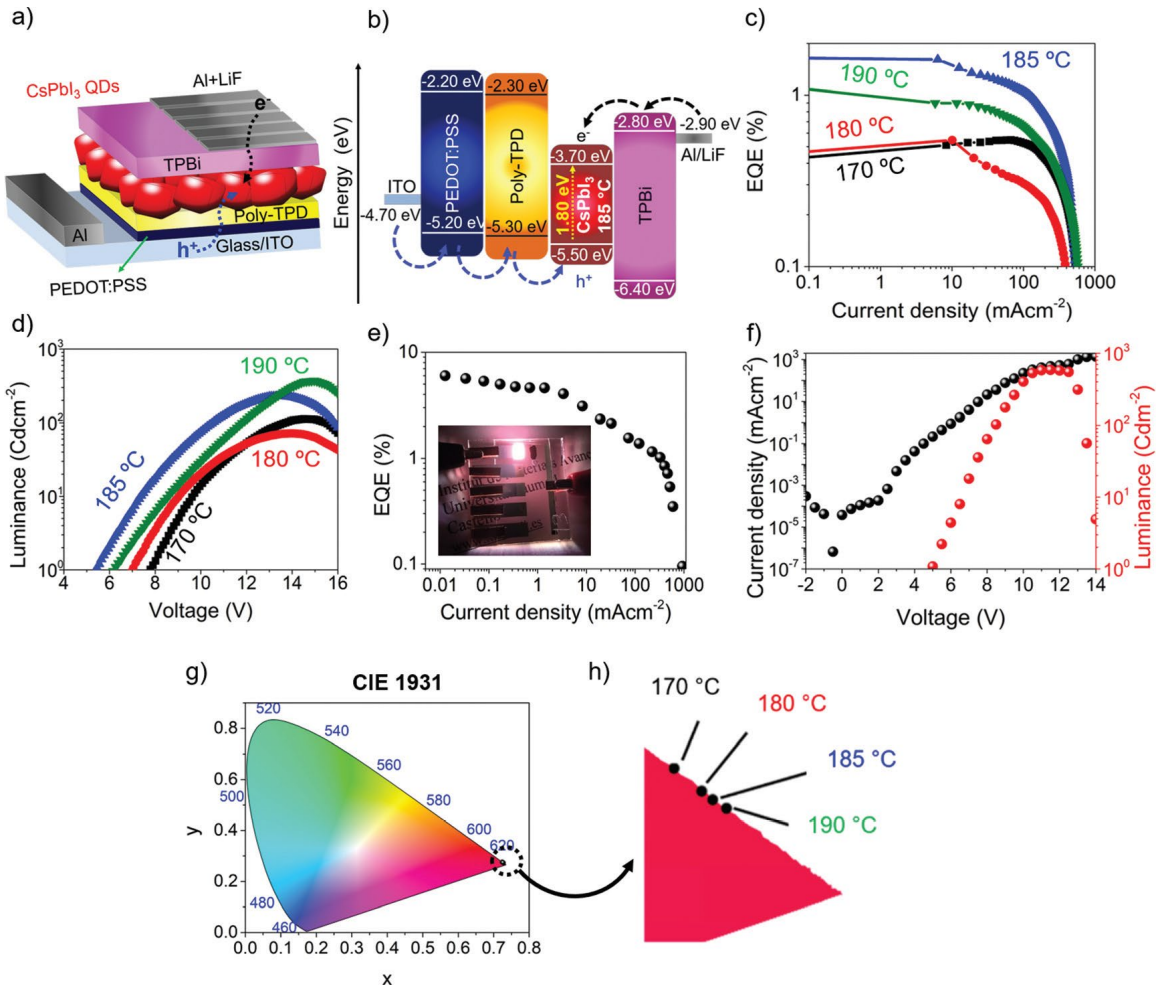


**Figure 4.3.5 (a) Schematic diagram and (b) relative energy band positions of a $CsPbI_3$-LED configuration. Performance characterization of devices: (c) EQE, and (d) luminance of $CsPbI_3$-LED fabricated from different perovskite quantum dots by varying the synthesis temperature. (e) Maximum EQE (f) current/luminance for the champion $CsPbI_3$-LED device using quantum dots synthesized at 185 °C. The inset of Fig. 5e shows the photograph of the $CsPbI_3$-LED device under operation. (g and h) CIE chromaticity at different temperatures.**

The improvement of the photophysical properties of $CsPbI_3$ QDs by using our synthetic route allowed us to explore these materials as light emitters for the fabrication of LEDs. Considering the high PLQY as the main feature of the synthesized QDs, their high performance in LEDs can be favored.[187, 188] Devices were prepared using the likely most extended perovskite LED architecture, ITO/PEDOT:PSS/poly-TPD/$CsPbI_3$/TPBi/LiF/Al (see Figure 4.3.5a and b), [189] which ensures an appropriate electron and hole injection into the perovskite QD active layer.[168] We have fabricated LEDs just varying the active layer, by using $CsPbI_3$ QDs synthesized at different temperatures. In order to ensure the dependence of the LED performance on the

photophysical properties of QDs, avoiding the influence of external factors on device preparation (QD concentration, thickness of active, electron and hole transport layers, etc.), we fabricated multiple LED devices by using the same and different batches of each kind of QD solutions for device optimization. As it is shown in Figure 4.3.5c, we observe that the maximum EQE obtained for the LED QDs presents exactly the same behavior as the $K_{nr}/K_r$ recombination rate ratio by varying the synthesis temperature (Figure 4.3.5e). In this context, we achieved the highest EQE performance with the QDs synthesized at 185 °C, due to the reduction of the non-radiative recombination sites in these QDs. All the devices present a roll-off effect at currents above 100 mA $cm^{-2}$ as it is commonly observed in perovskite LEDs.[190] The luminance (L) was also dependent on the synthesis conditions (Figure 4.3.5d). LEDs presenting the lowest turn-on voltage ($V_{ON}$), 4.8 V, were prepared using QDs synthesized at 185 °C.

Considering the previously reported record performance of non-modified $CsPbI_3$ QDs that present performance values of 2.25–2.5% EQE, L of 400 Cd $m^{-2}$ and $V_{ON}$ of 4.5–6V,[122, 125] our devices present similar values of the LED parameters. However, after contact optimization a champion $CsPbI_3$-LED device showing a maximum EQE value and L value of around 6.02% and 587 Cd $m^{-2}$, respectively, was obtained (see Figure 4.3.5e and f). The maximum current from the champion device was 1381 mA $cm^{-2}$ (Figure 4.3.5f) producing a red light, see the inset of Figure 4.3.5e, with a turn-on voltage of 4.8 V. This optimized device showed better performance than previously reported devices, as for example $Sr^{2+}$-modified $CsPbI_3$ QD LEDs (EQE = 5.92% and $V_{ON}$ = 9.2 V),[122] KBr-passivated $CsPbBr_{3-x}I_x$ QD LEDs (EQE = 3.55% and $V_{ON}$ = 4.6),[191] and relatively close performance to highly flexible $CsPbI_3$ QDs LEDs (EQE = 8.2% and $V_{ON}$ = 2 V).[192] Furthermore, $CsPbI_3$ LEDs fabricated in this study correspond to a deep red color that have the CIE chromaticity coordinates (x,y) beyond the red emission coordinates in accordance with the Rec. 2020 standards for red color (0.708, 0.292)[130] (see Figure 4.3.5g, h and Table A.3.4). Hence, we widely demonstrate that the maximum reduction of non-radiative recombination channels in QDs reached by controlling the synthesis temperature and capping ligand concentration opens the door for the improvement of the optoelectronic properties of perovskites to be competitive in the fabrication of high-performance LEDs with pure color.

# 5. Conclusions

## 5.1. Integrated Optical Amplifier-Photodetector on a Wearable Nanocellulose Substrate

we propose the monolithic integration of a WG amplifier–photodetector system in a flexible nanocellulose substrate for future wearable applications. The device allows an in-situ monitoring of PL signal (in spontaneous and ASE regimes) decoupled at the edge of the waveguide by studying the photocurrent generated by the pump beam generating this PL. For this purpose, we successfully integrated a PMMA/$MAPbI_3$ bilayer structure on the cellulose substrate without any significant degradation of the semiconductor, and inject the excitation light at the input edge of the flexible substrate. As a result, ASE is demonstrated with similar performances as those reported for rigid substrates. Moreover, we demonstrate the simultaneous photodetection of light photogenerating carriers in the MHP film by means of the integrated photoconductor with the WG amplifier. The resulting photo-current demonstrates a clear correlation with the intensity of PL under spontaneous and ASE generation regimes as a function of the laser excitation fluency. Moreover, the different behaviors of the photocurrent in the two regimes will allow a broad range of applications, such as trigger generation, gain automatic control, signal processing for visible telecommunications and sensing. This potentiality has been demonstrated by varying temperature below and above room temperature. Therefore, the present work paves the road for the future integration of wearable photonic components using cellulose substrates.

## 5.2. Operation Mechanism of Perovskite Quantum Dot Solar Cells Probed by Impedance Spectroscopy

we have prepared and characterized PQDSCs with $CsPbI_3$ QDs. The devices with different numbers of QD deposited layers, i.e., different thicknesses, have been prepared and analyzed. Two different working regimes are identified at low and high illumination conditions. At low illumination, recombination is ruled by multiple trapping and trap distributions. However, at higher light intensities, most of these traps are filled, resulting in a Shockley−Read−Hall recombination. PQDSCs present an impedance spectroscopy pattern similar to that of bulk thin-film PSCs. Sufficiently thick layers have to be prepared to reduce recombination, which probably originated in thin layers because of nonuniformities. Interestingly, PQDSCs present the main impedance signature of PSCs, a high $C_{LF}$ under illumination commonly related with ion migration. The similarity of the impedance pattern and the characteristic behavior of $R_{rec}$ and $C_{LF}$ reported in this work strongly points to an analogous working mechanism in both PSCs and PQDSCs. Further

confirmation of this point would indicate that the ionic effect is not just important in bulk perovskite thin films but on the QD layer, influencing decisively the working behavior of PQDSCs. As in the case of PSCs at high illumination, $C_{LF}$ for PQDSCs is independent of the active layer thickness, pointing to a major role of interfacial effects. $C_{LF}$ also presents a complementary slope to the observed $R_{rec}$, also observed in PSCs, pointing to a relationship between ion migration and recombination; however, further research is required to establish properly this relationship. In addition, this work highlights the potential of impedance spectroscopy in the future optimization of this technology.

## 5.3. Ligand & Band Gap Engineering: Tailoring the Protocol Synthesis for Achieving High-Quality $CsPbI_3$ Quantum Dots

By increasing the ligand concentration in the conventional protocol for hot-injection method, we unlocked the synthesis of $CsPbI_3$ QDs with enhanced photophysical properties: higher PLQY, narrower PL FWHM, deep red color (narrower bandgap) and enhanced long-term stability. We elucidated that OA and OLA are fully transformed into OLM during the synthesis, this species being the key factor for enabling the synthesis at higher temperatures and performing an efficient passivation of QD surfaces. $CsPbI_3$ synthesized with a higher amount of OLM per unit surface area of QDs present higher PLQY and long-term QD stability. Enhanced OLM passivation induces a decrease of the non-radiative recombination channels, prolonging the highest material stability for at least 15 months, evidencing only a decrease in the PLQY of around 7% after this period in QDs synthesized at 185 °C. By under-standing the chemistry behind the QD synthesis, we applied these materials for the fabrication of LEDs, reaching an EQE of around 6% and a chromaticity index beyond the Rec. 2020 standards for deep red. The performance of the fabricated LEDs is higher than the previously reported LEDs with the same standard architectures, containing standard capping agents, without additional elements or farther element exchange. Hence, we demonstrate that our synthetic protocol can provide high-quality and ultra-stable $CsPbI_3$ QDs that can be effectively employed in highly efficient optoelectronic devices.

# References

# References


1. Bragg, W.L., *The crystalline state.* 1933.
2. Patterson, A., *The Scherrer formula for X-ray particle size determination.* Physical review, 1939. **56**(10): p. 978.
3. Westphal, V. and S.W. Hell, *Nanoscale resolution in the focal plane of an optical microscope.* Physical review letters, 2005. **94**(14): p. 143903.
4. van Putten, E.G., et al., *Scattering lens resolves sub-100 nm structures with visible light.* Physical review letters, 2011. **106**(19): p. 193905.
5. Cargille, J.J., *Immersion oil and the microscope.* NY Microscop. Soc., Yearbook, 2008. **9**.
6. Hawkes, P.W. and J.C. Spence, *Science of microscopy*. 2008: Springer Science & Business Media.
7. Inkson, B., *Scanning electron microscopy (SEM) and transmission electron microscopy (TEM) for materials characterization*, in *Materials characterization using nondestructive evaluation (NDE) methods*. 2016, Elsevier. p. 17-43.
8. Williams, D.B. and C.B. Carter, *The transmission electron microscope*, in *Transmission electron microscopy*. 1996, Springer. p. 3-17.
9. Granger, R.M., et al., *Instrumental analysis*. 2017: Oxford University Press.
10. Shinde, K.N., et al., *Basic mechanisms of photoluminescence*, in *Phosphate Phosphors for Solid-State Lighting*. 2012, Springer. p. 41-59.
11. Lichtman, J.W. and J.-A. Conchello, *Fluorescence microscopy.* Nature methods, 2005. **2**(12): p. 910-919.
12. Lakowicz, J.R., *Introduction to fluorescence*, in *Principles of fluorescence spectroscopy*. 2006, Springer. p. 1-26.
13. *Generic Methodologies for Nanotechnology: Characterization*, in *Nanoscale Science and Technology*. 2005. p. 56-129.
14. *Photoluminescence in Analysis of Surfaces and Interfaces*, in *Encyclopedia of Analytical Chemistry*.
15. Achermann, M., *Time-resolved photoluminescence spectroscopy*, in *Optical Techniques for Solid-State Materials characterization*, R.P. Prasankumar and A.J. Taylor, Editors. 2011, CRC Press: Boca Raton, FL. p. 443-465.
16. Valeur, B. and M.N. Berberan-Santos, *Time-Resolved Fluorescence Techniques*, in *Molecular Fluorescence Principles and Applications*. 2012, WILEY-VCH Verlag GmbH & Co. KGaA. p. 285-325.
17. Becker, W., *Introduction to Multi-dimensional TCSPC*, in *Advanced Time-Correlated Single Photon Counting Applications*, W. Becker, Editor. 2015, Springer. p. 1-63.
18. Becker, W., *Overview of Photon Counting Techniques*, in *Advanced time-correlated single photon counting techniques*. 2005, Springer. p. 11-25.
19. Wahl, M., *Modern TCSPC electronics: principles and acquisition modes*, in *Advanced Photon Counting Applications, Methods, Instrumentation*, P. Kapusta, M. Wahl, and R. Erdmann, Editors. 2014, Springer. p. 1-21.
20. Fries, F. and S. Reineke, *Statistical treatment of Photoluminescence Quantum Yield Measurements.* Scientific reports, 2019. **9**(1): p. 1-6.
21. Würth, C., et al., *Comparison of methods and achievable uncertainties for the relative and absolute measurement of photoluminescence quantum yields.* Analytical chemistry, 2011. **83**(9): p. 3431-3439.
22. Borchert, H., *Electrical Characterization of Solar Cells*, in *Solar Cells Based on Colloidal Nanocrystals*. 2014, Springer, Cham. p. 139-148.
23. Trifiletti, V. and N. Manfredi, *Dye-Sensitized Solar Cells: Photophysics of Coordination Complex*, in *Emerging Photovoltaic Technologies: Photophysics and Devices*, C.S. Ponseca, Editor. 2019, Jenny Stanford Publishing: Boca Raton. p. 121-165.

24. Smith, W.A., *Photoelectrochemical cell design, efficiency, definitions, standards, and protocols*, in *Photoelectrochemical Solar Fuel Production*. 2016, Springer. p. 163-197.
25. Kirchartz, T., K. Ding, and U. Rau, *Fundamental Electrical Characterization of Thin-Film Solar Cells*, in *Advanced Characterization Techniques for Thin Film Solar Cells*. 2016. p. 41-69.
26. Anaya, M., et al., *Best practices for measuring emerging light-emitting diode technologies.* Nature Photonics, 2019. **13**(12): p. 818-821.
27. Yuan, M., et al., *Perovskite energy funnels for efficient light-emitting diodes.* Nature nanotechnology, 2016. **11**(10): p. 872-877.
28. Zarazua, I., et al., *Surface Recombination and Collection Efficiency in Perovskite Solar Cells from Impedance Analysis.* Journal of Physical Chemistry Letters, 2016. **7**(24): p. 5105-5113.
29. Guerrero, A., et al., *Properties of Contact and Bulk Impedances in Hybrid Lead Halide Perovskite Solar Cells Including Inductive Loop Elements.* Journal of Physical Chemistry C, 2016. **120**(15): p. 8023-8032.
30. Haranath, D., V. Shanker, and D. Vij, *Electroluminescence: an introduction*, in *Handbook of Electroluminescent Materials*, D. Vij, Editor. 2004. p. 1-23.
31. Robinson, J.W., et al., *Magnetic Resonance Spectroscopy*, in *Undergraduate instrumental analysis*. 2014, CRC Press. p. 113-242.
32. Zerbe, O. and S. Jurt, *Basics of 1D NMR Spectroscopy*, in *Applied NMR spectroscopy for chemists and life scientists*. 2014, John Wiley & Sons. p. 13-31.
33. Rogers, J.A., T. Someya, and Y. Huang, *Materials and Mechanics for Stretchable Electronics.* Science, 2010. **327**(5973): p. 1603-1607.
34. Crawford, M., *Wearable technology is booming, powered by photonics.* SPIE Newsroom, 2016.
35. Hu, J., et al., *Flexible integrated photonics: where materials, mechanics and optics meet Invited.* Optical Materials Express, 2013. **3**(9): p. 1313-1331.
36. Park, S.-I., et al., *Printed Assemblies of Inorganic Light-Emitting Diodes for Deformable and Semitransparent Displays.* Science, 2009. **325**(5943): p. 977-981.
37. Bosman, E., et al., *Highly Reliable Flexible Active Optical Links.* Ieee Photonics Technology Letters, 2010. **22**(5): p. 287-289.
38. Chen, Y., H. Li, and M. Li, *Flexible and tunable silicon photonic circuits on plastic substrates.* Scientific Reports, 2012. **2**.
39. Shih, M.H., et al., *Compact optical curvature sensor with a flexible microdisk laser on a polymer substrate.* Optics Letters, 2009. **34**(18): p. 2733-2735.
40. Shirer, M., R. Llamas, and J. Ubrani, *IDC Forecasts Wearables Shipments to Reach 213.6 Million Units Worldwide in 2020 with Watches and Wristbands Driving Volume While Clothing and Eyewear Gain Traction*. 2016.
41. Saule Technologies. [cited 2018 March]; Available from: http://sauletech.com/.
42. Dong, Q., et al., *Electron-hole diffusion lengths >175 μm in solution-grown $CH_3NH_3PbI_3$ single crystals.* Science, 2015. **347**(6225): p. 967-970.
43. De Wolf, S., et al., *Organometallic Halide Perovskites: Sharp Optical Absorption Edge and Its Relation to Photovoltaic Performance.* Journal of Physical Chemistry Letters, 2014. **5**(6): p. 1035-1039.
44. Xing, G., et al., *Low-temperature solution-processed wavelength-tunable perovskites for lasing.* Nature Materials, 2014. **13**(5): p. 476-480.
45. Zhu, H., et al., *Lead halide perovskite nanowire lasers with low lasing thresholds and high quality factors.* Nature Materials, 2015. **14**(6): p. 636-U115.
46. Laboratory, N.R.E., *Best Research-Cell Efficiency Chart*. 2019, NREL Golden, CO.
47. Suarez, I., et al., *Polymer/Perovskite Amplifying Waveguides for Active Hybrid Silicon Photonics.* Advanced Materials, 2015. **27**(40): p. 6157-6162.

48. Thi Tuyen, N., et al., *Enhancement of the Performance of Perovskite Solar Cells, LEDs, and Optical Amplifiers by Anti-Solvent Additive Deposition.* Advanced Materials, 2017. **29**(7).
49. Lin, Q., et al., *Filterless narrowband visible photodetectors.* Nature Photonics, 2015. **9**(10): p. 687-+.
50. Fang, Y., et al., *Highly narrowband perovskite single-crystal photodetectors enabled by surface-charge recombination.* Nature Photonics, 2015. **9**(10): p. 679-+.
51. Di Giacomo, F., et al., *Progress, challenges and perspectives in flexible perovskite solar cells.* Energy & Environmental Science, 2016. **9**(10): p. 3007-3035.
52. Kaltenbrunner, M., et al., *Flexible high power-per-weight perovskite solar cells with chromium oxide-metal contacts for improved stability in air.* Nature Materials, 2015. **14**(10): p. 1032-+.
53. Cong, L., et al., *Perovskite as a Platform for Active Flexible Metaphotonic Devices.* Acs Photonics, 2017. **4**(7): p. 1595-1601.
54. Stranks, S.D., et al., *Enhanced Amplified Spontaneous Emission in Perovskites Using a Flexible Cholesteric Liquid Crystal Reflector.* Nano Letters, 2015. **15**(8): p. 4935-4941.
55. Klemm, D., et al., *Nanocelluloses: A New Family of Nature-Based Materials.* Angewandte Chemie-International Edition, 2011. **50**(24): p. 5438-5466.
56. Dufresne, A., *Nanocellulose: a new ageless bionanomaterial.* Materials Today, 2013. **16**(6): p. 220-227.
57. Abitbol, T., et al., *Nanocellulose, a tiny fiber with huge applications.* Current Opinion in Biotechnology, 2016. **39**: p. 76-88.
58. Bettotti, P., et al., *Dynamics of Hydration of Nanocellulose Films.* Advanced Materials Interfaces, 2016. **3**(5).
59. Wu, W., et al., *Nanocellulose-based Translucent Diffuser for Optoelectronic Device Applications with Dramatic Improvement of Light Coupling.* Acs Applied Materials & Interfaces, 2015. **7**(48): p. 26860-26864.
60. Guidetti, G., et al., *Flexible Photonic Cellulose Nanocrystal Films.* Advanced Materials, 2016. **28**(45): p. 10042-10047.
61. Roilo, D., et al., *Cellulose Nanofibrils Films: Molecular Diffusion through Elongated Sub-Nano Cavities.* Journal of Physical Chemistry C, 2017. **121**(28): p. 15437-15447.
62. Yang, Y., et al., *Recent progress in flexible and wearable bio-electronics based on nanomaterials.* Nano Research, 2017. **10**(5): p. 1560-1583.
63. Jung, M.-H., N.-M. Park, and S.-Y. Lee, *Color tunable nanopaper solar cells using hybrid $CH_3NH_3PbI_{3-x}Br_x$ perovskite.* Solar Energy, 2016. **139**: p. 458-466.
64. Castro-Hermosa, S., et al., *Perovskite Solar Cells on Paper and the Role of Substrates and Electrodes on Performance.* Ieee Electron Device Letters, 2017. **38**(9): p. 1278-1281.
65. Bella, F., et al., *Improving efficiency and stability of perovskite solar cells with photocurable fluoropolymers.* Science, 2016. **354**(6309): p. 203-206.
66. Yang, W.S., et al., *Iodide management in formamidinium-lead-halide-based perovskite layers for efficient solar cells.* Science, 2017. **356**(6345): p. 1376-+.
67. Saliba, M., et al., *Cesium-containing triple cation perovskite solar cells: improved stability, reproducibility and high efficiency.* Energy & Environmental Science, 2016. **9**(6): p. 1989-1997.
68. Christians, J.A., et al., *Stability in Perovskite Photovoltaics: A Paradigm for Newfangled Technologies.* Acs Energy Letters, 2018. **3**(9): p. 2136-2143.
69. Conings, B., et al., *Intrinsic Thermal Instability of Methylammonium Lead Trihalide Perovskite.* Advanced Energy Materials, 2015. **5**(15).
70. Sutton, R.J., et al., *Bandgap-Tunable Cesium Lead Halide Perovskites with High Thermal Stability for Efficient Solar Cells.* Advanced Energy Materials, 2016. **6**(8).

71. Kulbak, M., et al., *Cesium Enhances Long-Term Stability of Lead Bromide Perovskite-Based Solar Cells.* Journal of Physical Chemistry Letters, 2016. **7**(1): p. 167-172.
72. Suarez, B., et al., *Recombination Study of Combined Halides (Cl, Br, I) Perovskite Solar Cells.* Journal of Physical Chemistry Letters, 2014. **5**(10): p. 1628-1635.
73. Noh, J.H., et al., *Chemical Management for Colorful, Efficient, and Stable Inorganic-Organic Hybrid Nanostructured Solar Cells.* Nano Letters, 2013. **13**(4): p. 1764-1769.
74. Eperon, G.E., et al., *Inorganic caesium lead iodide perovskite solar cells.* Journal of Materials Chemistry A, 2015. **3**(39): p. 19688-19695.
75. Eperon, G.E., et al., *Formamidinium lead trihalide: a broadly tunable perovskite for efficient planar heterojunction solar cells.* Energy & Environmental Science, 2014. **7**(3): p. 982-988.
76. Sharma, S., N. Weiden, and A. Weiss, *PHASE-DIAGRAMS OF QUASI-BINARY SYSTEMS OF THE TYPE - $ABX_3$-$A'BX_3$ $ABX_3$-$AB'X_3$, AND $ABX_3$-$ABX'_3$ X = HALOGEN.* Zeitschrift Fur Physikalische Chemie-International Journal of Research in Physical Chemistry & Chemical Physics, 1992. **175**: p. 63-80.
77. Alivisatos, A.P., *Semiconductor clusters, nanocrystals, and quantum dots.* Science, 1996. **271**(5251): p. 933-937.
78. Kovalenko, M.V., et al., *Prospects of Nanoscience with Nanocrystals.* Acs Nano, 2015. **9**(2): p. 1012-1057.
79. Owens, J. and L. Brus, *Chemical Synthesis and Luminescence Applications of Colloidal Semiconductor Quantum Dots.* Journal of the American Chemical Society, 2017. **139**(32): p. 10939-10943.
80. Schmidt, L.C., et al., *Nontemplate Synthesis of $CH_3NH_3PbBr_3$ Perovskite Nanoparticles.* Journal of the American Chemical Society, 2014. **136**(3): p. 850-853.
81. Protesescu, L., et al., *Nanocrystals of Cesium Lead Halide Perovskites ($CsPbX_3$, X = Cl, Br, and I): Novel Optoelectronic Materials Showing Bright Emission with Wide Color Gamut.* Nano Letters, 2015. **15**(6): p. 3692-3696.
82. Kovalenko, M.V., L. Protesescu, and M.I. Bodnarchuk, *Properties and potential optoelectronic applications of lead halide perovskite nanocrystals.* Science, 2017. **358**(6364): p. 745-750.
83. Huang, H., et al., *Lead Halide Perovskite Nanocrystals in the Research Spotlight: Stability and Defect Tolerance.* Acs Energy Letters, 2017. **2**(9): p. 2071-2083.
84. Sanehira, E.M., et al., *Enhanced mobility $CsPbI_3$ quantum dot arrays for record-efficiency, high-voltage photovoltaic cells.* Science Advances, 2017. **3**(10).
85. Ghosh, D., et al., *Dependence of halide composition on the stability of highly efficient all-inorganic cesium lead halide perovskite quantum dot solar cells.* Solar Energy Materials and Solar Cells, 2018. **185**: p. 28-35.
86. Liu, F., et al., *Ultrafast Electron Injection from Photoexcited Perovskite $CsPbI_3$ QDs into $TiO_2$ Nanoparticles with Injection Efficiency near 99%.* Journal of Physical Chemistry Letters, 2018. **9**(2): p. 294-297.
87. Draguta, S., et al., *Rationalizing the light-induced phase separation of mixed halide organic-inorganic perovskites.* Nature Communications, 2017. **8**.
88. Hoke, E.T., et al., *Reversible photo-induced trap formation in mixed-halide hybrid perovskites for photovoltaics.* Chemical Science, 2015. **6**(1): p. 613-617.
89. Fabian Gualdron-Reyes, A., S. Joon Yoon, and I. Mora-Sero, *Recent insights for achieving mixed halide perovskites without halide segregation.* Current Opinion in Electrochemistry, 2018. **11**: p. 84-90.
90. Yang, T.C.-J., et al., *High-Bandgap Perovskite Materials for Multijunction Solar Cells.* Joule, 2018. **2**(8): p. 1421-1436.

91. Wheeler, L.M., et al., *Targeted Ligand-Exchange Chemistry on Cesium Lead Halide Perovskite Quantum Dots for High-Efficiency Photovoltaics.* Journal of the American Chemical Society, 2018. **140**(33): p. 10504-10513.
92. Hazarika, A., et al., *Perovskite Quantum Dot Photovoltaic Materials beyond the Reach of Thin Films: Full-Range Tuning of A-Site Cation Composition.* Acs Nano, 2018. **12**(10): p. 10327-10337.
93. Yuan, J., et al., *Band-Aligned Polymeric Hole Transport Materials for Extremely Low Energy Loss α-$CsPbI_3$ Perovskite Nanocrystal Solar Cells.* Joule, 2018. **2**(11): p. 2450-2463.
94. Fabregat-Santiago, F., et al., *Characterization of nanostructured hybrid and organic solar cells by impedance spectroscopy.* Physical Chemistry Chemical Physics, 2011. **13**(20): p. 9083-9118.
95. Zhou, Q., et al., *In Situ Fabrication of Halide Perovskite Nanocrystal-Embedded Polymer Composite Films with Enhanced Photoluminescence for Display Backlights.* Advanced Materials, 2016. **28**(41): p. 9163-+.
96. Xu, Y., et al., *Two-Photon-Pumped Perovskite Semiconductor Nanocrystal Lasers.* Journal of the American Chemical Society, 2016. **138**(11): p. 3761-3768.
97. Navarro-Arenas, J., et al., *Single-Exciton Amplified Spontaneous Emission in Thin Films of $CsPbX_3$ (X = Br, I) Perovskite Nanocrystals.* Journal of Physical Chemistry Letters, 2019. **10**(20): p. 6389-6398.
98. Tan, Z.-K., et al., *Bright light-emitting diodes based on organometal halide perovskite.* Nature Nanotechnology, 2014. **9**(9): p. 687-692.
99. Dou, L., et al., *Solution-processed hybrid perovskite photodetectors with high detectivity.* Nature Communications, 2014. **5**.
100. Zolfaghari, Z., et al., *Operation Mechanism of Perovskite Quantum Dot Solar Cells Probed by Impedance Spectroscopy.* Acs Energy Letters, 2019. **4**(1): p. 251-258.
101. Li, F., et al., *Perovskite Quantum Dot Solar Cells with 15.6% Efficiency and Improved Stability Enabled by an α-$CsPbI_3$/$FAPbI_3$ Bilayer Structure.* Acs Energy Letters, 2019. **4**(11): p. 2571-+.
102. Hao, M., et al., *Ligand-assisted cation-exchange engineering for high-efficiency colloidal $Cs_{1-x}FA_xPbI_3$ quantum dot solar cells with reduced phase segregation.* Nature Energy, 2020. **5**(1): p. 79-88.
103. Masi, S., A.F. Gualdron-Reyes, and I. Mora-Sero, *Stabilization of Black Perovskite Phase in $FAPbI_3$ and $CsPbI_3$.* Acs Energy Letters, 2020. **5**(6): p. 1974-1985.
104. Fu, Y., et al., *Broad Wavelength Tunable Robust Lasing from Single-Crystal Nanowires of Cesium Lead Halide Perovskites ($CsPbX_3$, X = Cl, Br, I).* Acs Nano, 2016. **10**(8): p. 7963-7972.
105. Liu, F., et al., *Highly Luminescent Phase-Stable $CsPbI_3$ Perovskite Quantum Dots Achieving Near 100% Absolute Photoluminescence Quantum Yield.* Acs Nano, 2017. **11**(10): p. 10373-10383.
106. Shi, D., et al., *Low trap-state density and long carrier diffusion in organolead trihalide perovskite single crystals.* Science, 2015. **347**(6221): p. 519-522.
107. Diab, H., et al., *Narrow Linewidth Excitonic Emission in Organic-Inorganic Lead Iodide Perovskite Single Crystals.* Journal of Physical Chemistry Letters, 2016. **7**(24): p. 5093-5100.
108. Nedelcu, G., et al., *Fast Anion-Exchange in Highly Luminescent Nanocrystals of Cesium Lead Halide Perovskites ($CsPbX_3$, X = Cl, Br, I).* Nano Letters, 2015. **15**(8): p. 5635-5640.
109. Quyet Van, L., et al., *Structural Investigation of Cesium Lead Halide Perovskites for High-Efficiency Quantum Dot Light-Emitting Diodes.* Journal of Physical Chemistry Letters, 2017. **8**(17): p. 4140-4147.
110. Gan, J., et al., *α-$CsPbI_3$ Colloidal Quantum Dots: Synthesis, Photodynamics, and Photovoltaic Applications.* Acs Energy Letters, 2019. **4**(6): p. 1308-1320.
111. Chiba, T., et al., *Anion-exchange red perovskite quantum dots with ammonium iodine salts for highly efficient light-emitting devices.* Nature Photonics, 2018. **12**(11): p. 681-+.

112. Pradhan, N., *Journey of Making Cesium Lead Halide Perovskite Nanocrystals: What's Next.* Journal of Physical Chemistry Letters, 2019. **10**(19): p. 5847-5855.
113. Swarnkar, A., et al., *Quantum dot-induced phase stabilization of α-$CsPbI_3$ perovskite for high-efficiency photovoltaics.* Science, 2016. **354**(6308): p. 92-95.
114. Almeida, G., et al., *Role of Acid-Base Equilibria in the Size, Shape, and Phase Control of Cesium Lead Bromide Nanocrystals.* Acs Nano, 2018. **12**(2): p. 1704-+.
115. Naghadeh, S.B., et al., *Size Dependence of Charge Carrier Dynamics in Organometal Halide Perovskite Nanocrystals: Deciphering Radiative Versus Nonradiative Components.* Journal of Physical Chemistry C, 2019. **123**(7): p. 4610-4619.
116. Lu, M., et al., *Spontaneous Silver Doping and Surface Passivation of $CsPbI_3$ Perovskite Active Layer Enable Light-Emitting Devices with an External Quantum Efficiency of 11.2%.* Acs Energy Letters, 2018. **3**(7): p. 1571-1577.
117. Nayak, P.K., et al., *Impact of $Bi^{3+}$ Heterovalent Doping in Organic-Inorganic Metal Halide Perovskite Crystals.* Journal of the American Chemical Society, 2018. **140**(2): p. 574-577.
118. van der Stam, W., et al., *Highly Emissive Divalent-Ion-Doped Colloidal $CsPb_{1-x}M_xBr_3$ Perovskite Nanocrystals through Cation Exchange.* Journal of the American Chemical Society, 2017. **139**(11): p. 4087-4097.
119. Liu, W., et al., *$Mn^{2+}$-Doped Lead Halide Perovskite Nanocrystals with Dual-Color Emission Controlled by Halide Content.* Journal of the American Chemical Society, 2016. **138**(45): p. 14954-14961.
120. Zhu, J., et al., *Room-Temperature Synthesis of Mn-Doped Cesium Lead Halide Quantum Dots with High Mn Substitution Ratio.* Journal of Physical Chemistry Letters, 2017. **8**(17): p. 4167-4171.
121. Lu, M., et al., *Simultaneous Strontium Doping and Chlorine Surface Passivation Improve Luminescence Intensity and Stability of $CsPbI_3$ Nanocrystals Enabling Efficient Light-Emitting Devices.* Advanced Materials, 2018. **30**(50).
122. Yao, J.-S., et al., *Few-Nanometer-Sized α-$CsPbI_3$ Quantum Dots Enabled by Strontium Substitution and Iodide Passivation for Efficient Red-Light Emitting Diodes.* Journal of the American Chemical Society, 2019. **141**(5): p. 2069-2079.
123. Liu, Y., et al., *Synergetic Effect of Postsynthetic Water Treatment on the Enhanced Photoluminescence and Stability of $CsPbX_3$ (X = Cl, Br, I) Perovskite Nanocrystals.* Chemistry of Materials, 2018. **30**(19): p. 6922-6929.
124. Li, F., et al., *Postsynthetic Surface Trap Removal of $CsPbX_3$ (X = Cl, Br, or I) Quantum Dots via a $ZnX_2$/Hexane Solution toward an Enhanced Luminescence Quantum Yield.* Chemistry of Materials, 2018. **30**(23): p. 8546-8554.
125. Pan, J., et al., *Bidentate Ligand-Passivated $CsPbI_3$ Perovskite Nanocrystals for Stable Near-Unity Photoluminescence Quantum Yield and Efficient Red Light-Emitting Diodes.* Journal of the American Chemical Society, 2018. **140**(2): p. 562-565.
126. Yuan, S., et al., *Self-Assembled High Quality $CsPbBr_3$ Quantum Dot Films toward Highly Efficient Light-Emitting Diodes.* Acs Nano, 2018. **12**(9): p. 9541-9548.
127. Chen, Y., et al., *Surface Termination of $CsPbBr_3$ Perovskite Quantum Dots Determined by Solid-State NMR Spectroscopy.* Journal of the American Chemical Society, 2020. **142**(13): p. 6117-6127.
128. Shen, X., et al., *Zn-Alloyed $CsPbI_3$ Nanocrystals for Highly Efficient Perovskite Light-Emitting Devices.* Nano Letters, 2019. **19**(3): p. 1552-1559.
129. Ravi, V.K., et al., *Origin of the Substitution Mechanism for the Binding of Organic Ligands on the Surface of $CsPbBr_3$ Perovskite Nanocubes.* Journal of Physical Chemistry Letters, 2017. **8**(20): p. 4988-4994.

130. Zhu, R., et al., *Realizing Rec. 2020 color gamut with quantum dot displays.* Optics Express, 2015. **23**(18): p. 23680-23693.
131. Pitarch-Tena, D., et al., *Impedance Spectroscopy Measurements in Perovskite Solar Cells: Device Stability and Noise Reduction.* Acs Energy Letters, 2018. **3**(4): p. 1044-1048.
132. Saito, T., et al., *Cellulose nanofibers prepared by TEMPO-mediated oxidation of native cellulose.* Biomacromolecules, 2007. **8**(8): p. 2485-2491.
133. Pourdavoud, N., et al., *Photonic Nanostructures Patterned by Thermal Nanoimprint Directly into Organo- Metal Halide Perovskites.* Advanced Materials, 2017. **29**(12).
134. Deschler, F., et al., *High Photoluminescence Efficiency and Optically Pumped Lasing in Solution-Processed Mixed Halide Perovskite Semiconductors.* Journal of Physical Chemistry Letters, 2014. **5**(8): p. 1421-1426.
135. Draguta, S., et al., *Spatially Non-uniform Trap State Densities in Solution-Processed Hybrid Perovskite Thin Films.* Journal of Physical Chemistry Letters, 2016. **7**(4): p. 715-721.
136. Sutherland, B.R. and E.H. Sargent, *Perovskite photonic sources.* Nature Photonics, 2016. **10**(5): p. 295-302.
137. Suarez Alvarez, I., *Active photonic devices based on colloidal semiconductor nanocrystals and organometallic halide perovskites.* European Physical Journal-Applied Physics, 2016. **75**(3).
138. Diaz, J.A., et al., *Thermal Conductivity in Nanostructured Films: From Single Cellulose Nanocrystals to Bulk Films.* Biomacromolecules, 2014. **15**(11): p. 4096-4101.
139. Juarez-Perez, E.J., et al., *Photoinduced Giant Dielectric Constant in Lead Halide Perovskite Solar Cells.* Journal of Physical Chemistry Letters, 2014. **5**(13): p. 2390-2394.
140. Jaffe, A., et al., *High-Pressure Single-Crystal Structures of 3D Lead-Halide Hybrid Perovskites and Pressure Effects on their Electronic and Optical Properties.* Acs Central Science, 2016. **2**(4): p. 201-209.
141. Motta, C., F. El-Mellouhi, and S. Sanvito, *Charge carrier mobility in hybrid halide perovskites.* Scientific Reports, 2015. **5**.
142. Khenkin, M.V., et al., *Temperature and spectral dependence of $CH_3NH_3PbI_3$ films photoconductivity.* Applied Physics Letters, 2017. **110**(22).
143. McDonald, S.A., et al., *Solution-processed PbS quantum dot infrared photodetectors and photovoltaics.* Nature Materials, 2005. **4**(2): p. 138-142.
144. Gao, J., *Semiconductor Laser and Modulator Driver Circuit Design*, in *Optoelectronic Integrated Circuit Design and Device Modeling*. 2010, Wiley. p. 187-232.
145. Gualdron-Reyes, A.F., et al., *Controlling the Phase Segregation in Mixed Halide Perovskites through Nanocrystal Size.* Acs Energy Letters, 2019. **4**(1): p. 54-62.
146. Fakharuddin, A., et al., *Interfaces in Perovskite Solar Cells.* Advanced Energy Materials, 2017. **7**(22).
147. Juarez-Perez, E.J., et al., *Role of the Selective Contacts in the Performance of Lead Halide Perovskite Solar Cells.* Journal of Physical Chemistry Letters, 2014. **5**(4): p. 680-685.
148. Tress, W., et al., *Interpretation and evolution of open-circuit voltage, recombination, ideality factor and subgap defect states during reversible light-soaking and irreversible degradation of perovskite solar cells.* Energy & Environmental Science, 2018. **11**(1): p. 151-165.
149. Contreras-Bernal, L., et al., *Origin and Whereabouts of Recombination in Perovskite Solar Cells.* Journal of Physical Chemistry C, 2017. **121**(18): p. 9705-9713.
150. Dualeh, A., et al., *Impedance Spectroscopic Analysis of Lead Iodide Perovskite-Sensitized Solid-State Solar Cells.* Acs Nano, 2014. **8**(1): p. 362-373.
151. Pascoe, A.R., et al., *Insights into Planar $CH_3NH_3PbI_3$ Perovskite Solar Cells Using Impedance Spectroscopy.* Journal of Physical Chemistry C, 2015. **119**(9): p. 4444-4453.

152. Pockett, A., et al., *Characterization of Planar Lead Halide Perovskite Solar Cells by Impedance Spectroscopy, Open-Circuit Photovoltage Decay, and Intensity-Modulated Photovoltage/Photocurrent Spectroscopy.* Journal of Physical Chemistry C, 2015. **119**(7): p. 3456-3465.
153. Zarazua, I., et al., *Operating Mechanisms of Mesoscopic Perovskite Solar Cells through Impedance Spectroscopy and J-V Modeling.* Journal of Physical Chemistry Letters, 2017. **8**(24): p. 6073-6079.
154. Ansari-Rad, M., Y. Abdi, and E. Arzi, *Reaction Order and Ideality Factor in Dye-Sensitized Nanocrystalline Solar Cells: A Theoretical Investigation.* Journal of Physical Chemistry C, 2012. **116**(20): p. 10867-10872.
155. Fabregat-Santiago, F., et al., *Electron Transport and Recombination in Solid-State Dye Solar Cell with Spiro-OMeTAD as Hole Conductor.* Journal of the American Chemical Society, 2009. **131**(2): p. 558-562.
156. Zarazua, I., J. Bisquert, and G. Garcia-Belmonte, *Light-Induced Space-Charge Accumulation Zone as Photovoltaic Mechanism in Perovskite Solar Cells.* Journal of Physical Chemistry Letters, 2016. **7**(3): p. 525-528.
157. Bag, M., et al., *Kinetics of Ion Transport in Perovskite Active Layers and Its Implications for Active Layer Stability.* Journal of the American Chemical Society, 2015. **137**(40): p. 13130-13137.
158. Moia, D., et al., *Ionic-to-electronic current amplification in hybrid perovskite solar cells: ionically gated transistor-interface circuit model explains hysteresis and impedance of mixed conducting devices.* Energy & Environmental Science, 2019. **12**(4): p. 1296-1308.
159. Jacobs, D.A., et al., *The two faces of capacitance: New interpretations for electrical impedance measurements of perovskite solar cells and their relation to hysteresis.* Journal of Applied Physics, 2018. **124**(22).
160. Kim, H.-S., et al., *Control of I-V Hysteresis in $CH_3NH_3PbI_3$ Perovskite Solar Cell.* Journal of Physical Chemistry Letters, 2015. **6**(22): p. 4633-4639.
161. Snaith, H.J., et al., *Anomalous Hysteresis in Perovskite Solar Cells.* Journal of Physical Chemistry Letters, 2014. **5**(9): p. 1511-1515.
162. Tress, W., et al., *Understanding the rate-dependent J-V hysteresis, slow time component, and aging in $CH_3NH_3PbI_3$ perovskite solar cells: the role of a compensated electric field.* Energy & Environmental Science, 2015. **8**(3): p. 995-1004.
163. Anaya, M., et al., *Electron injection and scaffold effects in perovskite solar cells.* Journal of Materials Chemistry C, 2017. **5**(3): p. 634-644.
164. Contreras, L., et al., *Specific cation interactions as the cause of slow dynamics and hysteresis in dye and perovskite solar cells: a small-perturbation study.* Physical Chemistry Chemical Physics, 2016. **18**(45): p. 31033-31042.
165. Meggiolaro, D., et al., *Iodine chemistry determines the defect tolerance of lead-halide perovskites.* Energy & Environmental Science, 2018. **11**(3): p. 702-713.
166. Bisquert, J., et al., *Electron Lifetime in Dye-Sensitized Solar Cells: Theory and Interpretation of Measurements.* Journal of Physical Chemistry C, 2009. **113**(40): p. 17278-17290.
167. Sanchez, R.S., et al., *Slow Dynamic Processes in Lead Halide Perovskite Solar Cells. Characteristic Times and Hysteresis.* Journal of Physical Chemistry Letters, 2014. **5**(13): p. 2357-2363.
168. Krieg, F., et al., *Colloidal $CsPbX_3$ (X = CI, Br, I) Nanocrystals 2.0: Zwitterionic Capping Ligands for Improved Durability and Stability.* Acs Energy Letters, 2018. **3**(3): p. 641-646.
169. Rayi, V.K., et al., *Hierarchical Arrays of Cesium Lead Halide Perovskite Nanocrystals through Electrophoretic Deposition.* Journal of the American Chemical Society, 2018. **140**(28): p. 8887-8894.

170. Ravi, V.K., et al., *To Exchange or Not to Exchange. Suppressing Anion Exchange in Cesium Lead Halide Perovskites with $PbSO_4$-Oleate Capping.* Acs Energy Letters, 2018. **3**(4): p. 1049-1055.
171. Huang, H., et al., *Growth mechanism of strongly emitting $CH_3NH_3PbBr_3$ perovskite nanocrystals with a tunable bandgap.* Nature Communications, 2017. **8**.
172. Cara, C., et al., *Dialkylamide as Both Capping Agent and Surfactant in a Direct Solvothermal Synthesis of Magnetite and Titania Nanoparticles.* Crystal Growth & Design, 2015. **15**(5): p. 2364-2372.
173. Grisorio, R., et al., *Exploring the surface chemistry of cesium lead halide perovskite nanocrystals.* Nanoscale, 2019. **11**(3): p. 986-999.
174. Liu, Z., et al., *Ligand Mediated Transformation of Cesium Lead Bromide Perovskite Nanocrystals to Lead Depleted $Cs_4PbBr_6$ Nanocrystals.* Journal of the American Chemical Society, 2017. **139**(15): p. 5309-5312.
175. Pan, A., et al., *Insight into the Ligand-Mediated Synthesis of Colloidal $CsPbBr_3$ Perovskite Nanocrystals: The Role of Organic Acid, Base, and Cesium Precursors.* Acs Nano, 2016. **10**(8): p. 7943-7954.
176. De Roo, J., et al., *Highly Dynamic Ligand Binding and Light Absorption Coefficient of Cesium Lead Bromide Perovskite Nanocrystals.* Acs Nano, 2016. **10**(2): p. 2071-2081.
177. Dutta, A., et al., *Phase-Stable $CsPbI_3$ Nanocrystals: The Reaction Temperature Matters.* Angewandte Chemie-International Edition, 2018. **57**(29): p. 9083-9087.
178. Grisorio, R., et al., *Insights into the role of the lead/surfactant ratio in the formation and passivation of cesium lead bromide perovskite nanocrystals.* Nanoscale, 2020. **12**(2): p. 623-637.
179. Bodnarchuk, M.I., et al., *Rationalizing and Controlling the Surface Structure and Electronic Passivation of Cesium Lead Halide Nanocrystals.* Acs Energy Letters, 2019. **4**(1): p. 63-74.
180. Gualdron-Reyes, A.F., et al., *Unravelling the Photocatalytic Behavior of All-Inorganic Mixed Halide Perovskites: The Role of Surface Chemical States.* Acs Applied Materials & Interfaces, 2020. **12**(1): p. 914-924.
181. Koolyk, M., et al., *Kinetics of cesium lead halide perovskite nanoparticle growth; focusing and de-focusing of size distribution.* Nanoscale, 2016. **8**(12): p. 6403-6409.
182. Zhao, Q., et al., *Size-Dependent Lattice Structure and Confinement Properties in $CsPbI_3$ Perovskite Nanocrystals: Negative Surface Energy for Stabilization.* Acs Energy Letters, 2020. **5**(1): p. 238-247.
183. Cademartiri, L., et al., *Multigram scale, solventless, and diffusion-controlled route to highly monodisperse PbS nanocrystals.* Journal of Physical Chemistry B, 2006. **110**(2): p. 671-673.
184. Talapin, D.V., et al., *Evolution of an ensemble of nanoparticles in a colloidal solution: Theoretical study.* Journal of Physical Chemistry B, 2001. **105**(49): p. 12278-12285.
185. Chen, M., et al., *Solvothermal Synthesis of High-Quality All-Inorganic Cesium Lead Halide Perovskite Nanocrystals: From Nanocube to Ultrathin Nanowire.* Advanced Functional Materials, 2017. **27**(23).
186. Protesescu, L., et al., *Dismantling the "Red Wall" of Colloidal Perovskites: Highly Luminescent Formamidinium and Formamidinium-Cesium Lead Iodide Nanocrystals.* Acs Nano, 2017. **11**(3): p. 3119-3134.
187. Wang, H., et al., *Trifluoroacetate induced small-grained $CsPbBr_3$ perovskite films result in efficient and stable light-emitting devices.* Nature Communications, 2019. **10**.
188. Liu, Y., et al., *Suppression of non-radiative recombination toward high efficiency perovskite light-emitting diodes.* Apl Materials, 2019. **7**(2).
189. Zou, C., et al., *Highly stable cesium lead iodide perovskite quantum dot light-emitting diodes.* Nanotechnology, 2017. **28**(45).

190. Dai, X., et al., *Solution-processed, high-performance light-emitting diodes based on quantum dots.* Nature, 2014. **515**(7525): p. 96-99.
191. Yang, J.-N., et al., *Potassium Bromide Surface Passivation on $CsPbI_{3-x}Br_x$ Nanocrystals for Efficient and Stable Pure Red Perovskite Light-Emitting Diodes.* Journal of the American Chemical Society, 2020. **142**(6): p. 2956-2967.
192. Lu, M., et al., *Highly Flexible $CsPbI_3$ Perovskite Nanocrystal Light-Emitting Diodes.* Chemnanomat, 2019. **5**(3): p. 313-317.
193. Lifante, G., *Integrated photonics: fundamentals*. 2003: John Wiley & Sons.

# Appendices

# A.1. Integrated Optical Amplifier-Photodetector on a Wearable Nanocellulose Substrate

## A.1.1. Structural and morphological characterization

The morphology of the metal halide perovskite (MHP)films on NC substrates was analyzed by SEM using a JSM7001F (field emission scanning electron microscope).

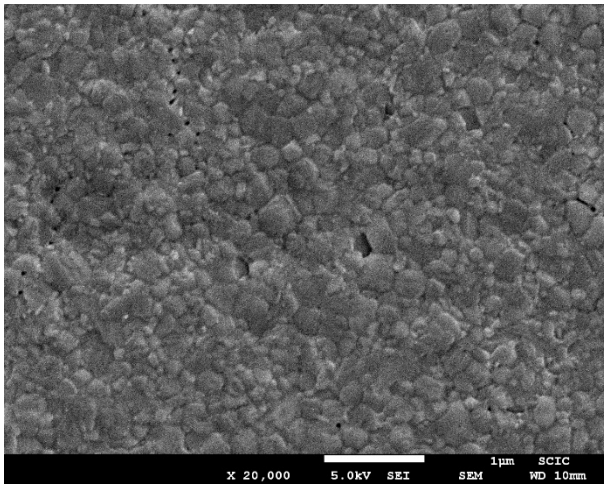


**Figure A.1.1 Top view of $MAPbI_3$ perovskite layer deposited on top of a NC substrate**

The XRD patterns of the samples were measured using an X-ray diffractometer (D8 Advance, Bruker-AXS) (Cu Kα, wavelength λ= 1.5406 Å).

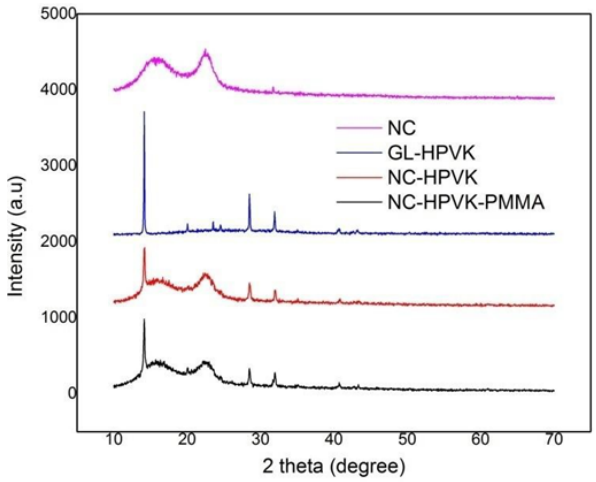


**Figure A.1.2 XRD patterns of plain NC, $MAPbI_3$ perovskite deposited on plain glass (GL), NC and NC cladded with PMMA. Peaks at 2θ = 13.9, 28.3 and 31.7 °correspond to plains (110), (220) and (310) of $MAPbI_3$, respectively. Note that any peak can be assigned to $PbI_2$.**

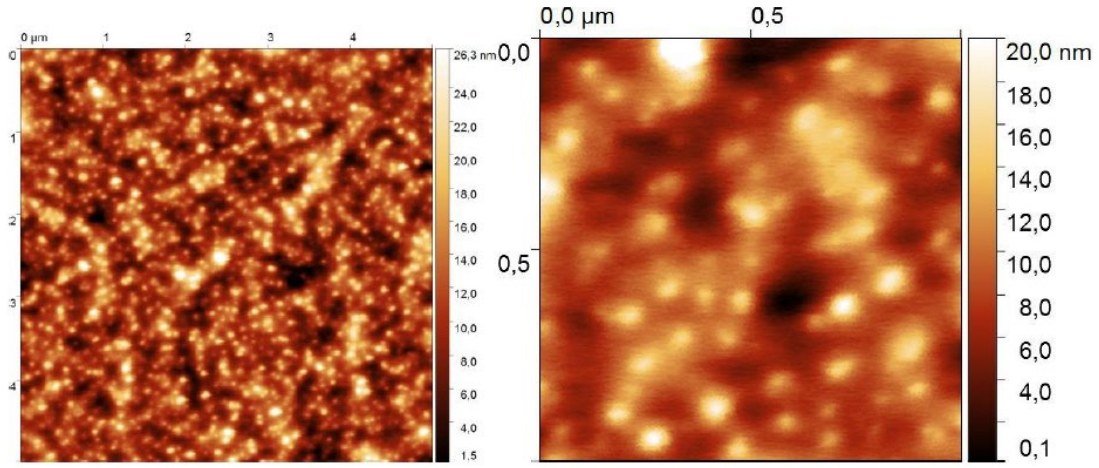


**Figure A.1.3 Atomic Force Microscopy images 5x5 (left) and 1x1 (right) µm² of a MHP film deposited on NC**

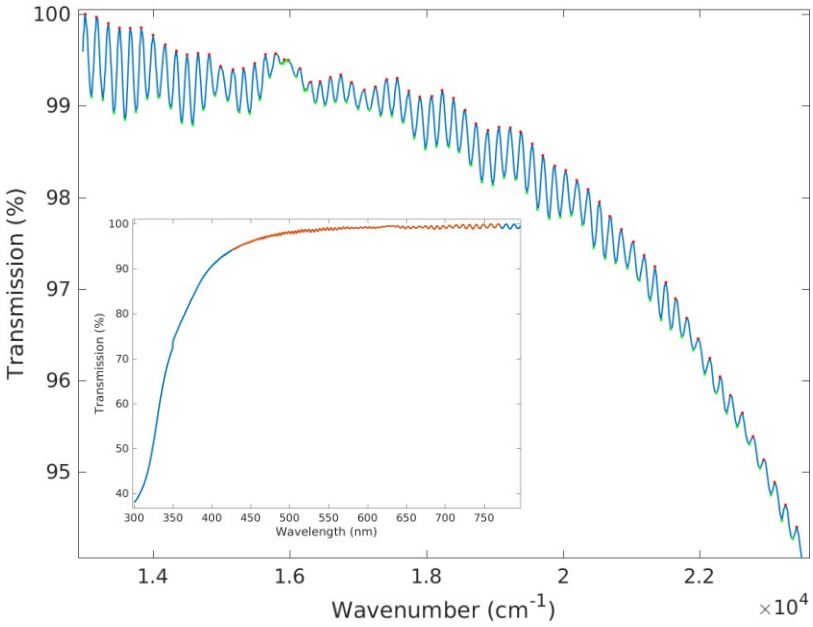


**Figure A.1.4 Interference spectrum of a NC thin film. The interference fringes have been used to characterize the film thickness. The inset corresponds to the UV-VIS transmission spectrum**

**Table A.1.1 Comparison between expected value (from previous thickness calibration) of the NC thin film and thickness calculated from interferences on three different zones of the same sample. Estimated uncertainty on the sample thickness is about 0.5 μm**

| Area | | A1 | A2 | A3 |
|---|---|---|---|---|
| $d_{expected}$ | [μm] | 20 | 20 | 20 |
| $d_{calculated}$ | [μm] | 21 | 22 | 20 |

### A.1.2. Propagating modes in PMMA/MHP layers

The refractive indices of the materials forming the waveguides (WGs) of MHP (on NC and $Si/SiO_2$) are listed in Table A.1.2. Since the refractive index of the MHP is higher than that of nanocellulose the structure conforms a planar waveguide, whose modes can be calculated with a transfer matrix algorithm.[193] Table A.1.3 presents the effective refractive indices of the modes at the pump (532 nm) and PL (780 nm) wavelengths for a waveguide composed by 350 and 850 nm thick MHP and PMMA bi-layers, respectively. Modes at 780 nm (red line in Figure 4.1.1e of the manuscript showed the fundamental mode, $TE_0$) are highly confined in the MHP semiconductor, while the pumping laser at 532 nm can propagate along the MHP ($TE_0$ and $TE_1$) or the PMMA ($TE_2$) layers forming part of the WG. However, the high absorption of the MHP at the pumping laser wavelength inhibits the propagation of the former two modes, and hence the excitation mainly travels along the $TE_2$ mode. Nevertheless, the overlap of the evanescent field of this $TE_2$ mode with the MHP film that enables its PL excitation (green line in Figure 4.1.1e).

**Table A.1.2 Refractive indices of materials**

| Material | 532nm | 780nm |
|---|---|---|
| **Air** | 1 | 1 |
| **PMMA** | 1.492 | 1.484 |
| **$CH_3NH_3PbI_3$** | 2.42-0.55i | 2.34-0.05i |
| **nanocellulose** | 1.54 | 1.54 |
| **$SiO_2$** | 1.4607 | 1.4537 |
| **Si** | 4.1353-0.0334i | 3.6944-0.0063i |

**Table A.1.3 Effective refractive indices of the WG modes**

| Mode | 532nm | 780 nm |
|---|---|---|
| **$TE_0$** | 2.34166-0.56i | 2.20274-0.05i |
| **$TE_1$** | 2.09493-0.58i | 1.7852-0.0545i |
| **$TE_2$** | 1.46501-0.0022i | - |

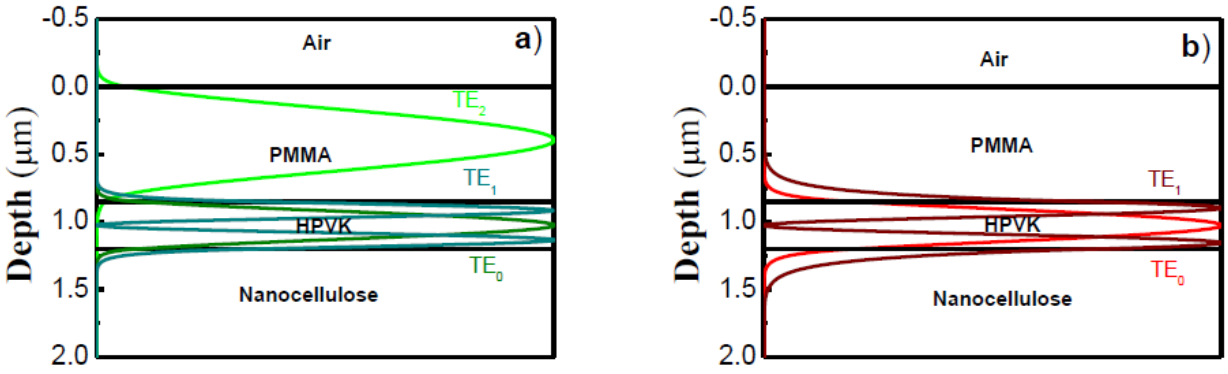


**Figure A.1.5 Power mode distribution along the different layers. a) 532 nm. b) 780 nm.**

### A.1.3. ASE measured under back-scattering geometry

The MHP films deposited on nanocellulose exhibits a stable ASE regime underback-scattering geometry using a pumping pulsed (< 1ns) laser at 100 Hz of repetition rate.

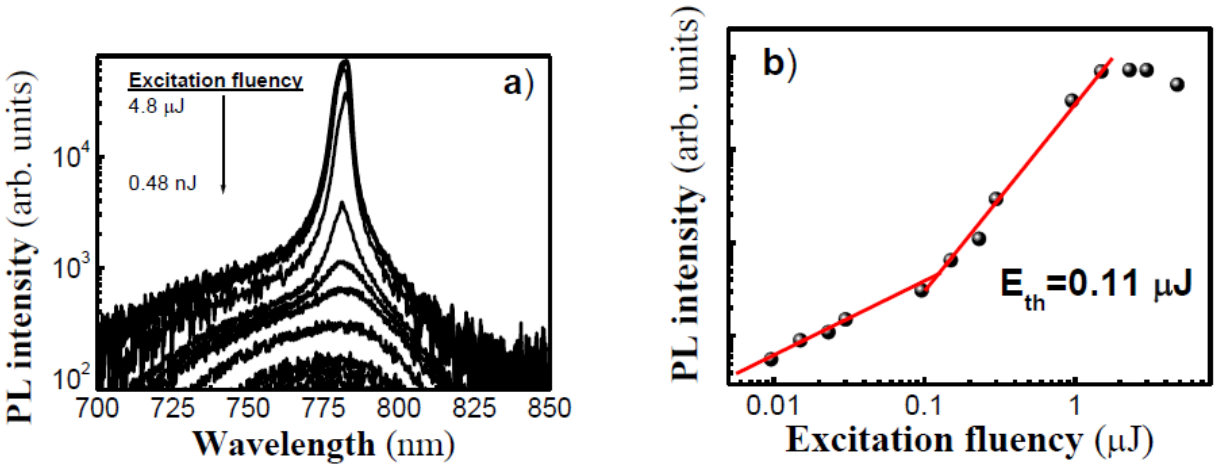


**Figure A.1.6 ASE measured in a350 nm thick CH3NH3PbI3film deposited on NC under backscattering geometry using for pumping a pulsed laser at 100 Hz of repetition rate. a) PL spectra. b) PL intensity at 780 nm as a function of the excitation fluency.**

### A.1.4. I-V characteristics under dark conditions

Figure A.1.7 shows the I-V response under dark conditions of several MHP films (350 and 500 nm thick) deposited on $Si/SiO_2$ (Figure A.1.7a) and nanocellulose (Figure A.1.7b) substrates to extract the dark current.

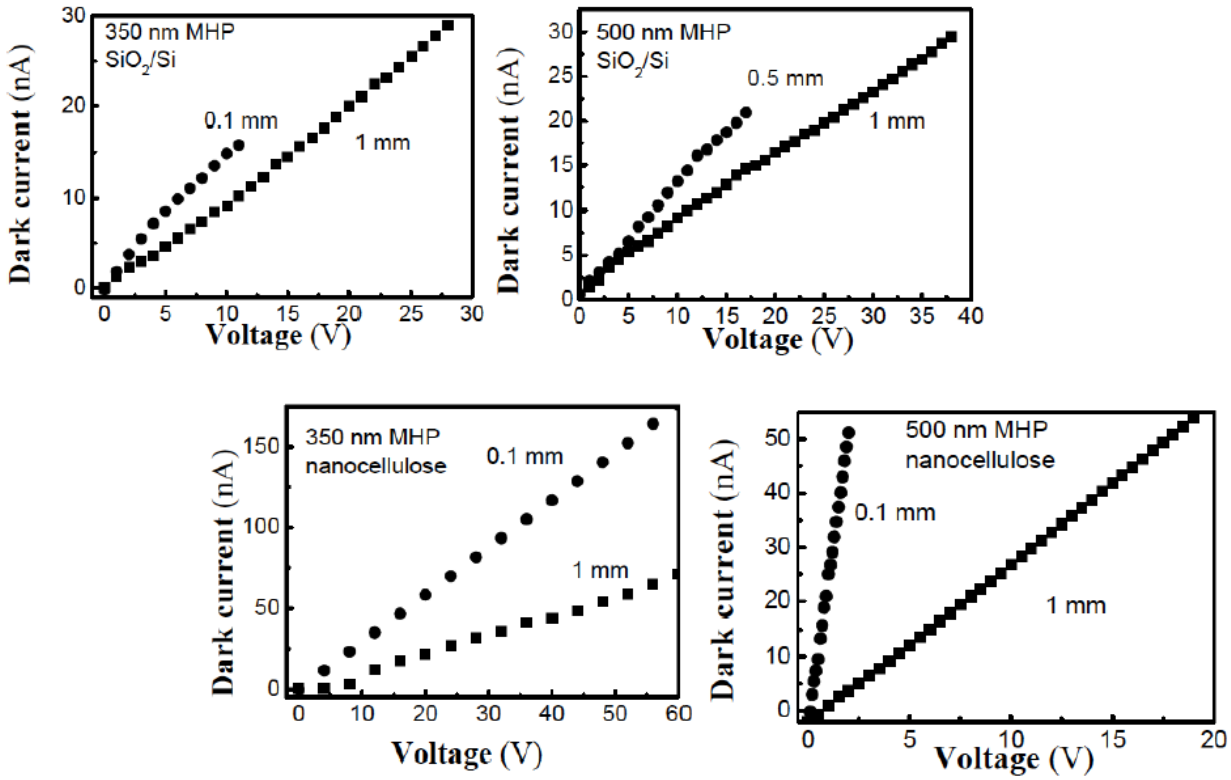


**Figure A.1.7 I-V curves under dark conditions in photoconductive devices with electrodes separated a certain distance (indicated in the figures) deposited in MHP films (350 and 500 nm thick) on a) $Si/SiO_2$and b) Nanocellulose substrates.**

### A.1.5. Photodetector frequency bandwidth and transient photocurrent

The frequency bandwidth and transient photocurrent were measured on a 350 nm thick MHP film spin-coated on a $SiO_2$/Si substrate. A similar behavior is observed in the film deposited on NC, but exhibiting smaller signal-to-noise ratio.

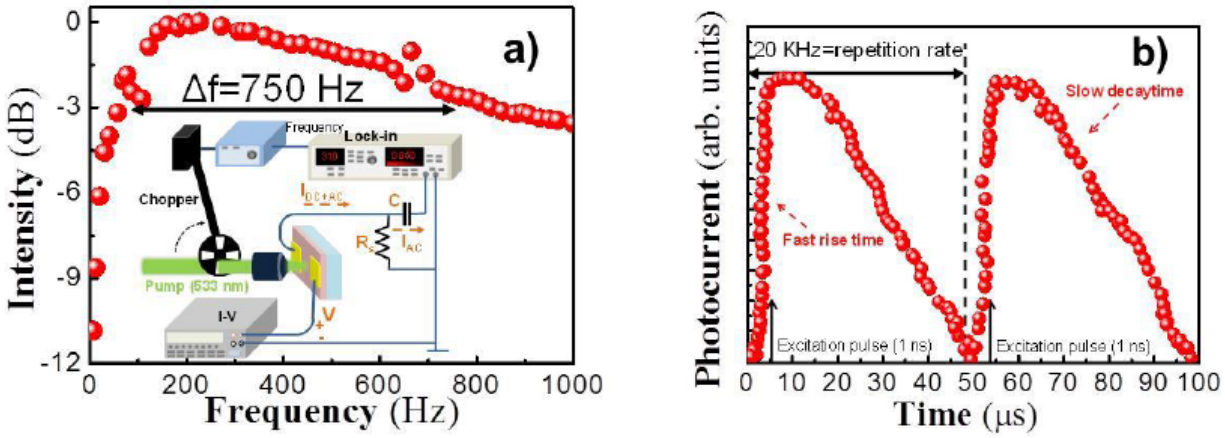


**Figure A.1.8 a) Photocurrent as a function of the chopper frequency (see the experimental set-up at the inset) under a CW excitation at 532 nm for 350 nm thick MHP layers spin-coated on a $SiO_2$/Si substrate. b) In the same sample, photocurrent transient under pulsed excitation (1 ns, 20 kHz) at 532 nm measured with a 100 MHz oscilloscope. The applied bias voltage was 10 V.**

### A.1.6. Light coupled on NC substrates

Figure A.1.9a shows the coupling of light on a PMMA/ $CH_3NH_3PbI_3$waveguided deposited on NC. Although this is a flexible substrate. it becomes possible to couple light and demonstrate amplification (see Figure A.1.9b)

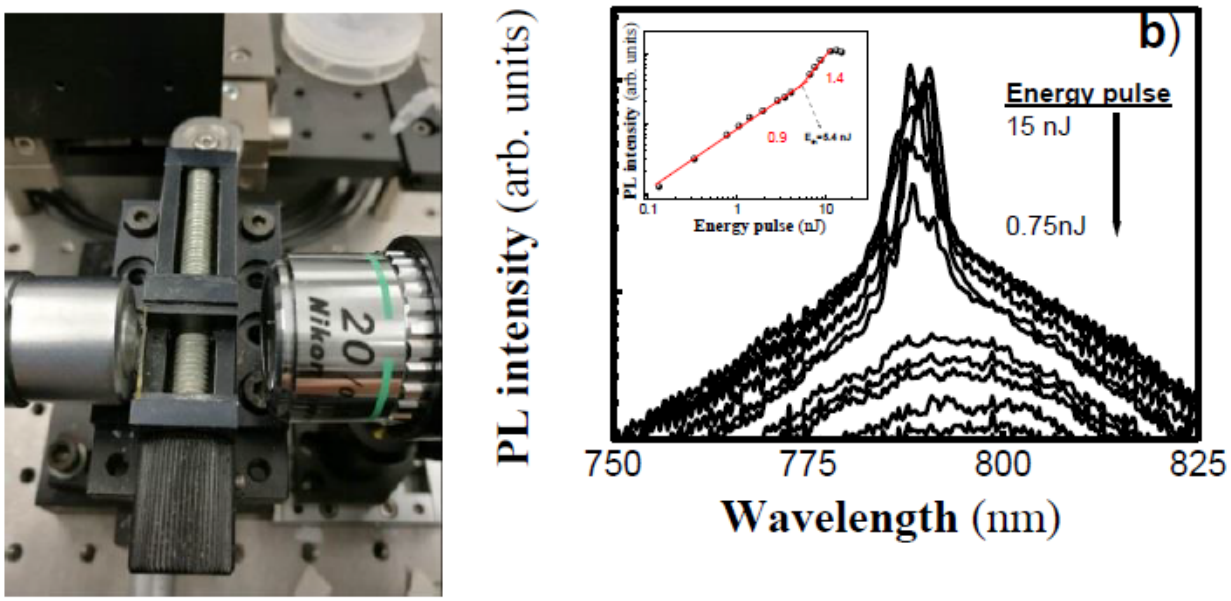


**Figure A.1.9 a) Light coupled on PMMA/$CH_3NH_3PbI_3$ waveguide deposited on NC. b) ASE measured under these conditions.**

## A.1.7. Modelling of carrier and photon generation

Under high excitation conditions, photogenerated carriers out of equilibrium, $\Delta n=\Delta p$, are much higher than the equilibrium concentration in MHP ($n_0$ or $p_0$) and are influenced by the stimulated emission. Then, the generation of carriers/photons fulfills the following set of two coupled differential equations:

$$\frac{\partial \Delta n(z)}{\partial t} = G(z) - B.\Delta n^2(z) - \sigma.(n(z) - N_0).\frac{S(z)}{h\vartheta} \quad \textbf{A.1.1}$$

$$\frac{dS(z)}{dz} = (\sigma.(n(z) - N_0) - \alpha_0).S(z) + R.\Delta n(z) \quad \textbf{A.1.2}$$

where $B$ is the radiative recombination rate, σ the gain cross section, $N_0$ the transparence carrier density[2], $S(z)$ the PL density ($I_{PL}/A$), $\alpha_0$ the intrinsic losses of the waveguide, $R$ a factor related with the generation of spontaneous emission inside the waveguide, and $G$ is related to the photogeneration of electron-hole pairs:

$$G(z) = \frac{P(z)}{A.h\vartheta}.\alpha \quad \textbf{A.1.3}$$

where $P(z)$ is the excitation peak power at position $z$ overlapping the active region, $\alpha$ the absorption coefficient at the excitation wavelength, $A$ the area of excitation and $h$ the energy of the pump photon at 532 nm. This model neglects the contribution of carrier diffusion because the length of the waveguide, 1 mm, is much longer than the diffusion length of carriers in the perovskite, 0.1 mm.[42] Here, $I_{ph}(z)$ is related to $\Delta n\, z$ by:

$$\frac{I_{ph}(z)}{A'} = e.\mu_n.\left(n_0 + \Delta n(z)\right).\frac{V}{g} \quad \textbf{A.1.4}$$

where $e$ is the electron charge, $\mu_n$ the electron mobility, $V$ the applied voltage and $g$ the gap between the electrodes; and the total photocurrent intensity measured along the whole length of the WG ($L$) will be:

$$I_{ph} = \frac{1}{L}\int_0^L I_{ph}(z)dz \quad \textbf{A.1.5}$$

This model supports our experimental results reported in Figure 4.1.3d that were fitted with equations A.1.1 and A.1.2 by using $B=2.8\cdot10^{-10} cm^{-3}/s$, $\sigma=2.7\cdot10^{-15}$ cm$^2$, $N_0=10^{18}$ cm$^{-3}$.

[2] the carrier density at which optical gain balances the material loss

### A.1.8. Waveguide PL/photocurrent spectra on $SiO_2$/Si substrates

Figure A.1.10 shows PL and photocurrent on a MHP/PMMA (350 nm/850 nm thick) waveguide fabricated on $SiO_2$/Si substrate, and characterized under similar conditions as the results shown in Figure 4.1.3d. Photocurrent was measured by applying 30 V on gold electrodes separated 0.5 mm. Again, PL collapses to a narrow peak (Figure A.1.10a) and follows a superlinear law $\boldsymbol{I_{PL} \propto I_{PUMP}^{2.8}}$ above a threshold of around 1 nJ (blue symbols in Figure A.1.10b). In these conditions, the measured photocurrent (red symbols in Figure A.1.10b) follows a square root law with the excitation fluency. The trend of both magnitudes (light emission intensity and photocurrent) was nicely fitted (blue and red continuous curves in Figure A.1.10b) using the model explained in the precedent section by using $B=1.7\cdot10^{-10} cm^3/s$, $\sigma=2.7\cdot10^{-15}$ cm$^2$, $N_0=10^{18}$ cm$^{-3}$. The lower value for $B$ needed to fit the data, as compared to that found for the device fabricated on cellulose, is again explained (see section 4.1) by the weaker influence of non-radiative channels in the MHP grown onto the$SiO_2$/Si substrate.

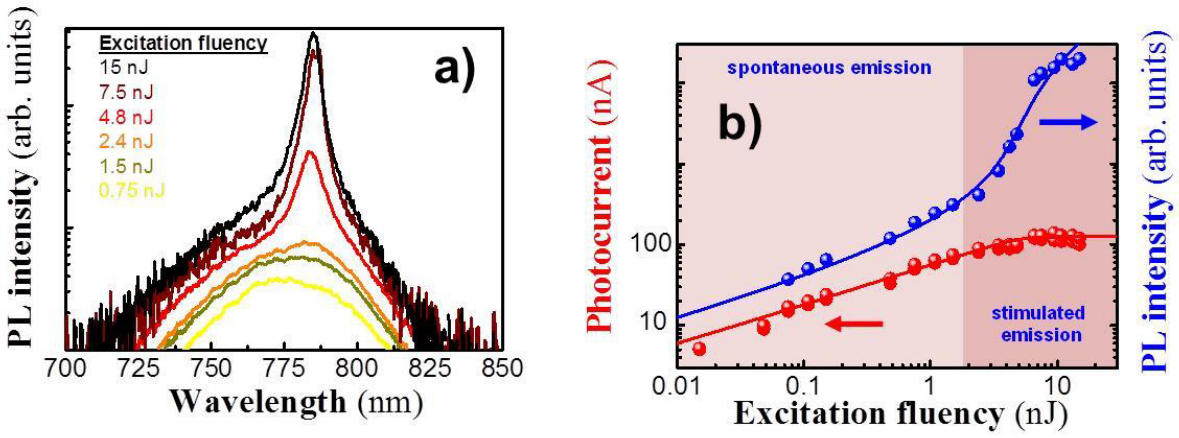


**Figure A.1.10 Photocurrent and PL intensity measured at the output edge of the MHP/PMMA waveguide fabricated on the $SiO_2$/Si substrate as a function of the excitation fluency coupled at the input edge of the WG: a) Waveguided PL spectra at measured for different pumping energies of the 532 nm pulsed laser (20KHz, 1 ns)b) Pulsed excitation demonstrates stimulated emission in the PL and a root-square dependence in the photocurrent below threshold and saturation above it. Symbols correspond to experimental data and solid lines to the best fit using the model presented in A.1.6.**

# A.2. Operation Mechanism of Perovskite Quantum Dot Solar Cells Probed by Impedance Spectroscopy

## A.2.1. TEM image of $CsPbI_3$ QDs and their diameter distributions

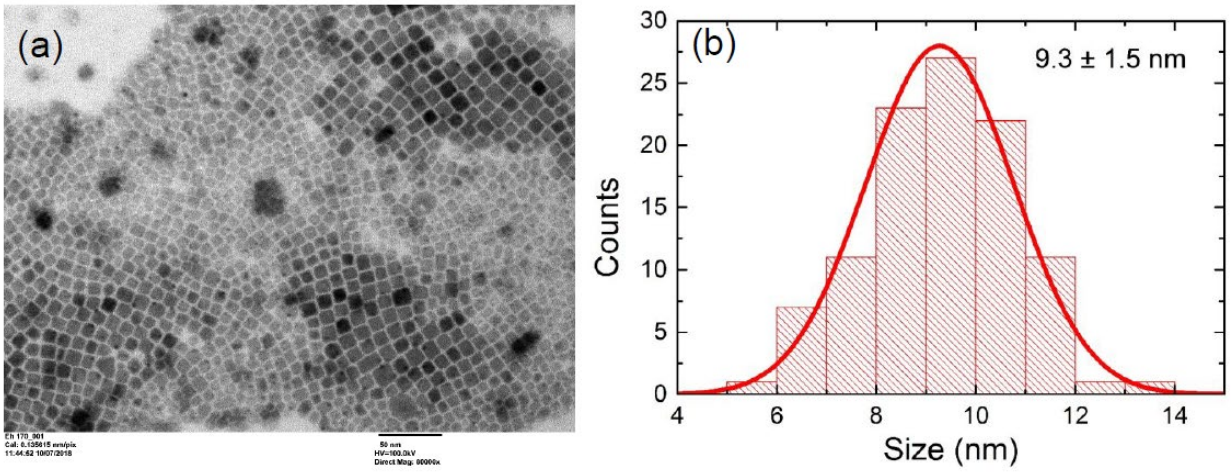


**Figure A.2.1 .(a) TEM image of $CsPbI_3$ QDs and (b) their diameter distributions (9.3 ± 1.5 nm).**

## A.2.2. XRD pattern of $CsPbI_3$ QDs

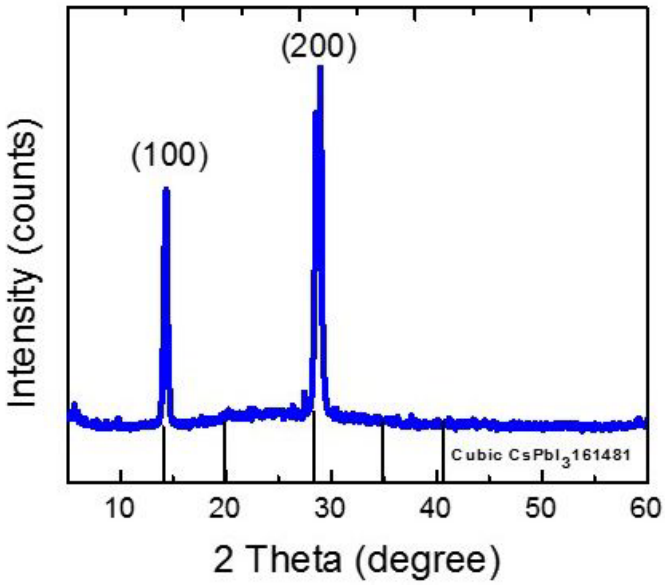


**Figure A.2.2 XRD pattern of $CsPbI_3$ QDs (blue solid line). For comparison diffractions from cubic $CsPbI_3$, crystallographic data ICSD-161481, are also included (black solid lines).**

## A.2.3. J-V curves measured under forward and reverse scans

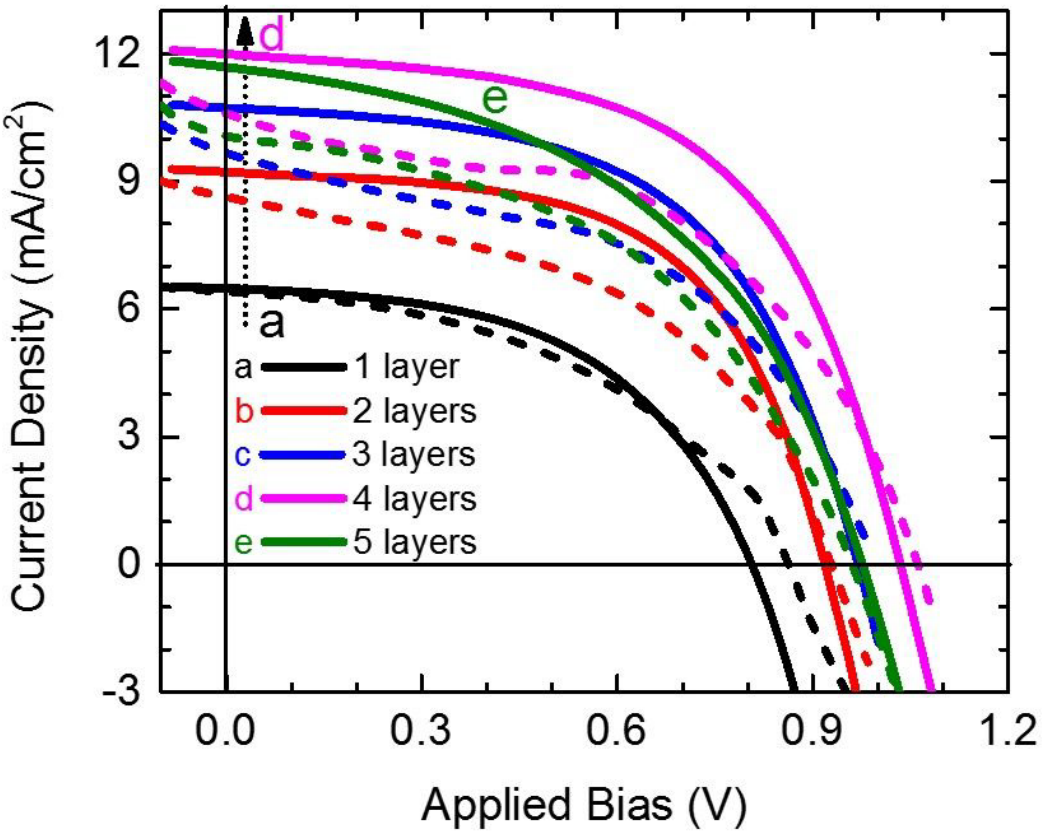


**Figure A.2.3 J-V curves measured under forward (dashed line) and reverse scans (straight line) of PQDSCs prepared from a QD solution of 50 mg/ml as function of the number of deposited layers.**

## A.2.4. J-V curve measured under forward and reverse scans of the champion cell

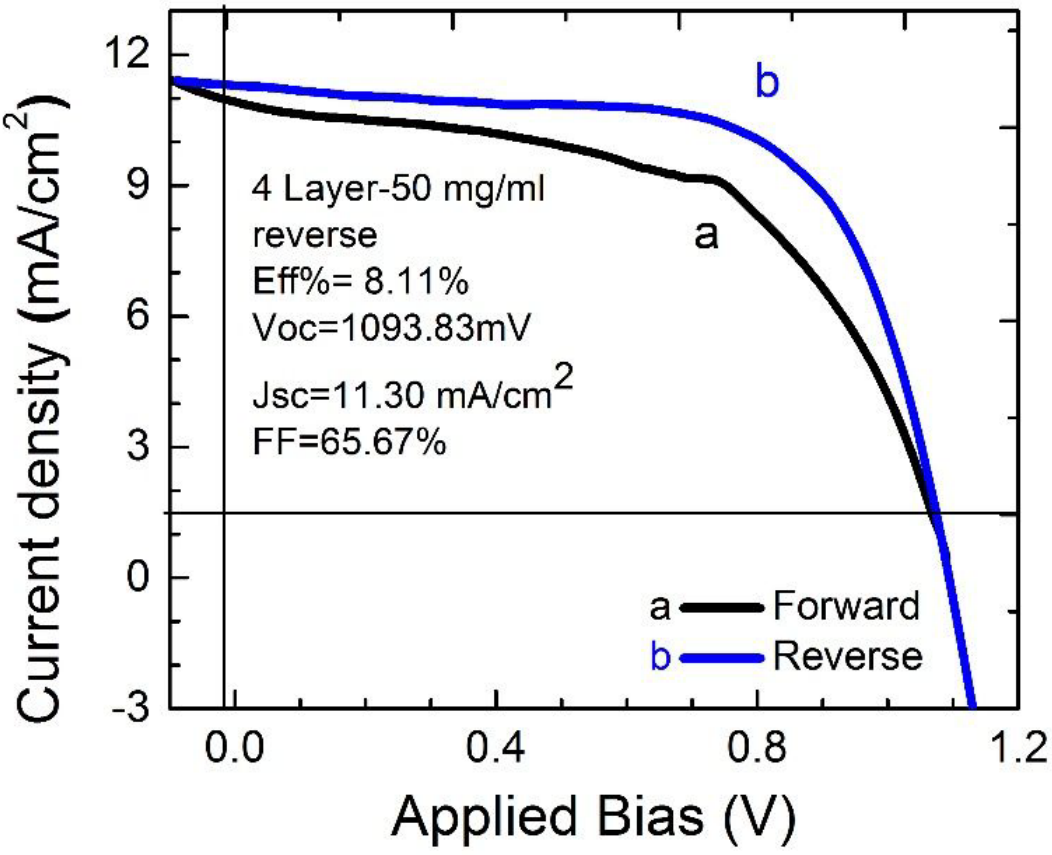


**Figure A.2.4 J-V curve measured under forward and reverse scans, of the champion cell fabricated in this study.**

## A.2.5. Example of the IPCE measured for the fabricated PQDSCs

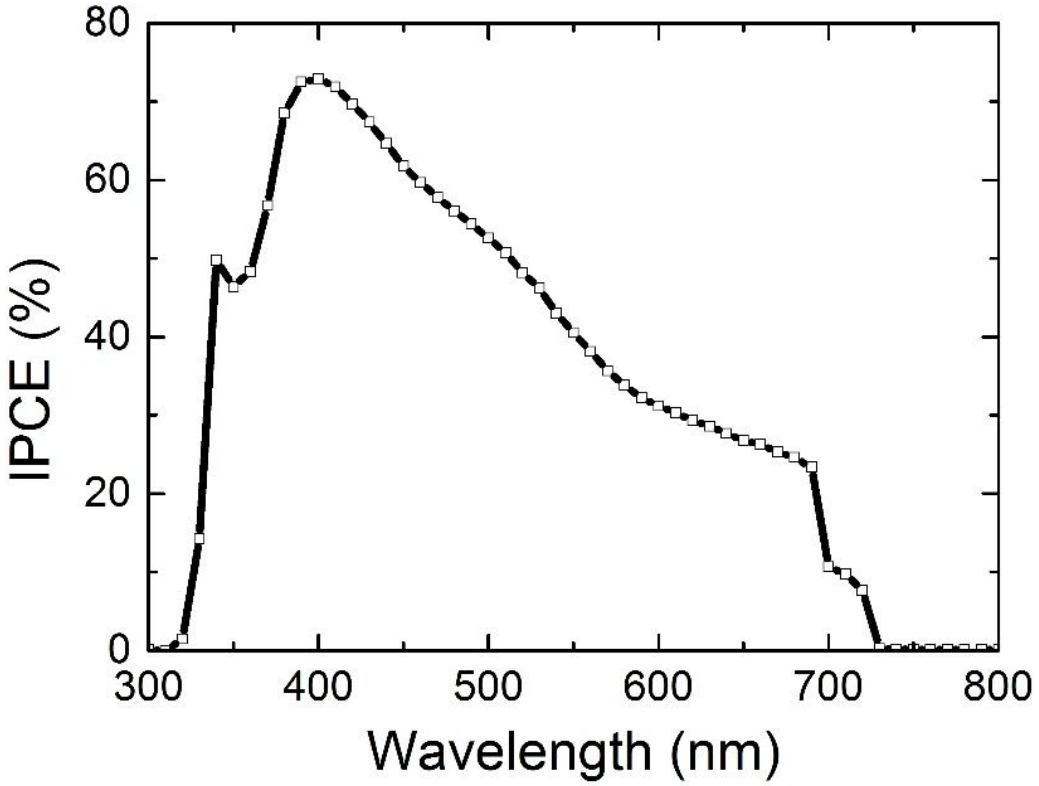


**Figure A.2.5 Example of the IPCE measured for the fabricated PQDSCs, from same champion cell fabricated in this study.**

## A.2.6. Equivalent circuit used for fitting the IS experimental data

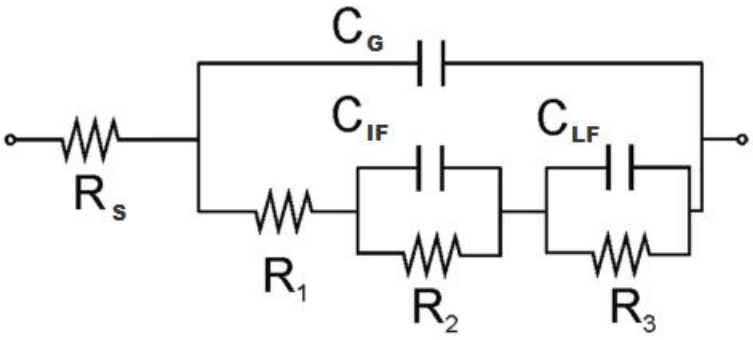


**Figure A.2.6 Equivalent circuit used for fitting the IS experimental data.[29]**

$R_s$ is the series resistance originated by wires, connections and FTO sheet. $C_G$ is the geometric capacitance of the device at high frequency. $C_{IF}$ is the intermediate frequency capacitance. $C_{LF}$ is the low frequency capacitance, associated with an accumulation capacitance of majority carries mediated by the presence on mobile ions.[28, 156] Interpretation of the physical meaning of $R_1$, $R_2$ and $R_3$ is not straight forward. The sum of all resistances provides the DC resistance:

$$R_{DC} = R_1 + R_2 + R_3 + R_S$$

where $R_{DC}$ is the inverse of the slope of the current-voltage, J-V, curve. $R_1$ and $R_2$ are the responsible of the high frequency feature observed in Figure 4.2.3b, that contains information about transport resistance in the selective contacts.[29, 147] J-V curve reconstruction from impedance measurements suggest that recombination resistance, $R_{rec}$ , cannot be directly related with low frequency resistance, $R_3$, but with the sum of high and low frequency resistances,[28, 153] analogously we have considered recombination resistance as:

$$R_{rec} = R_{DC} - R_S$$

Note that this expression overestimates $R_{rec}$ as it includes a contribution from transport resistance at the selective contacts but still a valid approach for a qualitative comparison as selective contacts used in all the analyzed samples are the same.

## A.2.7. High frequency resistance and Low frequency resistance

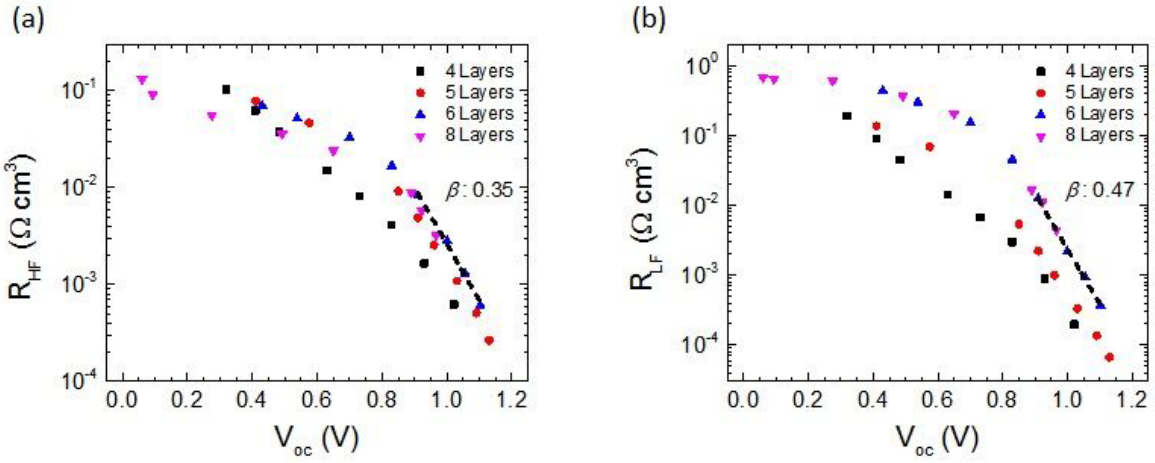


**Figure A.2.7 (a) High frequency resistance, $R_{HF} = R_1+R_2$ and (b) Low frequency resistance, $R_{LF} = R_3$ used in the determination of recombination resistance, $R_{rec} = R_1+R_2+R_3$ in Figure 4.2.3c. The β value obtained for thicker samples at high voltage is indicated. $R_H$, $R_{LF}$ and $R_{rec}$ present relatively similar β values in good agreement with the β =1/m=0.42 value obtained from the dependence of the voltage with the light intensity, Figure 4.2.3a.**

## A.2.8. Characteristic time obtained as $\tau = C_{LF} \cdot R_{rec}$

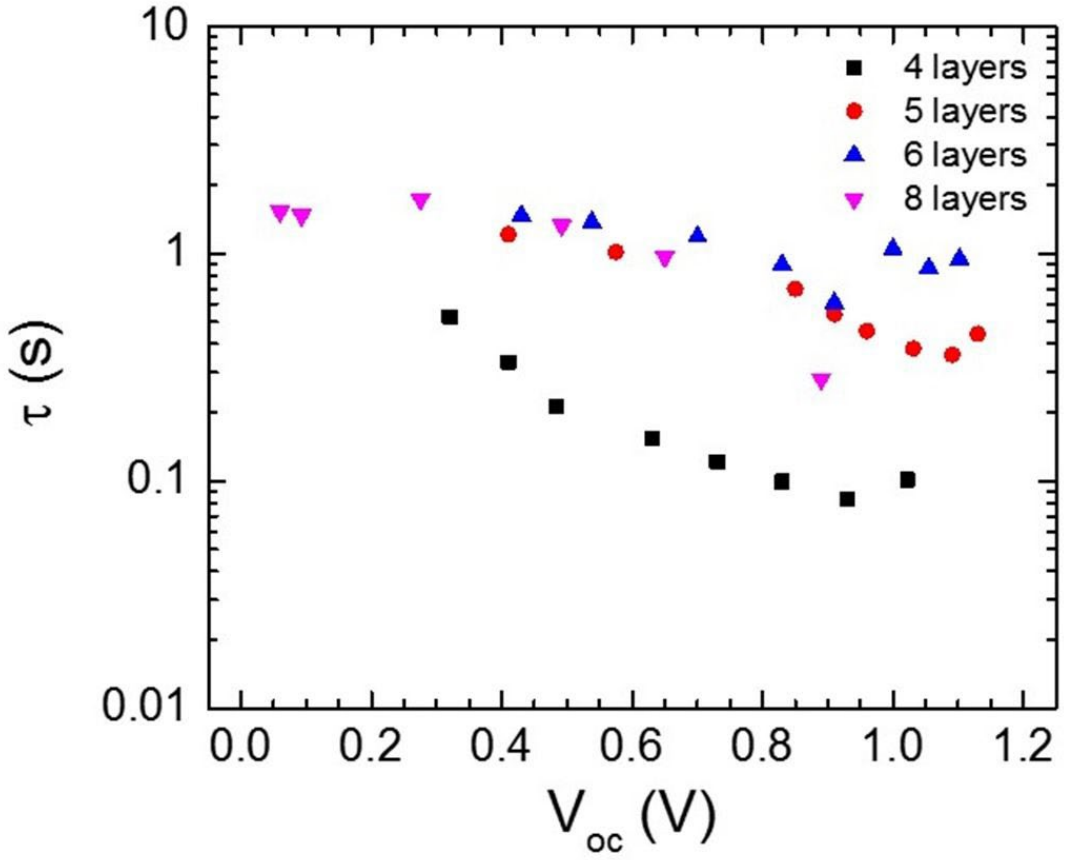


**Figure A.2.8 Characteristic time obtained as $\tau = C_{LF} \cdot R_{rec}$ from the data in Figure 4.2.3.**

In a good solar cell high $R_{rec}$ are observed, consequently $\tau$ mainly depends on $C_{LF}$. $C_{LF}$ has been related with the device hysteresis decreasing when hysteresis decrease,[160] as in inverted solar cells. In this context $\tau$ could be a good parameter to describe a perovskite solar cells as it is practically independent of the applied voltage and on the illumination.[28] However, a clear determination of the physical meaning of $C_{LF}$ is needed in order to provide $\tau$ with a physical insight beyond a mere phenomenological parameter.

# A.3. Ligand & Band Gap Engineering: Tailoring the Protocol Synthesis for Achieving High-Quality $CsPbI_3$ Quantum Dots

## A.3.1. $^{13}$C-NMR of OA/OLA samples

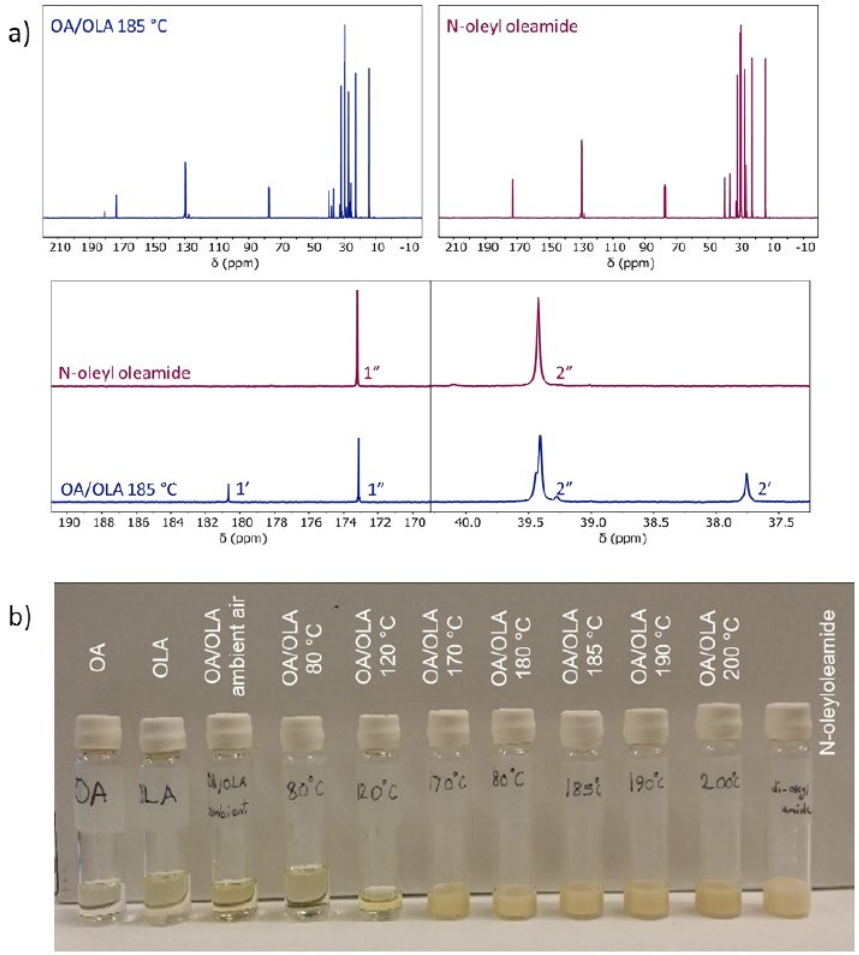


**Figure A.3.1 (a) $^{13}$C-NMR of OA/OLA samples at 185 °C and pure N-oleyl-oleamide (NOA). In sample of OA/OLA at 185 °C, two signals corresponding to the carbonyl carbon atoms (1' and 1") are visible and also two signals of the carbon atoms next to carbonyl (2', 2"). On the other hand, in the sample of pure N- oleyl-oleamide, only one signal of carbonyl group appeared. Besides $^{1}$H-NMR of the samples, this is another proof that ammonium oleate salt is fully converted to carboxylic amide. (b) Image of OA/OLA mixtures (1:1 molar ratio) heated at diverse synthesis temperatures to carry out the formation of OLM and N-oleyl-oleamide compounds.**

## A.3.2. $^{1}$H -NMR spectra of OA/OLA mixtures

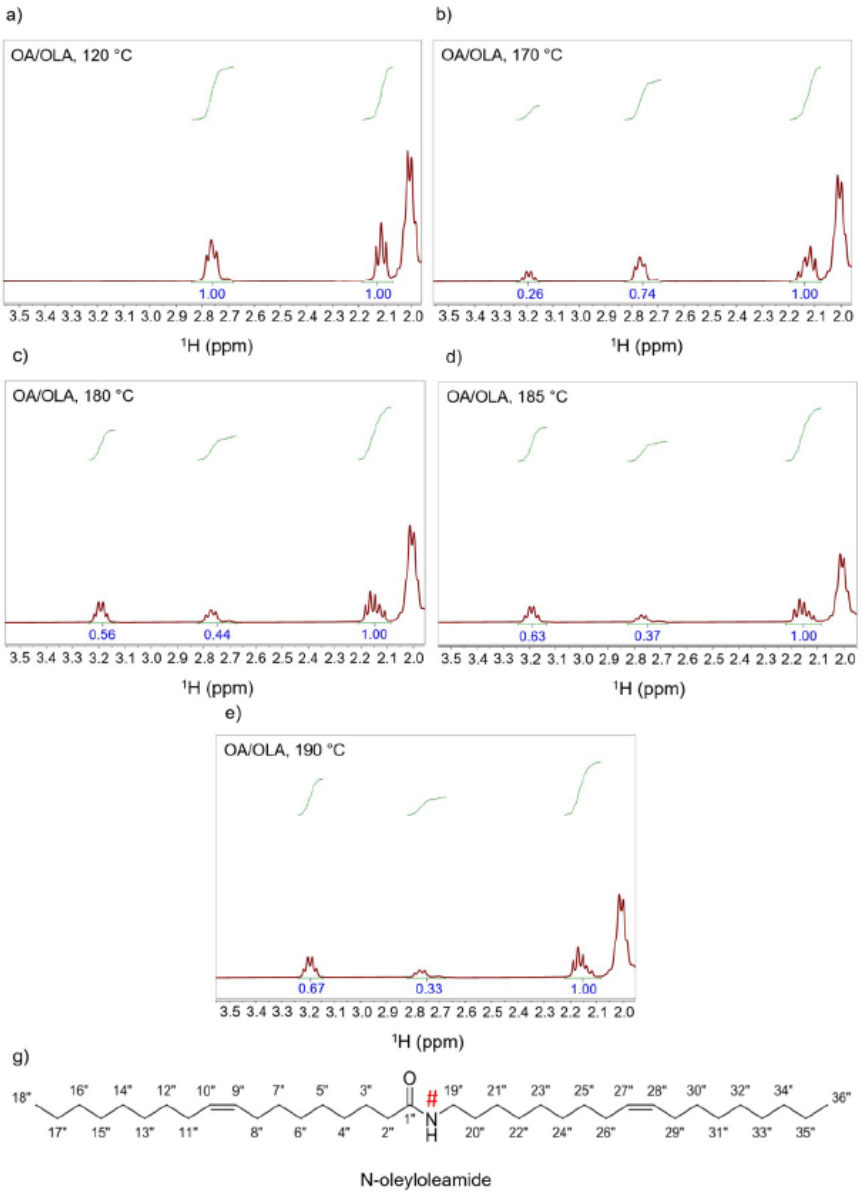


**Figure A.3.2 (a-f) $^{1}$H -NMR spectra of OA/OLA mixtures (1:1 molar ratio) heated at different synthesis temperatures. (g) Structure of the oleyl-oleamide obtained from NMR measurements.**

### A.3.3. $CsPbI_3$ QDs solutions prepared at different synthesis temperature under visible and UV light

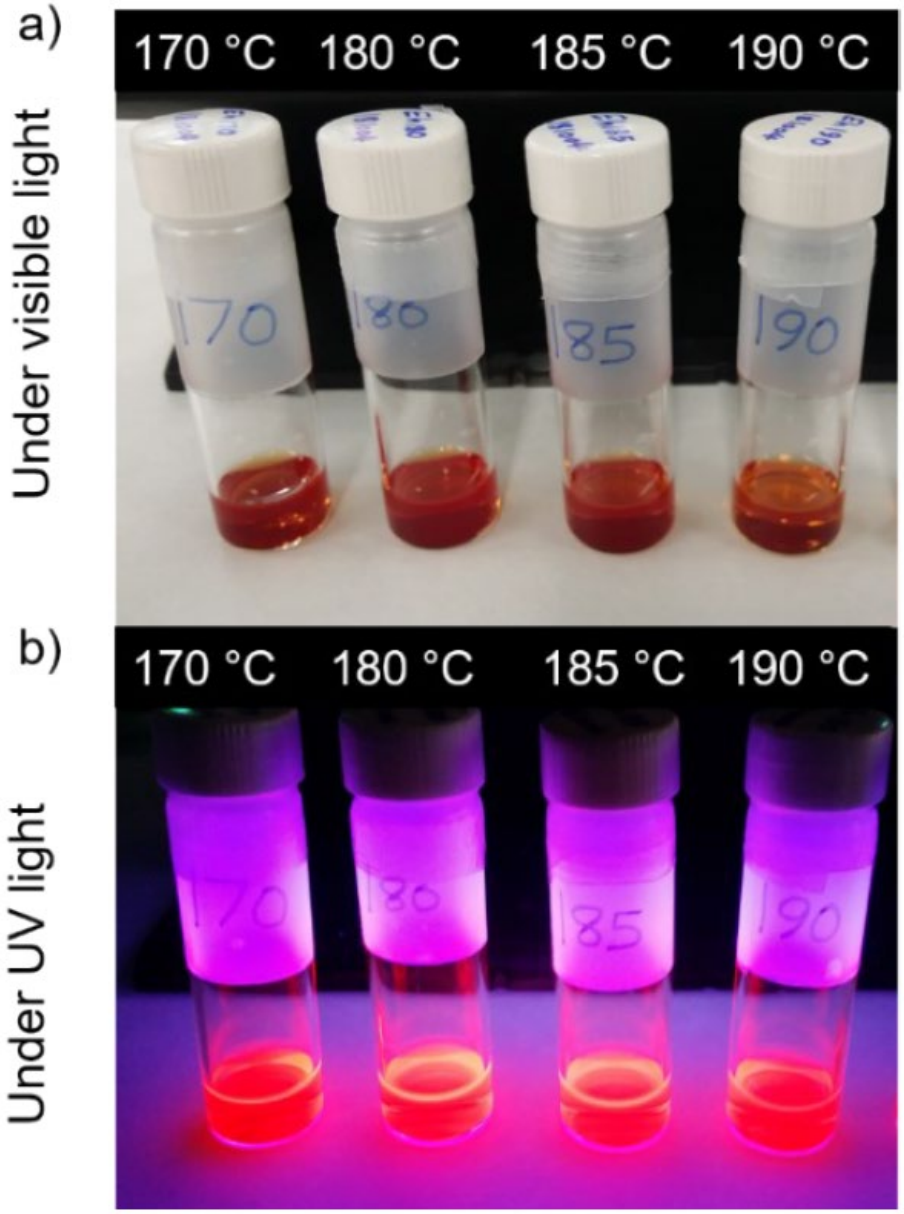


**Figure A.3.3 Pictures of the $CsPbI_3$ QDs solutions prepared at different synthesis temperature under (a) visible and (b) UV light.**

## A.3.4. Histograms of the particle size distribution obtained from TEM images for the $CsPbI_3$ QDs synthesized at different temperatures

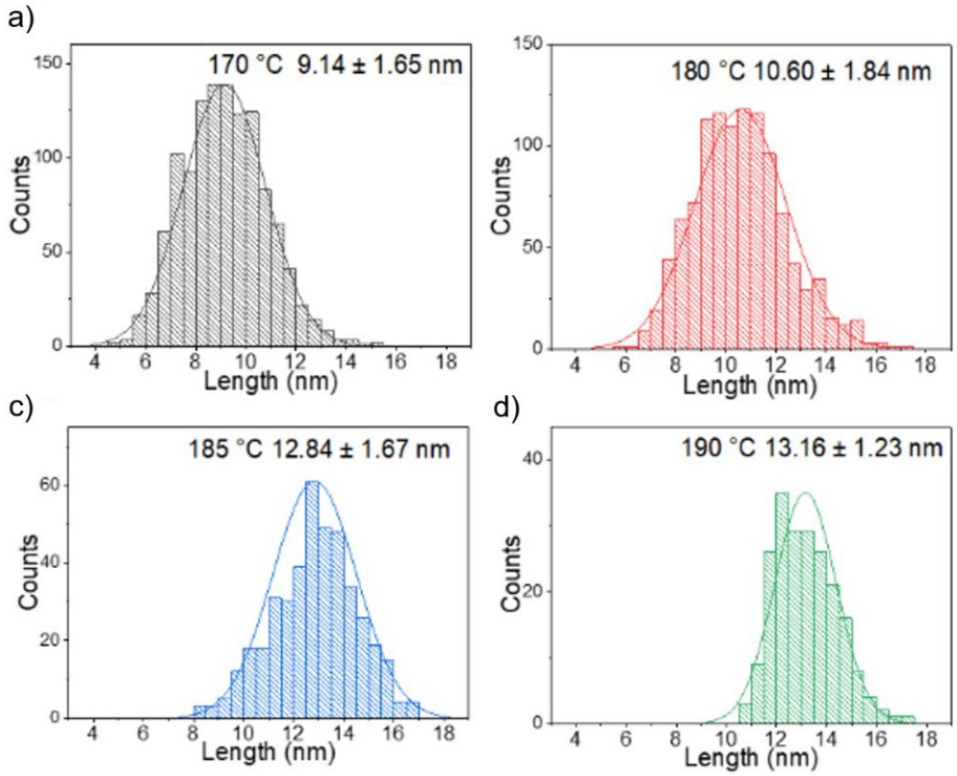


**Figure A.3.4 Histograms of the particle size distribution obtained from TEM images for the $CsPbI_3$ QDs synthesized at (a) 170 °C, (b) 180 °C, (c) 185 °C and (d) 190 °C. In order to avoid the selectivity in the QDs size during the measurements, all the QDs available in TEM images were measured for each sample.**

## A.3.5. Summary of the calculation of surface/volume and OLM/surface ratios

**Table A.3.1 Summary of the calculation of surface/volume and OLM/surface ratios.**

| Temperature (° C) | Volume of OA \| OLA (mL) | Number of moles of OLM after transformation (mmol) | Surface/ volume ratio ($10^6 \cdot cm^{-1}$) | Total volume ($cm^3$) | Total surface ($10^5 \cdot cm^2$) | OLM/Surface ratio ($10^{-5} \cdot mmol \cdot cm^{-2}$) |
|---|---|---|---|---|---|---|
| 170 | 1.5 \| 1.5 | 3.4 | 6.57 | 0.0397 | 2.60 | 1.30 |
| 180 | 2.9 \| 3.0 | 4.0 | 5.66 | 0.0397 | 2.24 | 1.79 |
| 185 | 3.9 \| 4.0 | 4.5 | 4.67 | 0.0397 | 1.85 | 2.43 |
| 190 | 3.9 \| 4.0 | 4.0 | 4.56 | 0.0397 | 1.81 | 2.21 |

Taking into account the size of the QDs grown, S, reported in Table 4.3.2 and Figure A.3.4, and the cubic shape, see Figure 4.3.3, the surface volume ratio is calculated as:

$$\frac{6S^2}{S^3} = \frac{6}{S}$$

The total mass of QDs obtained after the synthesis is same independently of the T, and we consider it is limited by the amount of Cs-Oleate 0.25 mmol. Consequently, 0.25 mmols of $CsPbI_3$ are produced after the synthesis. Taking into account the Molecular Weight (MW)=720.82 gr/mol of $CsPbI_3$ and the density of the cubic phase, 4.54 $gr/cm^{-3}$, the total volume is obtained. Considering, the surface/volume ratio the total surface that has to be passivated is calculated. Finally, considering the number of final OLM moles calculated from NMR experiments and the total surface, we obtain the ratio of both magnitudes.

A.3.6. PL decay of $CsPbI_3$ QDs synthesized at different temperatures

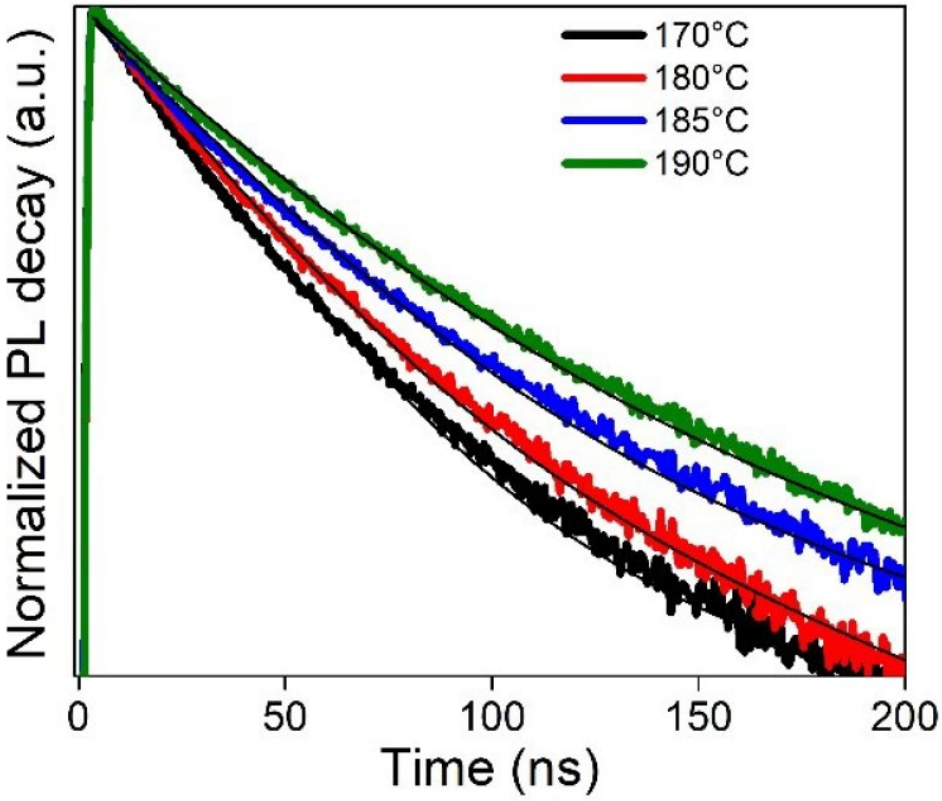


**Figure A.3.5 PL decay of $CsPbI_3$ QDs synthesized at different synthesis temperatures.**

## A.3.7. Parameters extracted from the fitting to a double exponential of the of the PL decay data

**Table A.3.2 Parameters extracted from the fitting to a double exponential of the of the PL decay data**

| Temperature (°C) | $A_1$ (%) | $\tau_1$ (ns) | $A_2$ (%) | $\tau_2$ (ns) | $\tau_{avg}$ (ns) | Absolute PLQY | $K_r$ ($10^7$ $s^{-1}$) | $K_{nr}$ ($10^7$ $s^{-1}$) | $K_{nr}/K_r$ |
|---|---|---|---|---|---|---|---|---|---|
| 170 | 80.8 | 25.3 | 19.2 | 123.4 | 77.9 | 0.82 | 1.05 | 0.23 | 0.220 |
| 180 | 72.8 | 26.6 | 27.2 | 88.7 | 61.0 | 0.88 | 1.44 | 0.20 | 0.138 |
| **185** | **72.5** | **32.7** | **27.4** | **128.9** | **90.3** | **0.92** | **1.02** | **0.08** | **0.078** |
| 190 | 64.6 | 35.7 | 35.4 | 114.4 | 85.8 | 0.90 | 1.06 | 0.10 | 0.094 |

Parameters extracted from the fitting to a double exponential of the of the PL decay data, plotted in Figure A.3.5, and radiative and non-radiative recombination decay rate constants, $K_r$ and $K_{nr}$, respectively. Expressions used in the calculations:

$$\boldsymbol{\tau_{avg}} = \frac{\sum \boldsymbol{A_i \tau_i^2}}{\sum \boldsymbol{A_i \tau_i}}$$

$$\boldsymbol{\tau_{avg}} = \frac{\mathbf{1}}{\boldsymbol{K_r + K_{nr}}}$$

$$\boldsymbol{K_r} = \frac{\boldsymbol{PLQY}}{\boldsymbol{\tau_{avg}}}$$

where absolute PLQY are used. Note that, calculation of $K_r$ and $K_{nr}$ were estimated according to PLQY range (0.82-0.92) and $\tau_{avg}$ extracted from PL decays obtained for QDs samples after 6 months of storage under air conditions.

### A.3.8. PLQY % (stability %) of QDs synthesized at different temperatures respect to initial values

**Table A.3.3 PLQY % (stability %) of QDs synthesized at different temperatures respect to initial values.**

| Temperature (°C) | **170** | **180** | **185** | **190** |
|---|---|---|---|---|
| PLQY% initial (stability %) | 87 (100) | 91 (100) | **93 (100)** | 92 (100) |
| PLQY% after 6 months (stability %) | 82 (95) | 88 (97) | **92 (99)** | 90 (98) |
| PLQY % After 15 months (stability %) | 66 (76) | 75 (82) | **86 (92)** | 84 (91) |

### A.3.9. Chromaticity coordinates of synthesized QDs at different temperatures and red color in Rec. 2020 standard

**Table A.3.4 Chromaticity coordinates of synthesized QDs at different temperatures and red color in Rec. 2020 standard**

| Temperature (°C) | X | Y |
|---|---|---|
| 170 | 0.7239 | 0.2761 |
| 180 | 0.7258 | 0.2742 |
| 185 | 0.7264 | 0.2736 |
| 190 | 0.7272 | 0.2728 |
| Rec. 2020 standard for red color | 0.708 | 0.292 |